Imaging the Shapes and Dynamics of Superfluid Helium Nanodroplets

vorgelegt von
M. Sc.
Bruno Langbehn
ORCID: 0000-0002-3245-8169

an der Fakultät II – Mathematik und Naturwissenschaften
der Technischen Universität Berlin
zur Erlangung des akademischen Grades

Doktor der Naturwissenschaften
Dr.rer.nat.

genehmigte Dissertation

Promotionsausschuss:

Vorsitzende: Prof. Dr. Kathy Lüdge
Gutachter: Prof. Dr. Thomas Möller
Gutachterin: Prof. Dr. Daniela Rupp
Gutachter: Prof. Dr. Karl-Heinz Meiwes-Broer

Tag der wissenschaftlichen Aussprache: 23. März 2021

Berlin 2021

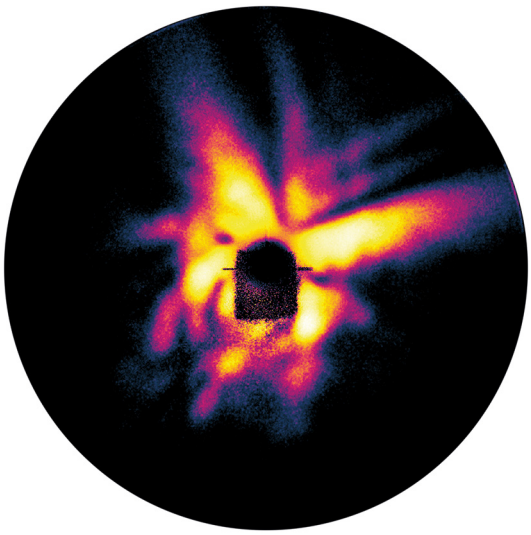

No chaos damn it.
– Jackson Pollock (1950)

Acknowledgments

I would like to thank the many people that contributed to this work – I would not have been able to complete it without your support. Looking back, I am deeply grateful for experiencing a vibrant scientific community based on teamwork and collaboration at beam times, conferences, and in academia.
It was Thomas Möller enabling me to have that experience. I want to thank him for giving me the opportunity to work in his group, for his reassuring advice, and for his guidance throughout all stages of this endeavor. I learned so much from him in so many different ways.
I am equally grateful to Daniela Rupp, who always helped me finding my way with her ability to motivate and inspire people while creating confidence by seemingly knowing what steps to be taken next. She, too, has truly become a role model for me.
Further, I want to thank Yevheniy Ovcharenko who played a key role in the experiment at FERMI and thereby organized one of the smoothest beam times I have ever participated in. Of course, this would not have been possible without the wonderful group of people working at the experiment, the FERMI staff, and the team of the Low Density Matter beamline. Therefore, I would like to especially thank Carlo Callegari, Oksana Plekan, Michele DiFraia, Kevin C. Prince, Riccardo Cucini, Paola Finetti, Alexander Demidovich, and Luca Giannessi. In addition, I want to thank Aaron C. LaForge and Paolo Piseri for the always joyful time spent at the beamline – and at "Al Tiglio".
I would like to thank Thomas Fennel and his group, especially Christian Peltz and Katharina Sander, who contributed a lot to advance the analysis and the interpretation of the data with their simulation and fitting routines.
For stimulating discussions on helium nanodroplets I would like to thank Andrey Vilesov, Manuel Barranco, Francesco Ancilotto, Marius Lewerenz, and Frank Stienkemeier.
Finally, I would like to express my gratitude to the people in the group of Thomas Möller for helping me – in one way or another – accomplish this thesis and for the congenial working environment. I want to say a special thank you to Andrea Merli who largely contributed to the enriching time I had teaching at the "Projektlabor". I want to also thank all the other group members I had the chance to work with in these past years: Mario Sauppe, Anatoli Ulmer, Julian Zimmermann, Björn Senfftleben, Rico Mayro P. Tanyag, Robert Richter, Tobias Bischoff, Andre Knecht, Maria Richter, Jan Philippe Müller, Torbjörn Rander, Linos Hecht, Andrea Heilrath, Jakob Jordan, Katharina Kolatzki, Frederic Ußling, Felix Zimmermann, Patrick Behrens, Theresa Höhne, Jonas Hügle, Morten Kallevik Straume, Leonie Werner, Alexander Nelde, Thomas Menz, Tung Cao Thanh, Pablo Nuñez von Voigt, Annabelle Spanier, Philipp Nelde, Fabian Seel, Georg Noffz, Timo Dörries, Nils Bernhardt, Jannis Zimbalski, and Niklas Schneider.

Abstract

This thesis addresses the three-dimensional (3D) structure determination of individual nanoparticles or, more precisely, helium nanodroplets, via scattering of extreme-ultraviolet light pulses. In particular, the recent development of free-electron lasers (FELs) delivering intense short-wavelength light pulses of femtosecond duration is a promising prospect for the study of unsupported particles such as proteins, nucleic acids, viruses, and also droplets on the nanometer scale. Motivated by this potential application in imaging of biomolecules, the thesis investigates superfluid helium nanodroplets in an experiment at the FERMI FEL that is focused on the interaction of intense light pulses with matter by analyzing wide-angle scattering patterns. The experiment can be divided in two parts:
In the first part, the complete 3D droplet shapes are retrieved from the diffraction patterns, enabling a comparison with theory. Despite the absence of friction in a superfluid, it is shown that the shapes of spinning superfluid helium nanodroplets resemble those of rotating normal liquid drops. Also the evolution of the droplet shapes from spherical to oblate, prolate, and even two-lobed configurations is observed.
In the second part of the experiment, scattering images of xenon doped helium nanodroplets are recorded after irradiating the droplets with intense near-infrared laser pulses to study the light induced dynamics. The diffraction patterns indicate density fluctuations in the droplets that occur as the energy of the laser pulse is deposited at the locations of the dopant atoms. The density fluctuations are further explored for two selected cases: (i) A random distribution of the fluctuations when the dopants are also randomly distributed in the droplet, and (ii) a structured distribution of the fluctuations when the dopants accumulate at specific sites, which is probably connected to the occurrence of quantized vortices in the spinning superfluid droplet.

Kurzfassung

Diese Arbeit befasst sich mit der dreidimensionalen Strukturbestimmung einzelner Nanoteilchen, genauer gesagt Helium-Nanotröpfchen, mittels Streuung extrem ultravioletter Lichtpulse. Hier bieten insbesondere die erst seit kurzem verfügbaren Freie-Elektronen-Laser (FEL), mit denen sich intensive Femtosekundenpulse im kurzwelligen Spektralbereich erzeugen lassen, einen vielversprechenden Ansatz, um einzelne Proteine, Nukleinsäuren, Viren und auch Tröpfchen auf der Nanometer-Skala zu untersuchen. Inspiriert von der Idee einzelne Biomoleküle, vor allem auch jene, die sich nicht kristallisieren lassen, direkt abzubilden, widmet sich diese Arbeit der Strukturaufklärung suprafluider Helium-Nanotröpfchen in einem Experiment am FERMI FEL. Durch die Analyse von Weitwinkel-Streubildern einzelner Tröpfchen können zudem Rückschlüsse auf die Wechselwirkung mit intensiven Lichtpulsen gezogen werden. Das Experiment lässt sich im Wesentlichen in zwei Teile gliedern:
Im ersten Teil wird aus den Streubildern die dreidimensionale Form der Tröpfchen gewonnen, was einen Vergleich mit theoretischen Gleichgewichtsformen ermöglicht. Obwohl es in einem Suprafluid keinerlei Reibung gibt, zeigt sich, dass rotierende Tröpfchen im suprafluiden und normalflüssigen Zustand sehr ähnliche Formen annehmen. Hierbei lässt sich der Übergang von sphärischen zu oblaten, prolaten und schließlich stark verformten hantelförmigen Tröpfchen beobachten.
Im zweiten Teil des Experiments werden lichtinduzierte Dynamiken in den Tröpfchen untersucht. Dazu werden die Helium-Nanotröpfchen mit Xenon dotiert und Streubilder nach Anregung der Tröpfchen mit intensiven, nah-infraroten Laserpulsen aufgenommen. Die beobachteten Streubilder weisen auf Dichtefluktuationen in den Tröpfchen hin, die dadurch entstehen, dass die Energie des Laserpulses an den Orten der Dotanden in die Tröpfchen eingebracht wird. Diese Dichtefluktuationen werden für zwei Fälle genauer untersucht: (i) Eine zufällige Verteilung der Fluktuationen, wenn die Dotanden im Tröpfchen ebenfalls zufällig verteilt sind, und (ii) eine strukturierte Verteilung der Fluktuationen, falls sich die Dotanden an bestimmten Orten sammeln, deren Position vermutlich mit dem Auftreten quantisierter Wirbel in den sich drehenden suprafluiden Tröpfchen zusammenhängt.

Contents

List of Figures

List of Tables

Chapter 1

Introduction

As we perceive the world with our eyes, all information is mediated by light that therefore plays a major role in scientific advances. At the beginning of the 17th century, the development of two optical instruments marks a milestone for insights into nature with unprecedented detail: The telescope to enlarge objects that are far away and the microscope to magnify small objects not even visible by eye. The advance into the microcosm paved the way for studying biological specimen like organic tissue, red blood cells, and bacteria, while technical improvements on the lenses enabled larger and larger magnifications, hence smaller and smaller structures could be investigated. However, as Ernst Abbe showed in the 19th century, the achievable resolution of a microscope is limited by the wavelength of the light used to illuminate the sample.

The discovery of x-rays by Röntgen in 1895 [1] opened up new possibilities to study the structure of matter: Providing sub-nanometer wavelengths, even the atomic order of crystals could be resolved [2, 3]. In the course of the 20th century, x-ray diffraction, especially x-ray crystallography, became the workhorse for structure determination of biomolecules, enabling scientists to decipher bioreactions on the molecular level [4]. Therefore, the samples need to be crystallized, which is often a challenging task when it comes to biological macromolecules such as proteins, nucleic acids, and viruses, especially when their inherent structure must not be changed during the process [5]. However, a correct identification of their natural configuration is an important prerequisite to understand their biochemical function. Hence, it would be a promising prospect to study molecules without the need of crystallization, thus enabling, e.g., tailor-made drug development or an *in situ* observation of catalytic processes. At the beginning of the 21st century, a window to observe non-crystalline macromolecules was opened by the emergence of free-electron lasers (FELs) delivering intense short-wavelength light pulses of femtosecond duration. Covering the spectral range from vacuum ultraviolet (VUV) and extreme ultraviolet (XUV) to soft and hard x-ray radiation at unprecedented power densities, these machines enabled not only to access new domains in x-ray science [6, 7] but also structure determination of nanocrystals [8] and even individual non-periodic nanoparticles such as single viruses, soot particles, metal and rare gas clusters, or helium nanodroplets [9–17].

The fundamental principle for single particle structure determination using x-ray diffraction is illustrated in Fig. 1.1. It is based on the technique of coherent diffraction imaging (CDI) applied to a single particle being imaged with a single light pulse. In Fig. 1.1 (a), the measurement process is shown. The stream of particles is intersected by

the intense x-ray beam and the scattered light is recorded with a detector. Because of the intense radiation dose, the particle will quickly disintegrate after the interaction with the light pulse. Nevertheless, when the pulse is short enough and sufficiently intense, a diffraction pattern of the still intact particle can be recorded [18]. In Fig. 1.1 (b), the structure determination process is exemplified. When the diffraction patterns are from identical particles at random orientation, patterns representing similar orientation can be grouped and averaged. From the correctly assigned orientation, the particle is then reconstructed using phase retrieval. However, despite its conceptual simplicity, there are several challenges to overcome before single particle imaging will meet the expectation of three-dimensional (3D) structure determination at atomic resolution [19]. For example, in order to perform a 3D characterization of the particle, a large number of diffraction patterns of identical particles has to be recorded. Further, the achievable resolution is ultimately limited by the ultrafast radiation damage in the particle [20].

In the context of this fast developing field, mainly driven by biomolecular applications, this thesis explores additional ways to retrieve particle shapes and trace structural changes in a scattering experiment. For the shape retrieval, a slightly different approach is chosen: It has been shown before that under certain circumstances, the 3D particle shape can be retrieved from a *single* diffraction pattern when the scattering signal is recorded up to large scattering angles [13]. In this regard, helium nanodroplets can act as an ideal model system. For many years it was believed that these droplets are spherical, but the first x-ray diffraction experiments recently performed [12] indicate that they are deformed, and it was concluded that they spin very fast. Hence, they provide a multitude of simple shapes to study.

In this early phase of determining helium nanodroplet shapes, my work for this thesis started with a scattering experiment using intense XUV light pulses from the FERMI FEL in Trieste, Italy. Motivated by previous work [12, 15, 22], this thesis seeks to expand the knowledge on the shapes of spinning helium nanodroplets by a thorough 3D shape characterization. Since the droplets are in a superfluid state where the atoms do not experience any friction, they do not rotate as a rigid body and it is therefore unclear if their equilibrium shapes differ from those of normal liquid rotating drops. However, the analysis of wide-angle scattering data of individual helium nanodroplets presented in this thesis shows that their shapes are indeed comparable to those known from theoretical models for normal liquid drops.

Furthermore, it was proposed to embed particles in a sacrificial layer of, e.g., water or helium in order to reduce radiation damage [23–25]. Since helium nanodroplets allow for easily embedding foreign species [26], they can serve as test environment to examine structural changes upon irradiation with an intense light pulse. In this context, my thesis aims at developing an understanding of the light induced dynamics in xenon doped helium nanodroplets. Therefore, the droplets are first irradiated with an infrared laser pulse before the scattering image is recorded in a so-called pump-probe setup. A huge variety of complex features is observed in the diffraction patterns which can be attributed to density fluctuations in the droplets. These are further examined for two selected types: fluctuations that are randomly distributed in the droplet and fluctuations that only occur at specific sites on the droplet surface. The occurrence of both types can be linked to the dopant atoms. While the former suggests a random distribution of the dopants, the latter indicates a possible connection to quantized vortex arrays in the superfluid droplets.

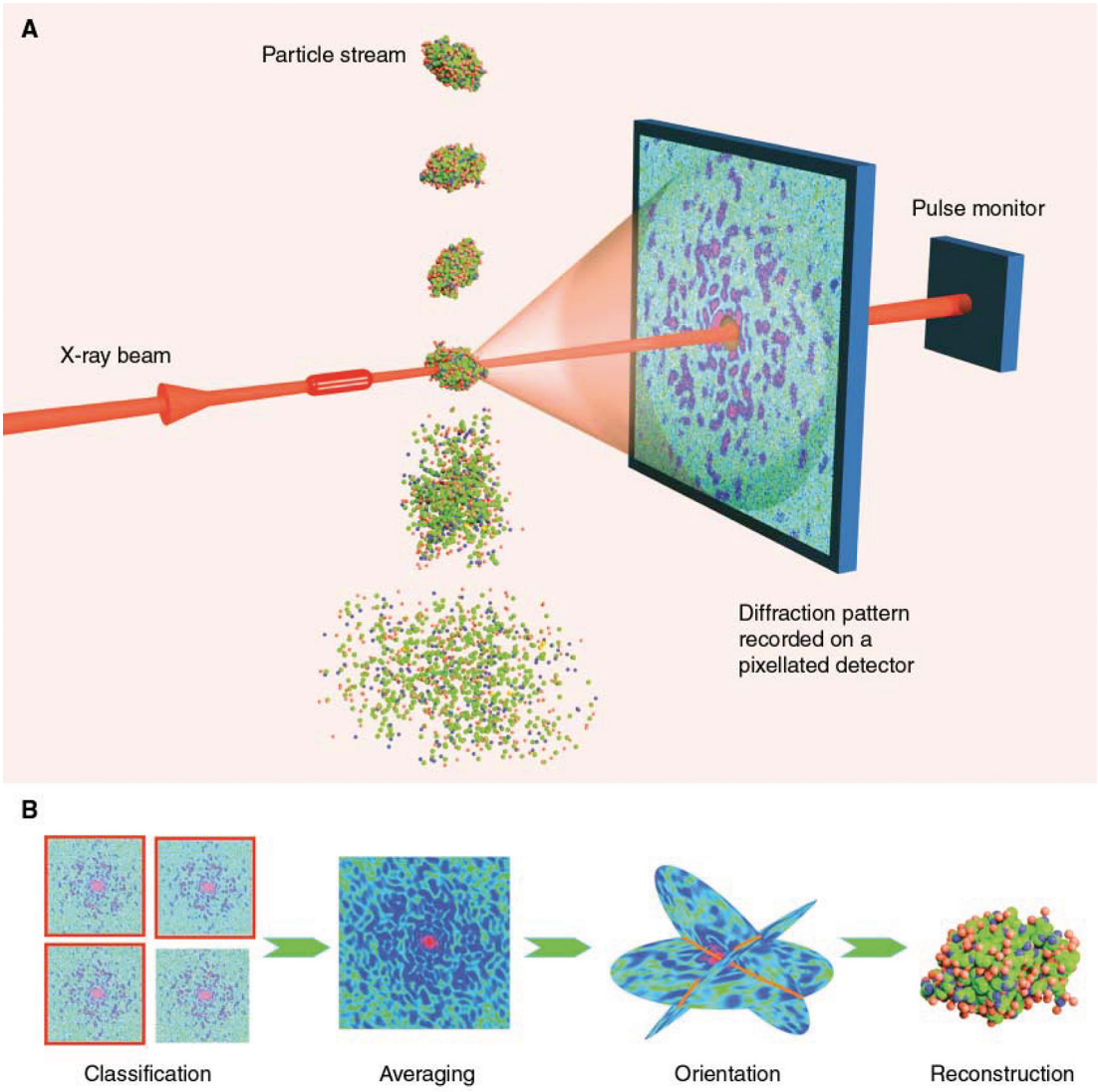

FIG. 1.1: Measurement scheme to image single particles using intense short-wavelength light pulses. (a) The particle stream is intersected by the x-ray beam and the scattered light is recorded on a detector. (b) The recorded diffraction patterns are grouped for particle orientation and, for each group, averaged. From the correctly assigned orientation, the three-dimensional particle shape can be reconstructed. Reprinted from Ref. [21].

The thesis is organized as follows: In Chapter 2, the fundamental concepts for the production and doping of helium nanodroplets, as well as important aspects of superfluidity, the shapes of rotating droplets, and the interaction of light with matter are presented. Chapter 3 gives the experimental details, i.e., the working principle and the characteristics of the FERMI FEL as well as a description of the pump-probe setup at the low density matter instrument. In Chapter 4, an overview on the recorded data is given before the results for the shape determination and the light induced dynamics are discussed. Finally, Chapter 5 summarizes the present experiment and gives an outlook on pathways to future work.

Chapter 2

Theoretical Concepts

The investigation of nanometer-sized particles by scattering of intense, short-wavelength light pulses is a promising approach for the ultimate goal of structure determination of single particles at atomic resolution. However, the interaction of intense radiation with a particle will influence the scattering process and the sample will likely be damaged, even on a very short timescale. Hence, the interpretation of the observations is a complicated task that can only be mastered by a combined effort of experiment and theory. In this context, *clusters*, i.e., self-bound ensembles of particles such as atoms or molecules, can serve as model systems to develop a fundamental understanding of the processes relevant to light-matter interaction because of their simple structure and as a link between atomic and solid state physics [27]. In my thesis, clusters of helium atoms are investigated that are synonymously referred to as *helium nanodroplets* since they remain fluid down to absolute zero. Therefore, the droplets might undergo deformations, e.g., because of rotation, and exhibit a multitude of different shapes. This makes them an ideal system to develop methods for shape retrieval via light scattering. There are two naturally occurring isotopes of helium that only differ in the number of neutrons in the core, nevertheless, they are quite different: ^{4}He is a boson and ^{3}He is a fermion. The descriptions in this thesis usually refer to ^{4}He, as it is much more abundant ($> 99.999\,\%$). Further, in spite of its simple electronic structure ($1s^2$), helium shows some remarkable properties. For example, helium is the only element exhibiting a superfluid phase, where the atoms in the liquid cease to experience friction. The initial research interest in helium nanodroplets was to investigate if the peculiarities of bulk liquid helium can also be found in nanometer-sized droplets. The final temperature of the droplets was estimated [28] and, for ^{4}He, measured [29] to be at about 0.4 K. Consequently, superfluidity was shown for ^{4}He droplets while ^{3}He droplets are not superfluid [30].

In this chapter, the fundamental concepts for the experiment discussed in this thesis are presented. It is organized as follows: In Sec. 2.1, the formation of helium nanodroplets is described. Further, the possibility to embed foreign species inside the droplets is explained as a simple approach to produce heteronuclear systems. Sec. 2.2 gives an introduction to the theoretical treatment of superfluidity and the implications for rotating superfluids. An overview on the shapes of (normal liquid) rotating droplets is then given in Sec. 2.3. Finally, the interaction of intense light pulses with clusters and light scattering on small particles are presented in Sec. 2.4.

2.1 Helium Nanodroplets

Helium nanodroplets exhibit some very peculiar properties. In the course of their formation by supersonic expansion of gaseous or liquid helium into vacuum they cool down to a temperature of only a few hundred millikelvin above absolute zero. At this temperature, ^{4}He is in a superfluid state where the atoms do not experience any friction: a liquid with vanishing viscosity. In combination with the ability to embed foreign species of atoms or molecules, so-called *dopants*, inside helium nanodroplets and a very high heat conductivity, this makes them an ideal cryogenic matrix, since the dopant species get cooled very efficiently while being able to move freely inside the droplets.

In this section, an introduction to helium nanodroplets is given. A broader review is given by Toennies and Vilesov [26]. First, the physics of supersonic jets and generation of rare gas clusters are presented, followed by a discussion of the specific aspects of helium nanodroplet generation and doping.

2.1.1 Supersonic Jets and Condensation

Since the beginning of cluster research in the middle of the twentieth century, various techniques have been established to produce clusters consisting of all kinds of elements or molecules. A brief overview on different types of clusters and their generation is given, e.g., by Haberland [31]. In particular, rare gas clusters are weakly bound by *van der Waals forces*, i.e., interactions of dipoles induced by fluctuations of the electron shell. The interaction potential of two atoms at a distance r can be approximated by the *Lennard-Jones potential* $V_{\mathrm{LJ}}(r)$ (cf. Sec. 4.6 in Ref. [31]):

$$V_{\mathrm{LJ}}(r) = \epsilon_{\mathrm{LJ}} \left[\left(\frac{r}{r_{\mathrm{min}}} \right)^{-12} - 2 \left(\frac{r}{r_{\mathrm{min}}} \right)^{-6} \right], \tag{2.1}$$

where the minimum of the potential well is located at an internuclear distance $r = r_{\mathrm{min}}$ with the corresponding energy $V_{\mathrm{LJ}}(r_{\mathrm{min}}) = -\epsilon_{\mathrm{LJ}}$. The repulsive term ($\propto r^{-12}$) is due to overlapping electron orbitals, while the attractive term ($\propto r^{-6}$) describes the induced dipole interaction between the atoms. In order to establish a van der Waals bond, the atoms need to be cold enough that their thermal energy is sufficiently smaller than the potential well and they need to approach each other very closely. These conditions, a cold and dense gas, can be established by an adiabatic expansion of the gas at high pressure into vacuum, a method dating back to 1956 [32]. During this expansion an *atomic beam* reaching low temperatures will form. In the following, the underlying physics of atomic beams are briefly summarized (for a more detailed treatment see, e.g., Miller's chapter *Free Jet Sources* in the book *Atomic and Molecular Beam Methods* edited by Scoles [33]) before the condensation of clusters in the beam is described.

In Fig. 2.1 the expansion of a gas from a reservoir (also called *stagnation chamber*) through a small orifice into vacuum is schematically shown. The velocity of the individual atoms is indicated by small arrows. It can be seen that the random velocity of the atoms in the stagnation chamber is transferred into a directed flow during the expansion. Hence, the broad velocity distribution gets very narrow, i.e., all the atoms move at nearly the same speed. As the relative movement of the individual atoms is a measure for the temperature, a cold beam of atoms is produced.

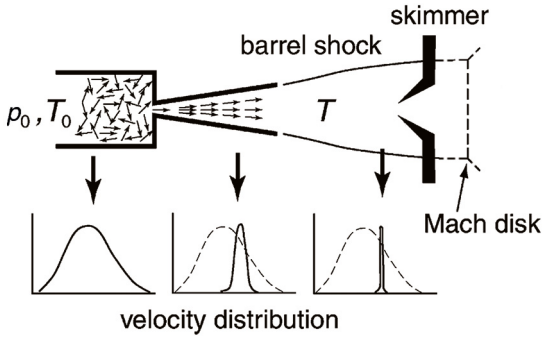

FIG. 2.1: Supersonic expansion of a gas into vacuum. The gas flows from a reservoir at pressure p_0 and temperature T_0 through a small orifice which leads to a very narrow velocity distribution and therefore to a low temperature T in the beam. The isentropic expansion of the gas is shielded by shock waves (*barrel shock* and *Mach disk*) from the background gas. In order to extract an undisturbed atomic beam, a skimmer has to be placed upstream of the Mach disk's position. Adapted from Ref. [34].

In the reservoir, the velocity of the atoms is much smaller than the local speed of sound v_s. In the case of an ideal gas at pressure p and density ρ_g,

$$v_\mathrm{s} = \sqrt{\gamma \frac{p}{\rho_\mathrm{g}}} = \sqrt{\frac{\gamma k_\mathrm{B} T}{m_\mathrm{g}}}, \tag{2.2}$$

where k_B is the Boltzmann constant, m_g is the mass of a single atom or molecule, and γ is the *adiabatic index*, which is the ratio of the specific heat at constant pressure c_p to the specific heat at constant volume c_v:

$$\gamma = \frac{c_\mathrm{p}}{c_\mathrm{v}} = 1 + \frac{2}{f}. \tag{2.3}$$

Here, f is given by the degrees of freedom of the gas atoms or molecules. For a monoatomic gas, only the translational degrees of freedom contribute, therefore $f = 3$ and $\gamma = 5/3$. The ratio of the velocity of the gas flow v_g to the local speed of sound is given by the *Mach number*

$$M = \frac{v_\mathrm{g}}{v_\mathrm{s}}. \tag{2.4}$$

In the course of the expansion, the Mach number increases: As the gas flows from the stagnation region that is at a high pressure p_0 into the vacuum that is at a low background pressure p_b, the local speed of sound decreases [$v_\mathrm{s} \propto \sqrt{p}$, cf. Eq. (2.2)]. Hence, given a sufficiently large pressure gradient, the flow changes from *sub*sonic ($M < 1$) to *super*sonic ($M > 1$). Sonic speed ($M = 1$) will be reached at the nozzle throat if the pressure ratio meets the condition [35]

$$\frac{p_0}{p_\mathrm{b}} \geq \left(\frac{\gamma + 1}{2}\right)^{\frac{\gamma}{\gamma - 1}}, \tag{2.5}$$

which is less than 2.1 for all gases. It is worth noting that for a subsonic flow an increase of the flow velocity is reached by decreasing the flow cross section while for a supersonic flow the velocity is increased when the flow cross section increases. Hence, in order to produce a supersonic beam, a convergent-divergent flow profile is needed. Further, as small pressure disturbances propagate at the speed of sound, the expanding gas in the

supersonic part of the beam does not interact with the background gas. Therefore, an undisturbed region forms along the beam axis, also called the *zone of silence*. At the boundaries of the beam, however, the pressure of the flowing gas has to adapt to the background pressure and the Mach number suddenly decreases. In consequence, shock waves form that interrupt the undisturbed expansion. These are called *barrel shocks* at the edges of the beam and *Mach disk* at the front of the expansion, cf. Fig. 2.1. The position x_{Mach} of the Mach disk downstream from the nozzle throat also depends on the pressure ratio and is given by [36]

$$\frac{x_{\mathrm{Mach}}}{d} = 0.67\sqrt{\frac{p_0}{p_\mathrm{b}}}, \tag{2.6}$$

where d is the nozzle diameter. In order to extract the unhindered beam, a conical aperture called *skimmer* (as it skims the beam) has to be introduced into the zone of silence. It has to be placed far enough upstream from the Mach disk position so that the beam is not disturbed. On the other hand, placing it closer to the nozzle lowers the mean free path length of the gas at the aperture, resulting in a decrease of the transmission probability through the skimmer [37]. However, when the undisturbed beam is extracted from the zone of silence, an ideal expansion into vacuum can be assumed.

The isentropic expansion of the gas is described as an adiabatic steady flow of an ideal gas using Bernoulli's equation [38]. The enthalpy of the gas in the reservoir H_0 is converted into that of the flow H and kinetic energy $m_\mathrm{g} v_\mathrm{g}^2/2$:

$$H_0 = H + \frac{1}{2} m_\mathrm{g} v_\mathrm{g}^2, \tag{2.7}$$

that can be related to the temperature using the specific heat capacity

$$c_\mathrm{p} T_0 = c_\mathrm{p} T + \frac{1}{2} m_\mathrm{g} v_\mathrm{g}^2. \tag{2.8}$$

The maximum velocity of the flow v_{max} is reached when all the enthalpy is converted into kinetic energy, i.e., when $H = c_\mathrm{p} T = 0$:

$$v_{\mathrm{max}} = \sqrt{\frac{2 c_\mathrm{p} T_0}{m_\mathrm{g}}} = \sqrt{\frac{\gamma}{\gamma - 1}\frac{2 k_\mathrm{B} T_0}{m_\mathrm{g}}} = \sqrt{\frac{5 k_\mathrm{B} T_0}{m_\mathrm{g}}} \quad \text{(for monoatomic gases)}. \tag{2.9}$$

Hence, the maximum velocity only depends on the temperature in the reservoir T_0. The temperature in the beam T can be calculated by rearranging Eq. (2.8) using Eqs. (2.4), (2.2), and $c_\mathrm{p} = c_\mathrm{v} + k_\mathrm{B}$, yielding:

$$T = T_0 \left[1 + \frac{1}{2}(\gamma - 1) M^2\right]^{-1}. \tag{2.10}$$

Thus, for large Mach numbers, the beam temperature gets very low and, given a sufficiently high density in the beam, cluster condensation starts.

In Fig. 2.2 the adiabatic expansion of the gas is schematically shown in a phase diagram. From the reservoir, where the gas is at the stagnation conditions p_0 and T_0 (point A), the pressure and temperature of the expanding gas changes along the adiabatic curve, eventually crossing the vapor pressure curve $p_\mathrm{v}(T)$ (point B). As the expansion continues along the adiabatic, the gas reaches a supersaturated state. With the onset

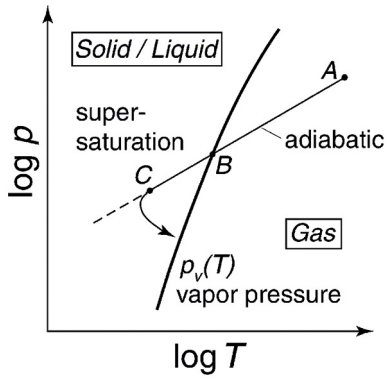

FIG. 2.2: Adiabatic expansion and supersaturation in the phase diagram. From point A, where the gas is at pressure p_0 and temperature T_0, the expansion follows the adiabatic curve, eventually crossing the vapor pressure curve $p_v(T)$ at point B. The gas reaches a supersaturated state, where condensation to clusters begins (point C), thus leaving the adiabatic and approaching the vapor pressure curve (see the small arrow). Adapted from Ref. [34].

of condensation (point C), the expanding gas departs from the adiabatic line and approaches the vapor pressure curve. The condensation is initiated by dimers forming in three-body-collisions:

$$\mathrm{A} + \mathrm{A} + \mathrm{A} \rightarrow \mathrm{A}_2 + \mathrm{A}. \tag{2.11}$$

While two atoms form a bond, the third atom evaporates carrying away excess momentum and binding energy. In the supersaturated gas the dimers act as condensation nuclei, where clusters start growing by successive addition of monomers. This will of course increase the cluster temperature and in order not to destroy the whole cluster, the condensation heat needs to be removed from the cluster via collisions or evaporation of single atoms. As long as the ratio of atoms to clusters in the beam is high, monomer addition is the predominant growth process; with an increasing number of clusters in the beam, coagulation of clusters becomes more important [34]. In general, these multiplicative growth processes lead to a log-normal distribution of cluster sizes [39]. However, since there is no rigorous theory available describing the kinetics of cluster growth in supersonic beams, the final size of the clusters is typically estimated using Hagena's scaling laws [40]. In this concept of *corresponding jets* the parameter Γ is defined where the expansion of a gas leads to similar final temperatures and condensation conditions [41]:

$$\Gamma = n_0\, d^q\, T_0^{0.25q-1.5} \quad (0.5 < q \leq 1), \tag{2.12}$$

where $n_0 = p_0/(k_\mathrm{B} T_0)$ is the particle density in the reservoir and the parameter q has been experimentally determined to be 0.85. Further, the dimensionless parameter Γ^* is defined in order to compare different gases [41]:

$$\Gamma^* = \frac{p_0\, d^{0.85}}{T_0^{2.2875}} \cdot \frac{1}{k_\mathrm{B}\, \Gamma_\mathrm{ch}}, \tag{2.13}$$

where Γ_ch is a characteristic parameter containing gas specific constants. Larger values of Γ^* lead to larger mean cluster sizes $\langle N \rangle$, i.e., in order to produce large clusters, the stagnation pressure p_0 has to be increased while the temperature in the reservoir T_0 needs to be decreased. Using the condensation parameter Γ^*, an empirical formula to

roughly predict the mean cluster size is given [42]:

$$\langle N \rangle = 33 \cdot \left(\frac{\Gamma^*}{1000} \right)^{2.35} . \tag{2.14}$$

It should be noted that for this formula, two modifications for small clusters [43] and large clusters [44] have been proposed. Overall, calculations based on these scaling laws have been very reliable to estimate the mean sizes for neon, argon, krypton, and xenon clusters. For typical expansion conditions needed to generate helium clusters, however, the assumption of an ideal gas is not longer valid and the scaling laws deviate. Therefore, the characteristics in the production of helium nanodroplets will be discussed in the following section.

2.1.2 Generation of Helium Nanodroplets

While the first observation of helium droplets was presumably made by Kamerlingh Onnes, who reported more than a hundred years ago a forming mist during the expansion of compressed helium [45], the first beam of condensed helium was reported by Becker *et al.* in 1961 [46]. In order to generate a free jet of helium droplets, expansion conditions close to the vapor pressure line have to be chosen. Since the *critical point*, located in the phase diagram at the upper end of this curve, is at a very low temperature and moderate pressure (for ^{4}He: $T_c = 5.1953\,\mathrm{K}$, $p_c = 2.2746\,\mathrm{bar}$ [47]), the modeling of the expansion cannot be based on the assumption of an ideal gas; instead, real-fluid properties have to be used [48]. This is rather surprising, as under standard conditions, helium is often given as an example for a nearly ideal gas. In Fig. 2.3 the phase diagram of ^{4}He is shown in the typical log-log representation, exhibiting some special properties of helium. It can be seen that there is no triple point, where the gas, liquid, and solid phase coexist. The solid phase is only reached at high pressures (above 25 bar), which means that helium remains liquid down to absolute zero. Therefore, helium clusters are the only rare gas clusters that are liquid (and accordingly called *helium nanodroplets*). Further, the liquid phase is divided by the *λ-Line* into a normal fluid ("HeI") and a superfluid ("HeII") phase. The isentropes based on real-fluid behavior are shown as dashed lines for different expansion conditions ($p_0 = 20\,\mathrm{bar}$, T_0 as indicated). While for high temperatures, the isentropes are straight lines and hence describe a nearly ideal expansion (i.e., as it is known for the other rare gases), for lower temperatures, the isentropes exhibit a curvature towards the vapor pressure line. Based on their appearance they can be grouped into three categories, representing different expansion regimes that correspond to ranges of decreasing temperature (cf. Fig. 2.3) [49]:

I. The isentropes resemble those of an ideal gas expansion and cross the vapor pressure curve from the gas phase to the liquid phase, thus reaching a supersaturated state. As described in Sec. 2.1.1, subsequent condensation in the beam leads to cluster formation. In this so-called *subcritical* expansion regime, small helium clusters are formed.

II. The isentropes pass close to the critical point, a process accompanied by considerable density fluctuations in the beam. Large clusters form in the course of this *critical* expansion because of a spontaneous separation into gas and liquid.

III. The isentropes exhibit a clear curvature and cross the vapor pressure line from the liquid side. This leads to the formation of gas bubbles in the liquid, a phenomenon

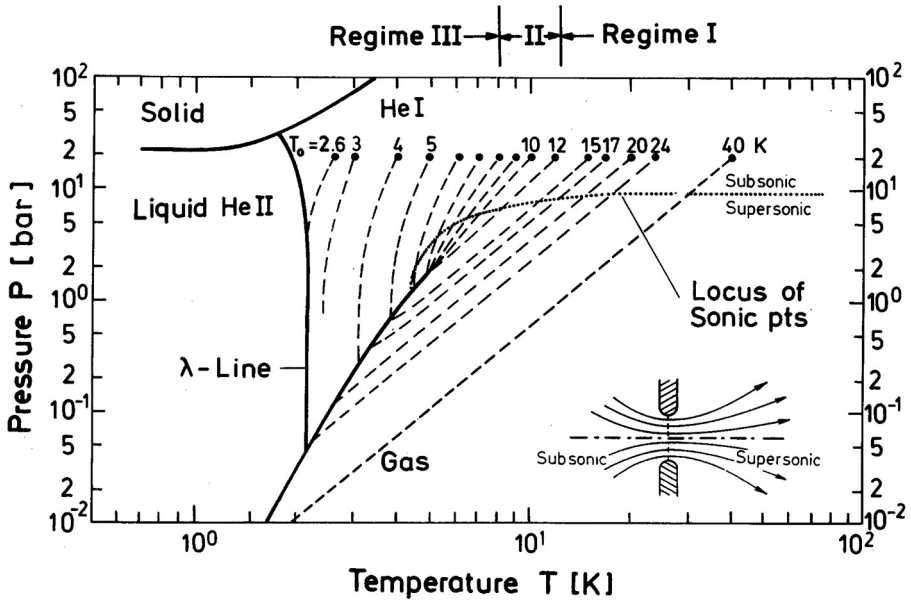

FIG. 2.3: Phase diagram of ^{4}He. The liquid phase is divided by the λ-Line in a normal fluid (HeI) and a superfluid (HeII) phase. The dashed lines are isentropes for different expansion conditions ($p_0 = 20\,\text{bar}$, T_0 as indicated). Three different expansion regimes can be identified: subcritical (Regime I), critical (Regime II), and supercritical (Regime III). For details see text. Reprinted from Ref. [49].

well known as *cavitation*, which ultimately results in the formation of very large helium droplets. The fragmentation of the liquid in this so-called *supercritical* expansion regime yields a size distribution with an exponential falloff [50].

It should be noted that extremely large clusters can be produced at even lower temperatures, where a continuous liquid jet of helium breaks up into droplets because of Rayleigh instabilities [51].

Overall, a quantitative description of the adiabatic expansion of helium is complex since quantum effects have to be considered that increase the collision frequency for low collision energies [52]. Further, the probability that a helium atom colliding with a helium cluster gets absorbed by the cluster (the *sticking probability*) is supposed to be close to unity [53]. This means that even for subcritical expansion conditions, Eq. (2.14) can only give a rough estimate of the mean droplet size but does, in general, not apply. Up to now, there is no rigorous scaling law for the expansion of helium from the liquid phase available, although a proposition has been made several years ago by Knuth and Henne [54]. Therefore, one can only resort to basic considerations: The cluster size increases with decreasing temperature, increasing stagnation pressure and increasing nozzle diameter. For example, in order to generate very large helium nanodroplets, a cluster source is needed where high pressure can be applied at cryogenic temperature. In order to keep sufficient vacuum conditions even when using a large orifice and applying a high stagnation pressure, a *pulsed* source can be used, where the gas is not continuously expanded into vacuum but in short gas pulses. For this type of cluster source extremely large droplet sizes of up to $\langle N \rangle \sim 1 \times 10^{12}$ and a considerably increased flux as compared to continuous sources have been reported [55, 56].

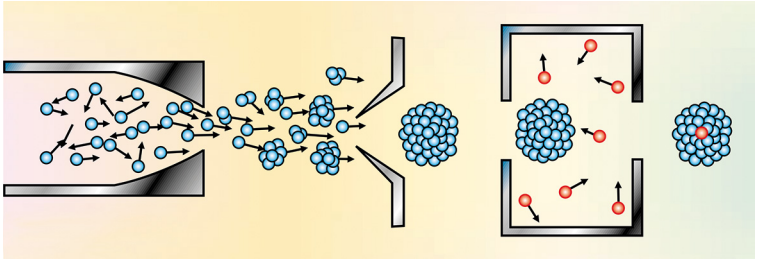

FIG. 2.4: Doping of helium nanodroplets. The droplets are produced by a supersonic expansion from a nozzle and subsequently extracted from the beam through a skimmer, before they enter a gas cell or an oven, where the dopants are picked up via collisions. Adapted from Ref. [62].

2.1.3 Doping of Helium Nanodroplets

The possibility to introduce *dopants*, i.e., foreign species (atoms or molecules), into helium nanodroplets has raised a lot of scientific interest. A dopant will form a bound state with the droplet upon collision. Because of the droplet's superfluid nature, the helium atoms that surround the embedded species perfectly adapt to the dopant's structure without hindering its rotation. In addition, the droplet's low temperature and large heat conductivity account for a very efficient cooling of the dopant, thus enabling high resolution spectroscopy [57] – especially since helium is transparent for a wide spectral range (from infrared to vacuum-ultraviolet). Also, the fundamental interaction of the dopant with the droplet, e.g., upon ionization, has been examined in great detail (for a review, see the article by Stienkemeier and Lehmann [58]). Further, by successive doping of helium nanodroplets, growth processes can be studied in an ultracold environment [59]. For example, the structure of metal clusters [60] and bimetallic core-shell nanowires [61] grown in helium nanodroplets have been investigated.

In Fig. 2.4, a typical setup for doping of helium nanodroplets is schematically shown. After production of the droplets by supersonic expansion and extraction of the beam through a skimmer, the droplets traverse a gas cell or oven where they collide with the dopants that they subsequently capture. This so-called *pick-up* technique pioneered in the group of Scoles [63] and was since used for a large variety of droplet size regimes as well as dopant numbers and species. Depending on their chemical potential, the dopants are either immersed in or reside on the surface of the helium droplet, a behavior that can be referred to as *heliophilic* or *heliophobic*, respectively [26]. Because of the additional heat introduced to the droplet by the picked up dopant, several helium atoms will evaporate from the droplet to maintain its low temperature. The number of dopants that get picked up by the droplet depends on the dopant species and the droplet size, their collisional cross section, as well as the number of collisions. Assuming a pick up probability of unity, successive capture and clustering of dopants in helium nanodroplets yields a Poissonian distribution [59]. For k atoms picked up by the droplet this gives the probability

$$P_k = \frac{(\tilde{z})^k}{k!} \exp(-\tilde{z}), \tag{2.15}$$

where $\tilde{z}$ is the average number of collisions [26] given by

$$\tilde{z} = n_{\mathrm{M}} \sigma_{\mathrm{coag}} L \frac{\overline{g}}{v_{\mathrm{D}}}. \tag{2.16}$$

Here, n_{M} is the density of the dopant gas in the cell of effective length L. The so-called "coagulation" cross section σ_{coag} is a measure for the dopant atoms getting successively picked up by the helium nanodroplet and forming a dopant cluster inside the droplet via monomer addition. The relative velocity $\overline{g} = (v_{\mathrm{D}}^2 + v_{\mathrm{M}}^2)^{1/2}$ is given by the velocities of the helium droplet v_{D} and the mean thermal velocity of the dopant gas

$$v_{\mathrm{M}} = \sqrt{\frac{8R_{\mathrm{gas}}T_{\mathrm{M}}}{\pi M_{\mathrm{M}}}}\,, \tag{2.17}$$

with R_{gas} the general gas constant, T_{M} the temperature of the dopant gas and M_{M} its molar mass. The actual number of collisions in the gas cell depends on the velocity of the helium droplet traversing the gas cell and is accounted for by the term $\overline{g}/v_{\mathrm{D}}$ [59]. Please note that this expression does not take into account the shrinking of the droplet that is due to the evaporation of helium atoms upon pick up of dopant atoms. For a large number of picked up atoms k, Eq. (2.15) approaches a Gaussian distribution

$$P(k) = \frac{e^{-(k-\tilde{z})^2/(2\tilde{z})}}{\sqrt{2\pi\tilde{z}}}\,, \tag{2.18}$$

with expectation and variance of $\tilde{z}$. In this case, the number of atoms picked up by the droplet is simply given by Eq. (2.16). This is exemplified in Fig. 2.5 for parameters reflecting the experimental conditions in this work.

At the same time, the droplets will evaporate helium atoms because of the additional binding energy and therefore shrink during the pick up process. The total energy introduced to a droplet upon collision is given by [59]

$$E_{\mathrm{tot}} = \langle E_{\mathrm{coll}} \rangle + E_{\mathrm{bind}}, \tag{2.19}$$

with the average thermal collision energy

$$\langle E_{\mathrm{coll}} \rangle = E_{\mathrm{int}}(\mathrm{M}) + \frac{3k_B T}{2} + \frac{M_{\mathrm{M}} v_{\mathrm{D}}^2}{2N_{\mathrm{A}}}\,. \tag{2.20}$$

It is the sum of the internal rovibrational energy of the dopant $E_{\mathrm{int}}(\mathrm{M})$ and the kinetic energy of the collision, with N_{A} the Avogadro constant. Please note that Eq. (2.19) does not take into account clustering of the foreign species inside the droplet. This might be negligible for a small amount of dopant atoms, but for large droplets picking up a substantial amount of dopants it is assumed to significantly contribute to the total energy. In Ref. [64], Gomez *et al.* proposed to include the bulk sublimation energy E_{M} as an estimate for the energy added by coagulation of the dopants inside the droplet:

$$E_{\mathrm{tot}} = \langle E_{\mathrm{coll}} \rangle + E_{\mathrm{bind}} + E_{\mathrm{M}}\,. \tag{2.21}$$

The number of helium atoms that evaporate from the droplet per dopant atom is then given by

$$\Delta N_{\mathrm{evap}} = \frac{E_{\mathrm{tot}}}{E_{\mathrm{He}}}, \tag{2.22}$$

where E_{He} is the binding energy of bulk liquid helium.

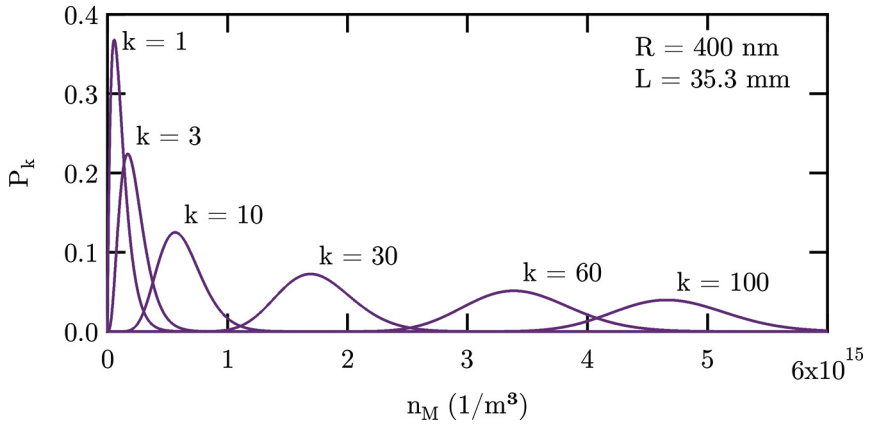

FIG. 2.5: Doping probability P_k versus particle density n_{M}, for a droplet radius $R = 400\,\mathrm{nm}$ and a collision length $L = 35.3\,\mathrm{mm}$. The successive capture and coagulation of dopants in a helium nanodroplet results in a Poissonian distribution for the probability P_k to pick up k atoms [59]. It can be seen that for large k the distribution becomes Gaussian.

2.2 Aspects of Superfluidity

The superfluid phase of helium is without doubt its most interesting property, being a macroscopic manifestation of quantum phenomena. In superfluid helium frictionless flow, an enormous thermal conductivity, and, given a rotation above some critical velocity, the appearance of vortex lines have been observed. In this section, the underlying physics will be briefly summarized, mainly based on two sources: An excellent overview given by Vinen [65] and a more detailed treatment that can be found in the book by Enss and Hunklinger [66]. In addition to this theoretical description, the fascinating history of the discovery of superfluidity is reviewed in an article from Balibar [67].

At the beginning of the twentieth century, helium was the last of the so-called *permanent gases* that would not condense [68]. In 1908, however, Kamerlingh Onnes achieved to liquefy helium in his low temperature laboratory at the University of Leiden, the Netherlands [69]. He found the boiling point at a temperature close to 4 K and, in subsequent studies, observed that helium remains liquid when cooled further down to 1.5 K [70]. Even at absolute zero, helium will not freeze because of its small mass and therefore large zero point energy [71], keeping the density of the fluid low while the interatomic forces are sufficiently strong to form a liquid phase. Further, at a temperature around 2.2 K, the density curve of helium showed a maximum, a sudden jump of the dielectric constant was noticed, and the specific heat curve exhibited a discontinuity. These observations led Keesom and Wolfke to suggest a phase transition between two liquids they called *helium I* and *helium II* [72]. The startling idea that helium, a weakly interacting gas lacking outstanding chemical properties, exhibits two different liquid states was backed by more precise measurements of the specific heat by Keesom and Clusius [73] and, subsequently, Keesom and Keesom [74]. In Fig. 2.6 the specific heat curve of liquid helium is shown. The pronounced peak at 2.19 K hints at the phase transition and since the shape of the curve resembles the Greek letter λ, it was suggested to call the point of the sudden increase in heat capacity the λ-*Point* [74]. The phase transition is accompanied by a clearly visible effect: The boiling of helium I, i.e., above the λ-Point temperature T_λ, will suddenly cease as soon as the temperature falls

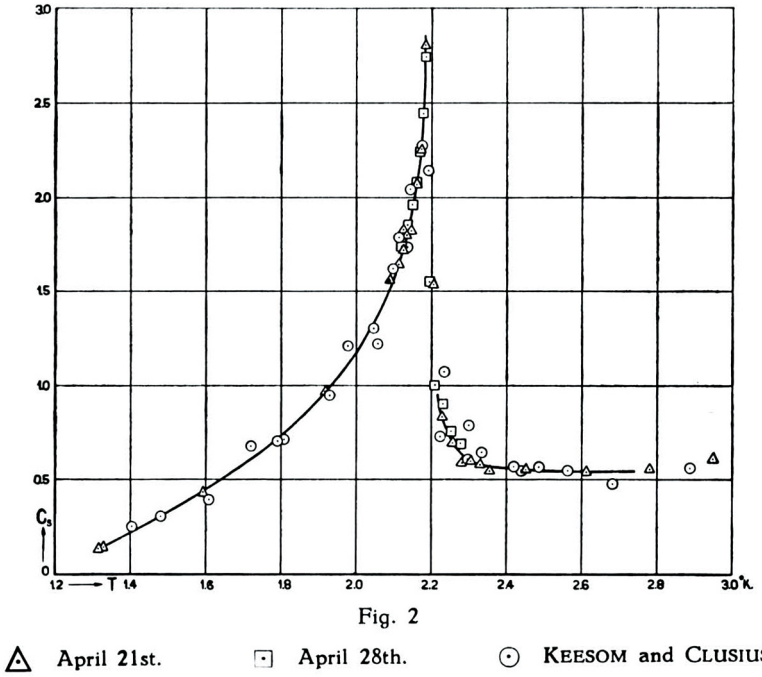

FIG. 2.6: Specific heat of liquid helium C_S versus temperature T. Close to $T = 2.2\,\mathrm{K}$ a sudden peak is observed, hinting at a phase transition in the liquid. Because of the curve's resemblance to the Greek letter λ, this is called the λ-Point with a corresponding temperature T_λ. It marks the transition of the normal liquid phase helium I ($T > T_\lambda$) to the superfluid phase helium II ($T < T_\lambda$). Reprinted from Ref. [74].

below T_λ [75]. This is, in fact, due to the large heat conductivity of helium II [76, 77] that leads to a homogeneous temperature throughout the liquid where evaporation only occurs at the surface. Several other phenomena have been observed in helium II. For example, when an empty beaker is lowered into a bath of helium II, the liquid will form a very thin film (called *Rollin film* [78]) covering the walls of the beaker and thus filling it until the height of the liquid surface in the beaker equals that of the bath. When the beaker is removed, the process will reverse and the helium II from inside the beaker will creep over its walls, dripping back into the bath until the beaker is completely emptied. Because of the Rollin film, helium II containers need to be completely sealed for the liquid not to leak out. Another astonishing observation is the *fountain effect* [79] where a flask with a thin neck is inserted into helium II. The bottom of the flask is open towards the helium bath but filled with a fine, compressed powder, i.e., the liquid helium has to flow through the powder to enter the flask. The thin neck sticks out of the liquid's surface. When the helium in the flask above the powder is heated, e.g., by a lamp, the helium gets ejected through the thin neck and a fountain of liquid helium forms. These two examples are closely linked to the superfluid nature of helium II.

Superfluidity was discovered in the course of two independent experiments addressing the viscosity of helium II by Kapitza [80] and, at the same time, by Allen and Misener [81]. Both works were published back to back in Nature. While Kapitza reasoned that the viscosity of helium II is at least 1500 times smaller than that of helium I and it could therefore be called a *superfluid*, Allen and Misener pointed out that the known hydrodynamic equations are not sufficient to describe the observed flow of helium II,

thus it would require an entirely new description. Nevertheless, the vanishing viscosity of helium below the λ-Point immediately gives an explanation of Rollin's film flow: As any other liquid, helium II gets attracted to the walls of its container by capillary forces, however, because of the weak interatomic forces in the liquid and since there is no viscous drag, unlike any other liquid it will form a thin film creeping along all surfaces it is in contact with until it completely covers the walls of its container. The fountain effect, on the other hand, is not sufficiently described by the frictionless flow of helium II alone. Further, a so-called *viscosity paradox* was observed: While liquid helium below the lambda point flows unhindered through thin capillaries, i.e., with zero viscosity, the oscillations of a torsion pendulum in helium II decay, resulting in a viscosity about an order of magnitude lower than air, but not zero. Therefore, it was concluded that a more sophisticated, radically new theory on superfluidity is needed that will be discussed in the following.

2.2.1 The Two-Fluid Model

A first attempt to describe the superfluid flow of helium II was made by London and Tisza. Since ^{4}He is a boson, London suggested to consider the superfluid phase of helium as a form of Bose-Einstein-Condensation, a theoretical concept for an ideal gas of non-interacting bosons: Below a critical temperature T_{BEC}, a fraction of the particles condense into the ground state and can thus be described by a single macroscopic wavefunction. This ordering process is reflected by the specific heat below the λ-Point that London calculated for a Bose-Einstein condensate of helium atoms. The resulting curve showed some qualitative agreement with the experimental data [82]. Further, he found a critical temperature of $T_{\mathrm{BEC}} \approx 3.1\,\mathrm{K}$ which is close to the measured value $T_\lambda \approx 2.2\,\mathrm{K}$. Based on London's theory, Tisza proposed that helium II consists of two components: A normal fluid one, whose atoms are distributed over all excited states, and a superfluid one, whose atoms are all condensed to the ground state [83]. The concentration of the superfluid component continuously increases from zero at $T = T_{\mathrm{BEC}}$ to unity at $T = 0$ (while the concentration of the normal fluid component decreases). Since the condensed atoms are in the ground state they are not able to dissipate momentum and the viscous behavior of helium II is exclusively linked to the fraction of non-condensed atoms [83]. This idea of helium II consisting of two fluids was later reformulated in a famous paper by Landau [84], who was strongly opposed to consider liquid helium as an ideal gas of non-interacting atoms forming a Bose-Einstein condensate, arguing that the condensed atoms would collide with the excited atoms when moving through the liquid and therefore experience friction. Instead, he proposed collective excitations of quasiparticles he called *phonons* and *rotons* in the liquid causing the viscous behavior of the normal component. Superfluid behavior, on the other hand, is exhibited by the liquid if the flow velocity is too small to excite phonons or rotons, i.e., when no energy can be dissipated. Therefore, the superfluid component can be identified as the part of the liquid that remains in its ground state (i.e., the condensate in Tisza's model) [85].

In a simple picture, this can be exemplified by an object of mass m traversing a resting liquid with an initial velocity $\boldsymbol{v}_{\mathrm{e}}$ [86], as shown in Fig. 2.7 (a). When the object creates an excitation of energy ϵ and momentum $\hbar\boldsymbol{k}$ (where $\hbar$ is the reduced Planck constant and $\boldsymbol{k}$ is the wave vector of the excitation) in the liquid, the object's kinetic energy is decreased, thus it moves at a smaller final velocity $\boldsymbol{v}_{\mathrm{f}}$, cf. Fig. 2.7 (b). Considering

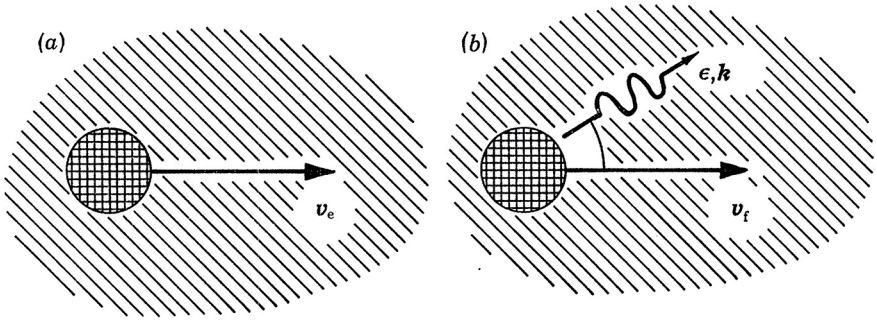

FIG. 2.7: Schematic of an object moving through a liquid. (a) The object moves with an initial velocity $\boldsymbol{v}_\mathrm{e}$. (b) Creating an excitation with energy ϵ and momentum $\hbar\boldsymbol{k}$ will reduce the object's kinetic energy and therefore its final velocity to $\boldsymbol{v}_\mathrm{f}$. Reprinted from Ref. [86].

conservation of energy and momentum yields

$$\frac{1}{2}mv_\mathrm{e}^2 = \frac{1}{2}mv_\mathrm{f}^2 + \epsilon \tag{2.23}$$

and

$$m\boldsymbol{v}_\mathrm{e} = m\boldsymbol{v}_\mathrm{f} + \hbar\boldsymbol{k}. \tag{2.24}$$

Inserting the final velocity $\boldsymbol{v}_\mathrm{f} = \boldsymbol{v}_\mathrm{e} - \hbar\boldsymbol{k}/m$ from Eq. (2.24) into Eq. (2.23) gives

$$\frac{1}{2}mv_\mathrm{e}^2 = \frac{1}{2}m\left(v_\mathrm{e}^2 - \frac{2\hbar}{m}\boldsymbol{v}_e\cdot\boldsymbol{k} + \frac{\hbar^2k^2}{m^2}\right) + \epsilon \tag{2.25}$$

which can be rearranged to

$$v_\mathrm{e}\cos\vartheta = \frac{\epsilon}{\hbar k} + \frac{\hbar k}{2m} \tag{2.26}$$

using $\boldsymbol{v}_e\cdot\boldsymbol{k} = v_\mathrm{e}k\cos\vartheta$ where ϑ is the angle between $\boldsymbol{v}_\mathrm{f}$ and $\boldsymbol{k}$. Since $\cos\vartheta \leq 1$ it follows

$$v_\mathrm{e} \geq \frac{\epsilon}{\hbar k} + \frac{\hbar k}{2m}, \tag{2.27}$$

which is the condition for simultaneous conservation of energy and momentum in the process. This means that there is a minimum initial velocity $v_\mathrm{e,min}$ of the object below which no excitations can be created in the liquid and hence no dissipation of energy can occur,

$$v_\mathrm{e,min} = \left(\frac{\epsilon}{\hbar k} + \frac{\hbar k}{2m}\right)_\mathrm{min}. \tag{2.28}$$

Assuming that the second term is negligible in comparison with the first term, a critical velocity v_L can be given,

$$v_\mathrm{L} = \left(\frac{\epsilon}{\hbar k}\right)_\mathrm{min}, \tag{2.29}$$

which is called the *Landau velocity*. A liquid can only show superfluid behavior if the Landau velocity is non-zero, $v_\mathrm{L} > 0$, which depends on the form of the liquid's dispersion relation $\epsilon(k)$. For an ideal Bose gas, the energy of the excited states simply equals the kinetic energy of a free particle, i.e., the dispersion relation is $\epsilon = \hbar^2k^2/(2m)$. Therefore, the Landau velocity is zero, $v_\mathrm{L} = [\epsilon/(\hbar k)]_\mathrm{min} = [\hbar k/(2m)]_\mathrm{min} = 0$, and excitations can be created for any given momentum, which means that energy can be dissipated for any given flow velocity. In liquid helium, however, interactions between the particles have

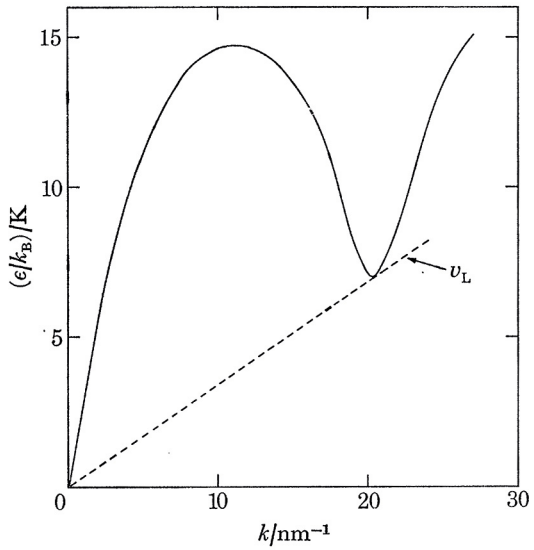

FIG. 2.8: Dispersion curve of liquid helium II. The excitation energy ϵ is shown versus the magnitude of its wave vector $\boldsymbol{k}$. For low momenta $\hbar k$ the nearly linear slope of the phonon branch can be seen. The parabola-shaped roton branch is located at higher momenta. Its minimum gives the minimum velocity needed to create excitations, the Landau velocity $v_L \approx [\epsilon/(\hbar k)]_{\min}$. Reprinted from Ref. [86].

to be considered. Landau suggested a linear dispersion for low momenta, leading to low-energy excitations he called phonons, and a quadratic dispersion for high momenta with an energy gap, i.e., a minimum energy Δ_r is needed for higher energy excitations Landau called rotons. In Fig. 2.8, a measured dispersion curve of liquid helium II is shown that turned out to match Landau's qualitative prediction. At low momenta, the linear slope of the phonon branch can be seen while at higher momenta, the roton branch is located exhibiting a parabola-like form. The Landau velocity v_L is given at the minimum of the roton branch (while the slope of the phonon branch corresponds to the speed of sound). Inserting experimental values [87] yields $v_L \approx 58\,\mathrm{m\,s^{-1}}$. The breakdown of superfluidity above the critical velocity v_L has been experimentally verified by Allum *et al.* [86]. It should be noted that the specific dispersion relation is not the only criterion for superfluidity: In order to transport the mass without friction, also a condensate must exist [88].

In the two-fluid model, liquid helium II consists of two interpenetrating fluids, the normal component with density ρ_n, velocity $\boldsymbol{v}_n$, entropy S_n, and viscosity η_n, and the superfluid component with density ρ_{sf}, velocity $\boldsymbol{v}_{sf}$, entropy $S_{sf} = 0$, and viscosity $\eta_{sf} = 0$, i.e., the superfluid component flows without viscosity while the normal component carries all the entropy and viscosity greater than zero. Within this model, the fountain effect mentioned above can be easily understood: Upon heating of helium II, the superfluid component turns into the normal fluid component, i.e., the respective densities ρ_{sf} and ρ_n change. This leads to a concentration gradient within the helium bath that is compensated by a flow of the normal component away from the heat source and a *counterflow* of the superfluid component towards the heat source. As shown in Fig. 2.9 (a) for flask with a compressed powder at the bottom, the flow of the normal component out of the flask is blocked while the counterflow of the superfluid component into the flask is not. As long as the heating is maintained, the continuous inflow of superfluid helium leads to an ejection of the liquid through the flask's thin neck, hence a fountain of liquid helium

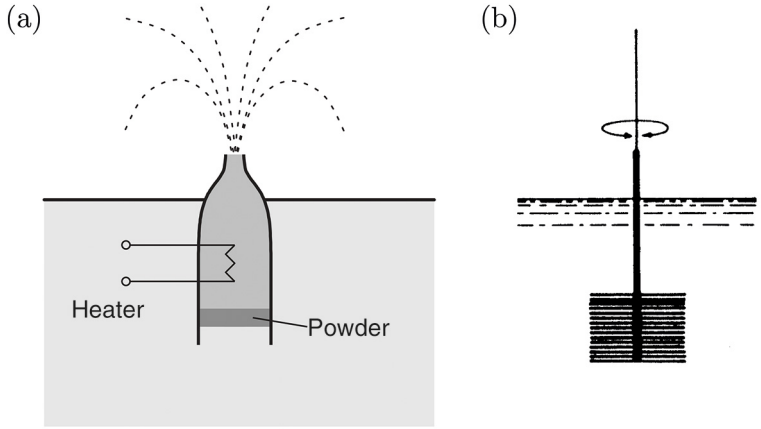

FIG. 2.9: (a) The fountain effect. A flask with a bottom consisting of a compressed powder is put into a bath of liquid helium. When the flask gets heated, a fountain can be observed. Reprinted from Ref. [66]. (b) The Andronikashvili experiment. A torsion pendulum equipped with a stack of equally spaced thin disks is put into a bath of liquid helium. The dampening of its oscillations is correlated to the concentration of the normal liquid component. Reprinted from Ref. [91].

can be observed. Further, the large heat conductivity of helium II can be attributed to this efficient counterflow. Since the normal and superfluid component do not have to move together, a new type of sound wave can occur called *second sound*. In contrast to a *first sound* wave, where $\boldsymbol{v}_\mathrm{n}$ and $\boldsymbol{v}_\mathrm{sf}$ move in phase leading to an oscillation of density and pressure, just like in an ordinary liquid, a second sound wave in helium II is an oscillation of temperature and entropy where $\boldsymbol{v}_\mathrm{n}$ and $\boldsymbol{v}_\mathrm{sf}$ move in antiphase, i.e., density and pressure remain almost constant. Therefore, in helium II, temperature is transported by waves instead of dissipation resulting in a large thermal conductivity. The aforementioned viscosity paradox is also resolved by the two-fluid model: Below T_λ, the superfluid component flows unhindered through small cracks and thin capillaries, while in the case of the torsion pendulum, the remaining normal component imposes a viscous drag and therefore dampens the oscillation. The latter effect was used by Andronikashvili to measure the reduction of the normal component's concentration in helium II with decreasing temperature [89]. A schematic of the experiment is shown in Fig. 2.9 (b). The torsion pendulum was equipped with a stack of 50 thin disks equally spaced at 0.2 mm from each other. As only the normal fluid and not the superfluid component gets dragged by the disc stack, the dampening of the pendulum's oscillation is correlated to the concentration of the normal fluid component. Fifty years later, an experiment termed the "Microscopic Andronikashvili Experiment" [30] was performed using helium nanodroplets to determine how many ^{4}He atoms are needed to exhibit superfluidity. Therefore, the rotation of a molecule embedded in a helium nanodroplet consisting of (non-superfluid) ^{3}He and (superfluid) ^{4}He atoms at varying concentration was measured. It turned out that at a minimum number of 60 ^{4}He atoms the molecule can rotate without friction, which nicely matched the theoretical prediction [90].

2.2.2 Rotation and Formation of Vortices

One of the most astonishing consequences of superfluidity is the formation of vortices in a rotating liquid. This section gives a brief description of this phenomenon, for a

comprehensive overview see the text book by Donnelly [92]. As a measure of rotation, the circulation of a fluid is given by the curl of its velocity field $\boldsymbol{v}_\mathrm{l}$, also known as the vorticity ω_v [92]:

$$\omega_\mathrm{v} = \operatorname{curl} \boldsymbol{v}_\mathrm{l}. \tag{2.30}$$

Since a superfluid flows with zero viscosity, no shearing forces and therefore no turbulence occur. Hence, Landau assumed in his two-fluid model that the flow of the superfluid component is irrotational, i.e.,

$$\operatorname{curl} \boldsymbol{v}_\mathrm{sf} = 0. \tag{2.31}$$

In 1955, Feynman chose a microscopic approach (i.e., solving the Schrödinger equation) to describe superfluid helium, resulting in the prediction of quantized vortices as possible excitations below the Landau velocity [93]. The following considerations are based on Ref. [66]. Coming back to London's original idea of interpreting the superfluid transition in liquid helium as a form of Bose-Einstein condensation, the condensate's macroscopic wavefunction describing the movement of the atoms condensed in the ground state is given as

$$\psi(\boldsymbol{r}) = \psi_0 \, \mathrm{e}^{i\varphi(\boldsymbol{r})}. \tag{2.32}$$

Here, ψ_0 is the amplitude that is assumed constant and $\varphi(\boldsymbol{r})$ is the position-dependent phase that is related to the velocity of the atoms in the superfluid component. The momentum $\boldsymbol{p}$ of a condensed atom can be described by [66]

$$-i\hbar\nabla\psi = \boldsymbol{p}\psi. \tag{2.33}$$

Since the momentum of an atom in the superfluid component can be identified as $m_4\boldsymbol{v}_\mathrm{sf}$ (where m_4 is the effective mass of a ^{4}He atom), inserting Eq. (2.32) into Eq. (2.33) gives $\boldsymbol{p} = \hbar\nabla\varphi(\boldsymbol{r}) = m_4\boldsymbol{v}_\mathrm{sf}$ and therefore

$$\boldsymbol{v}_\mathrm{sf} = \frac{\hbar}{m_4}\nabla\varphi(\boldsymbol{r}), \tag{2.34}$$

meaning that the superfluid velocity depends on the gradient of the phase. For the possible motion of the condensate, it immediately follows

$$\operatorname{curl} \boldsymbol{v}_\mathrm{sf} = \nabla \times \boldsymbol{v}_\mathrm{sf} = \frac{\hbar}{m_4}\nabla \times \nabla\varphi(\boldsymbol{r}) = 0, \tag{2.35}$$

which is the curl-free constraint from Eq. (2.31). In consequence, the local motion of the superfluid component has to be free of rotation, meaning that a superfluid in a rotating cylinder should stay at rest. In contrast to a normal fluid liquid that would form a parabola-shaped meniscus in a rotating container, a flattened surface is expected for helium II, since the superfluid component does not participate in the rotation and hence the centrifugal force is reduced. In Fig. 2.10 (a), the layout of such a rotating bucket experiment carried out by Osborne [94] is shown. As is already indicated in the sketch, it turned out that the meniscus of the superfluid exhibits the same parabola-shape as one would expect for a normal liquid. This unanticipated result can be understood by considering the hydrodynamic circulation κ of the superfluid along a contour C that is given for a single connected region by the line integral

$$\kappa = \oint_C \boldsymbol{v}_\mathrm{sf} \, \mathrm{d}\boldsymbol{l}. \tag{2.36}$$

In the superfluid, the contour can be continuously contracted to a point, yielding

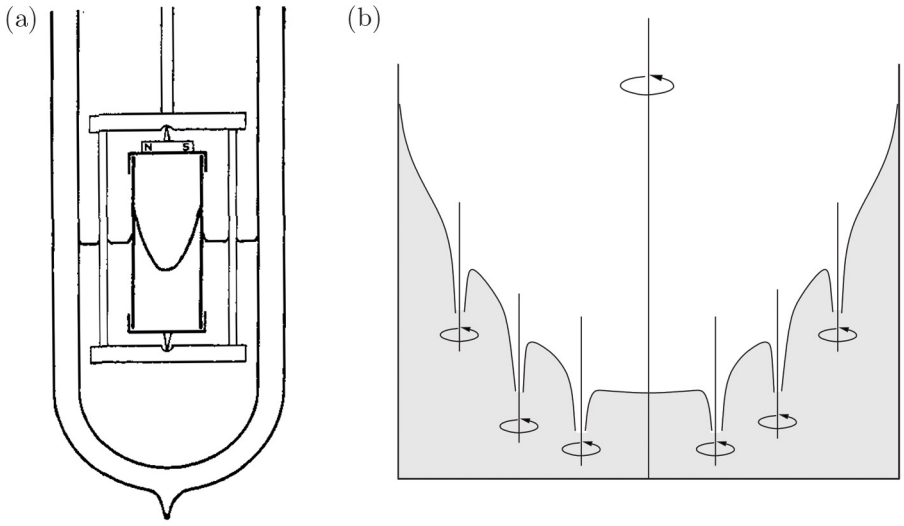

FIG. 2.10: Formation of vortices in a rotating bucket filled with superfluid helium. (a) Rotating bucket experiment. The helium II inside the inner cylinder exhibits a parabola-shaped meniscus upon rotation. Reprinted from Ref. [94]. (b) In a rotating container filled with superfluid helium, vortices form carrying the rotational energy. The liquid helium close to the vortex cores is normal fluid, i.e., the vortices impose the parabola shape on the liquid's surface. Reprinted from Ref. [66].

zero circulation, unless there is a singularity or hole within the contour (e.g., helium II circulating in a torus). In the latter case, using Eq. (2.34), the circulation becomes

$$\kappa = \oint_C \frac{\hbar}{m_4} \nabla\varphi(\boldsymbol{r})\, \mathrm{d}\boldsymbol{l} = \frac{\hbar}{m_4} \Delta\varphi_c, \tag{2.37}$$

with $\Delta\varphi_c$ the phase difference along the contour C. Since the wavefunction must be single-valued, the phase change for a complete cycle can only be an integer multiple of 2π, hence $\Delta\varphi_c = 2\pi n_\varphi$ and therefore

$$\kappa = \frac{h}{m_4} n_\varphi \qquad (n_\varphi = 0, 1, 2, \dots), \tag{2.38}$$

which means that the circulation is quantized in multiples of h/m_4 (with h the Planck constant). This quantization has been experimentally demonstrated by Vinen [95] in a cylinder filled with liquid helium II and a thin wire placed in the center. For a singly connected region in helium II, as in Osborne's rotating bucket experiment, the superfluid component seems to rotate because of vortex lines that form in the liquid. The superfluid velocity increases with decreasing distance to the vortex center and as soon as it exceeds the Landau velocity v_L, a normal fluid is formed in vicinity of the vortex core. Therefore, the vortices act as holes in the superfluid component. In Fig. 2.10 (b), the situation is shown for a rotating bucket filled with helium II. The forming vortices impose the classical parabola shape on the superfluid meniscus. The energy of a vortex increases quadratically with the circulation, it is therefore energetically favorable to have multiple vortices with $n_\varphi = 1$ instead of fewer vortices with larger circulation. Further, the vortices repel each other, thus forming vortex arrays as shown in Fig. 2.11. It is the top view of a rotating cylinder filled with helium II, where the number of vortices increases with the cylinder's angular velocity. The diameter of the dark circles corresponds to the cylinder diameter which is about 2 mm, hence the quantized vortex lines indeed

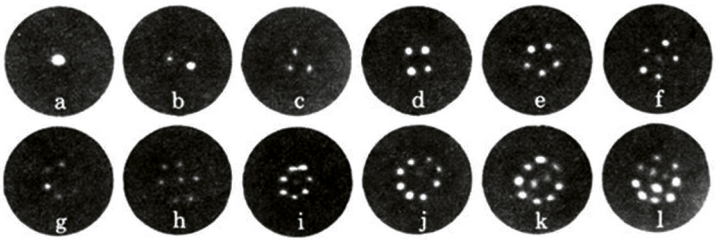

FIG. 2.11: Vortex arrays in bulk superfluid helium. Top view of a rotating cylinder filled with helium II. As the camera co-rotates with the cylinder, static vortex arrays are observed. The number of vortices increases with increasing angular velocity of the cylinder. Adapted from Ref. [98].

demonstrate a quantum phenomenon on a macroscopic scale. In the context of helium nanodroplets, after a long-lasting discussion whether vortices do exist in the droplets or not, similar vortex lattices have been observed [12, 96, 97].

2.3 Shapes of Rotating Droplets

The study of rotating masses dates back to Newton [99] who investigated the deformation of the planets that is due to rotation, concluding that the distance between the poles must decrease while the diameter at the equator will increase, hence the equilibrium shape will be oblate. In 1843, Plateau conducted an experimental study on the equilibrium shapes of a rotating liquid drop held together by surface tension that was suspended in an immiscible fluid chosen in such a way to keep the drop at neutral buoyancy [100]. By rotating the vessel containing the fluid and the drop, he was able to observe a multitude of deformations, among them ellipsoidal and dumbbell-like, i.e., prolate, shapes. However, the drop was not free of interactions with the fluid. Subsequent experimental and theoretical work of many contributors led to a rigorous characterization of the equilibrium shapes of freely rotating liquid drops. It turned out they are suitable for describing systems of very different dimensions such as atomic nuclei and black holes that are normally not accessible in the laboratory, thus liquid drop models are of interest to several disciplines of physics [101]. In the following, a brief summary on the shapes of normal liquid rotating drops will be given with a short consideration of superfluid droplet shapes.

In general, a liquid drop is held together by surface tension and exhibits a spherical shape at rest. When angular momentum is applied, the shape of the droplet will deform until the centrifugal force is balanced by the surface tension. An analytical solution for the equilibrium shapes of rotating drops is given by Chandrasekhar [102]. This model is restricted to oblate spheroids, i.e., *axisymmetric* or *biaxial* shapes. The degree of deformation of the drop as compared to a sphere is given by the dimensionless parameter Σ:

$$\Sigma = \frac{\rho_{\mathrm{D}} \omega_{\mathrm{a}}^2 a^3}{8\sigma_{\mathrm{D}}}, \tag{2.39}$$

where ω_{a} is the angular velocity, a is the equatorial radius of the drop, ρ_{D} its density, and σ_{D} its surface tension. In Fig. 2.12, the upper right quadrant of the calculated shape outline for increasing Σ is shown, with z the polar axis and $\bar{\omega}$ the equatorial axis. As can be seen, at $\Sigma = 0$ the shape is a sphere that will flatten at the poles for

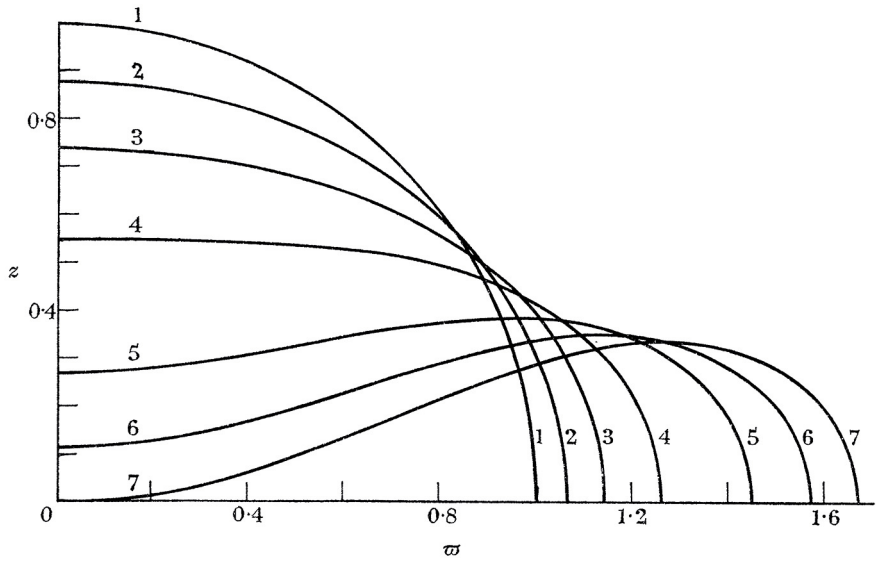

FIG. 2.12: Axisymmetric equilibrium shapes of rotating liquid drops based on the analytical model by Chandrasekhar [102]. The polar radius z is shown versus the equatorial radius $\bar{\omega}$ for increasing values of the parameter Σ. The curves labeled $1, 2, \ldots, 7$ are for $\Sigma = 0$, 0.21, 0.51, 1.0, 1.73, 2.1, and 2.33, respectively. At rest ($\Sigma = 0$) the drop is forming a sphere. With increasing Σ, the drops become more and more oblate, approaching a toroidal shape for $\Sigma > 1$. Nevertheless, the axisymmetric configuration becomes unstable at $\Sigma = 0.4587$. Reprinted from Ref. [102].

increasing Σ. For $\Sigma > 0.4587$, the oblate shape configuration becomes unstable. In Fig. 2.13 (a) a stability diagram for rotating droplet shapes based on the calculations of Brown and Scriven [103] is shown. The solid lines represent the stable configurations, while the solutions along the dashed lines are unstable. The shapes are characterized by the dimensionless angular velocity Ω_a:

$$\Omega_a = \sqrt{\frac{3\rho_D V}{32\pi\sigma_D}} \cdot \omega_a, \tag{2.40}$$

where V is the droplet volume. With increasing angular momentum (given by the dimensionless parameter L), the shapes evolve from a sphere ($\Omega_a = 0$) to more and more flattened spheroids along the oblate branch. At $\Omega_a \approx 0.56$, the stability limit is reached and the oblate configuration will rearrange to a prolate one. When the angular momentum is increased beyond the bifurcation point at $L \approx 0.3$ and $\Omega_a \approx 0.56$ the drops evolve along the prolate branch, exhibiting *triaxial* and two-lobed shapes until they eventually disintegrate into two separate spheres. The stability diagram was confirmed in microgravity experiments during space shuttle flights [104, 105]. Also, higher bifurcations could be shown in an experiment using diamagnetically levitated water droplets that were additionally stabilized by surface waves beyond the two-lobed bifurcation point [106]. In Fig. 2.13 (b), the results of an experimental study on levitated rotating wax droplets [107] are shown. After the droplets solidified, the lengths of their principal axes a, b, c and their volume V could be determined and compared to theoretical models. The inset pictures of the droplets nicely show the evolution from spherical and spheroidal (oblate) to triaxial and two-lobed (prolate) droplets (note the inverse axis since $a \propto L$).

In contrast to a normal liquid drop, a superfluid drop cannot rotate as a rigid body

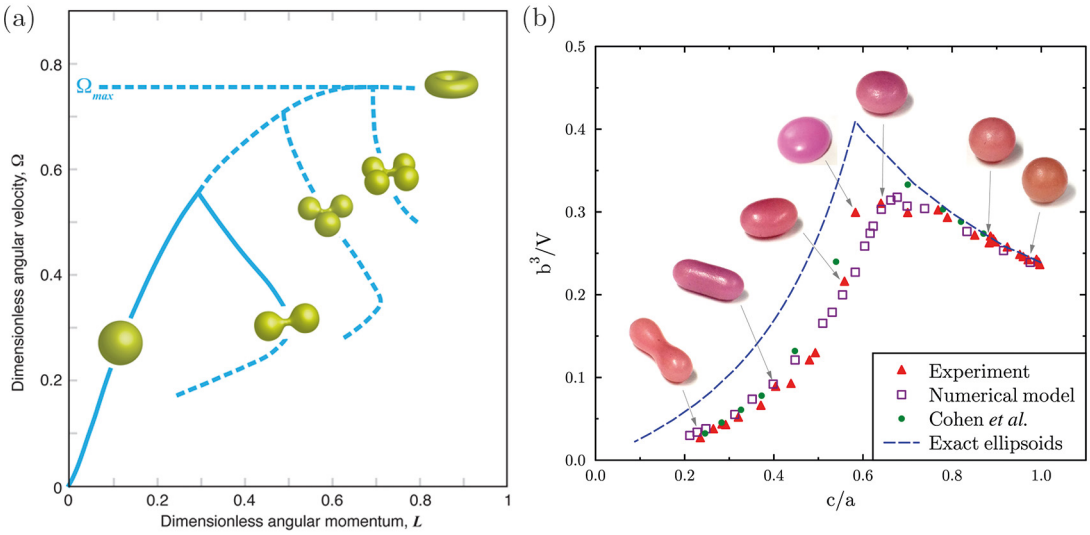

FIG. 2.13: Shapes of classically rotating droplets. (a) Evolution of the dimensionless angular velocity Ω_a with increasing dimensionless angular momentum L. The solid lines represent stable equilibrium shapes with a transition from oblate to prolate shapes at $\Omega_a \approx 0.56$. The dashed lines are unstable configurations. Reprinted from Ref. [101]. (b) Ratios of the droplets' principal axes a, b, c, and volume V. Comparison of measured wax droplet shapes (triangles), numerical model (squares), calculated ratios reported by Cohen *et al.* [108] (circles), and exact ellipsoids (dashed line). Reprinted from Ref. [107].

because of its vanishing viscosity. Hence, angular momentum is expected to be stored in surface waves [109] or quantized vortices inside the drop [110, 111]. Such vortices have been recently observed in superfluid helium nanodroplets [12, 112], however, it is not clear a priori whether they influence the shape of the droplets or not. In a study employing density functional theory it was pointed out that vortices could stabilize the droplets beyond the classical limit, i.e., extremely oblate ("wheel-like") shapes could occur [113]. The vortex ends have to meet the droplet surface perpendicularly resulting in a bending of the vortex lines. Large angular momentum is accompanied by a large number of vortices exhibiting only a small bending because of the flat, almost parallel surfaces of the extremely deformed droplet. The outline of the two-dimensional projection of these deformed droplet shapes accurately matches experimental data [12] and the classically unstable wheel-shaped droplets have been further examined in a subsequent study [15]. On the other hand, also prolate shapes have been qualitatively reported for superfluid helium nanodroplets based on characteristic features in scattering images [15, 22]. However, from the shape projection alone it is often not feasible to distinguish whether a shape is extremely oblate (i.e., wheel-like) or prolate (i.e., pill-shaped). Therefore, one aim of this thesis is to provide a complete three-dimensional characterization of spinning superfluid droplet shapes.

2.4 Light-Cluster Interaction

Clusters, in particular rare gas clusters, are often considered as ideal model systems to study fundamental interactions of radiation with matter [114–117]. While these clusters have a density close to that of a solid state target, they exist in the gas phase. Therefore,

energy introduced to the system, e.g., by irradiation with a strong light field, will fully act on the system without dissipation to a substrate or to the bulk [114, 116]. A high radiation dose leads to the formation of a *nanoplasma* in the cluster within only a few femtoseconds, typically followed by an expansion or even complete destruction of the sample [114, 115, 118]. The dynamics triggered by the light field depend on the field itself (i.e., its intensity, photon energy, and duration), but also on the cluster size and material (e.g., because of different ionization potentials and electronic resonances as well as differences in the fragmentation of homo- and heteronuclear samples). In this sense, each cluster can be seen as a nanometer-sized laboratory, offering to explore its basic properties and the specific light induced dynamics.

With the availability of intense laser pulses in the infrared and optical regime, the interaction of strong light fields with clusters could be studied, offering to investigate ultrafast many-particle dynamics [115]. However, at the beginning of this century, the advent of short-wavelength light sources [i.e., *free-electron lasers* (FELs), cf. Sec. 3.1] delivering ultrashort pulses with power densities of up to $1 \times 10^{18}\,\mathrm{W\,cm^{-2}}$ opened up unprecedented possibilities to study nanometer-sized systems. For example, instead of averaging over an ensemble of clusters with different sizes, compositions, and shapes, it has become feasible to investigate within a single exposure an individual cluster in so-called *single-shot single-cluster* experiments. These studies mainly aim at gaining a better understanding of (i) growth processes by investigating the cluster morphology, (ii) electron dynamics by exploring changes of the optical constants, (iii) ionization processes by analyzing the charge states of ionic fragments, and (iv) fragmentation dynamics by employing time-resolved imaging techniques. A detailed overview is given, e.g., in the book chapter by Bostedt, Gorkhover, Rupp, and Möller [119]. Among the first of such experiments were measurements addressing the nanoplasma dynamics in rare gas clusters: Upon irradiation, transient changes of the clusters' electronic configuration were observed [120], refractive core-shell structures could be identified [121], and the hydrodynamic expansion [122] as well as the highly charged ionization fragments [123] of individual rare gas clusters were investigated. Further, the temporal evolution of the clusters was explored in *pump-probe* experiments, where an initial light pulse (e.g., from an infrared laser) excites the system and, after a variable time delay, a second light pulse (e.g., from a short-wavelength light source) probes the state of the system. In such experiments, a softening of the cluster surface was observed on the femtosecond timescale [124], and the fragmentation dynamics of rare gas clusters were imaged on a pico- to nanosecond timescale [125].

This thesis reports on superfluid helium nanodroplets exposed to intense light fields leading to ionization of the droplets and subsequent nanoplasma formation followed by droplet fragmentation. Further, the droplet shapes were investigated by recording the signal of extreme ultraviolet light pulses scattered by the droplets in forward direction. As an introduction to the interaction of light with clusters, the fundamental concepts for ionization mechanisms and nanoplasma dynamics as well as light scattering on small particles are briefly summarized in the following.

2.4.1 Ionization Mechanisms

The ionization of clusters starts with the ionization of individual atoms. Especially at the beginning of the light pulse, the cluster environment does not influence the coupling of the light pulse to the atoms, therefore they can be regarded as if they were

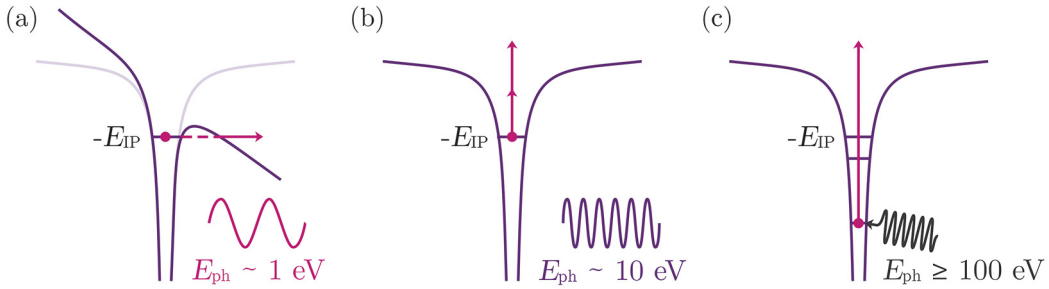

FIG. 2.14: Photon energy dependent ionization processes. The predominant processes at the onset of ionization are shown. (a) In the infrared regime, the atomic potential is bent by the strong light field to such an extent that the electron can tunnel through the barrier. (b) At ultraviolet to extreme ultraviolet photon energies, the atom can be ionized at lower intensities via single- or multiphoton absorption. (c) In the x-ray regime, the photon energy is sufficient to directly address inner-shell electrons. Already low power densities lead to ionization. The schematic is based on a visualization by C. Bostedt. Adapted from Ref. [130].

isolated [114]. Hence, the following description of ionization mechanisms concentrates on the *onset of ionization* in atoms.

In general, for a photoionization event to take place at least one photon needs to be absorbed by the atom. This of course depends on the atom's ionization potential E_{IP} and the photon energy E_{ph} of the incoming light field. Even if the photon energy is too small to overcome the ionization potential, the atom can get ionized by absorption of *multiple* photons [126] or *tunneling* of the electron through the potential barrier [127] given a sufficiently high field intensity. Which process prevails is strongly wavelength-dependent. In Fig. 2.14 the dominant processes at the onset of ionization for different photon energies are shown. In the infrared regime ($E_{ph} \sim 1\,\text{eV}$), as illustrated in Fig. 2.14 (a), the photon energy is far too small for single- or multiphoton ionization. At high intensities, however, the light field is strong enough to bend the atomic potential to such an extreme that *tunnel ionization* occurs where the electron can simply tunnel through the barrier. Therefore, the tunneling time has to match the period of the oscillating field, i.e., the frequency of the field has to be low enough to allow the electron to pass the barrier within a half-cycle of the light wave [115]. For even stronger fields, the barrier can be shifted below the ionization potential enabling *barrier suppression ionization* [115]. In the case of higher photon energies, as shown in Fig. 2.14 (b) for the ultraviolet to extreme ultraviolet regime ($E_{ph} \sim 10\,\text{eV}$), electrons from the valence shell can be promoted to the continuum by *multiphoton ionization* already at lower intensities, and a few photons are sufficient to further ionize the atom [128]. In the x-ray regime, as depicted in Fig. 2.14 (c), inner-shell electrons are addressed as the photon energy is sufficient for *direct ionization*. In the course of the process, additional decay channels can lead to a further ionization of the atom [129]. For example, in an *Auger decay* the inner-shell vacancy is filled by an electron from a higher-lying shell which is accompanied by the emission of another electron carrying the excess energy. The absorption of a single x-ray photon can therefore result in a multiply ionized atom. Thus, already in low intensity x-ray beams highly charged ions can be produced.

In order to classify the interaction of the light field with matter, a field dominated and a photon dominated regime can be identified depending on the ability of the light field to couple to the atomic potential. Therefore, it is helpful to consider the quiver motion

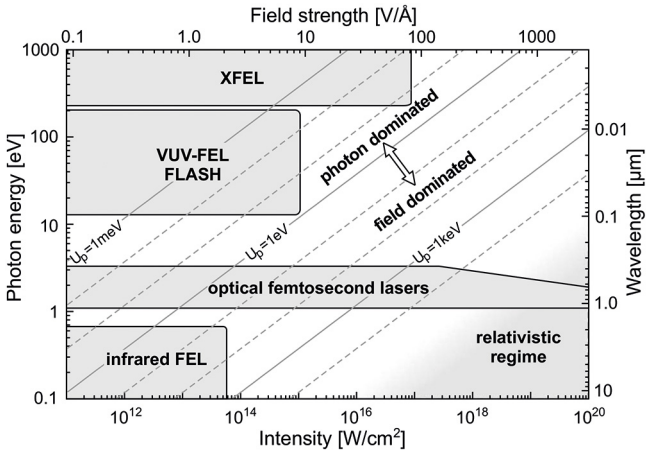

FIG. 2.15: Photon energy and intensity dependent coupling regimes. The shaded areas depict the conditions attainable at different light sources. Free-electron lasers in the vacuum ultraviolet regime (VUV-FEL) and x-ray regime (XFEL) clearly induce photon dominated ionization processes. Reprinted from Ref. [115].

of a free electron induced by the light field. The cycle-averaged kinetic energy of the oscillating electron is called the *ponderomotive potential* U_P, given by [115]

$$U_\mathrm{P} = \frac{e^2 \mathcal{E}_0^2}{4 m_\mathrm{e} \omega^2} \tag{2.41}$$

with e and m_e the electron charge and mass, respectively, ω the frequency of the light field and $\mathcal{E}_0$ its peak field strength. The ponderomotive potential can be calculated using the power density I and the wavelength λ of the light field in convenient units by the relation $U_\mathrm{P} = 9.33 \times 10^{-20}\,\mathrm{eV} \cdot I\,[\mathrm{W\,cm^{-2}}] \cdot (\lambda\,[\mathrm{nm}])^2$. The prevailing coupling mechanism is then given by a comparison of the electron's ponderomotive potential to the atom's ionization potential with a transition from field- to photon-dominated coupling at $U_\mathrm{P} = E_\mathrm{IP}$ [115]. This is illustrated in Fig. 2.15 as an intensity-frequency diagram for a typical ionization potential of a few electron volts. The shaded areas indicate the attainable intensities at photon energies from different light sources. It can be seen that ionization mechanisms in atoms exposed to infrared radiation are typically field dominated while in extreme ultraviolet or x-ray light fields, photon dominated ionization processes prevail. An estimate whether ionization proceeds predominantly via electron tunneling or (multi)photon absorption can be given using the *Keldysh parameter* γ [131],

$$\gamma = \omega \cdot \tau_\mathrm{t} = \sqrt{\frac{E_\mathrm{IP}}{2U_\mathrm{P}}}, \tag{2.42}$$

that compares the tunneling time $\tau_\mathrm{t} = \sqrt{2 m_\mathrm{e} E_\mathrm{IP}/(e\mathcal{E}_0)^2}$ to the frequency of the light field. Tunnel ionization prevails if the tunneling time is shorter than or comparable to the period of the light field (i.e., $\gamma \lesssim 1$), while for $\gamma \gg 1$, single- or multiphoton ionization is the dominant process [115].

In the course of the ionization process the cluster environment is not negligible anymore. For example, in studies at a short-wavelength FEL, irradiation with intense light pulses led to higher final charge states in clusters than in atoms [132, 133]. This pronounced absorption of energy by clusters was investigated in further theoretical work [116, 117, 134, 135] showing it is caused by an efficient coupling of the light field to the nanoplasma.

A more detailed description of the dynamics following the initial ionization process is given in the next section.

2.4.2 Nanoplasma Dynamics

The influence of the cluster environment on the ionization dynamics becomes increasingly important with each ionization step. In general, the interaction of intense radiation with clusters can be divided in three phases [114]. First, individual cluster atoms get ionized as described in the previous section. Second, the cluster turns into a nanoplasma as emitted electrons are not bound to individual atoms anymore but still attached to the cluster. Third, since the deposited energy cannot dissipate otherwise, the cluster disintegrates. In the following the basic concepts describing the nanoplasma dynamics in rare gas clusters are summarized based on the review article by Fennel *et al.* [115].

The ionization dynamics in a cluster are schematically shown in Fig. 2.16. The upper row illustrates a cluster hit by an intense short-wavelength light pulse while the lower row depicts the evolution of the cluster potential. Upon irradiation, the cluster gets ionized [cf. Fig. 2.16 (a)] which in turn leads to a deepening of the cluster potential and therefore a decreasing kinetic energy of the electrons leaving the cluster [cf. Fig. 2.16 (b)]. Due to the increasing charge of the cluster ions, the interatomic Coulombic barrier is suppressed leading to further ionization of the atoms. In order to describe the charging dynamics it is helpful to distinguish between *outer ionization* and *inner ionization* of the cluster [136]. The outer ionized electrons are those that can leave the cluster potential, while the inner ionized electrons are not longer bound to individual atoms but also not promoted to the continuum. However, they can move freely within the cluster potential and are therefore called *quasifree*. Hence, the nanoplasma is formed by the quasifree electrons that can no longer leave the cluster and the ionic cores of the cluster atoms [cf. Fig. 2.16 (c)]. Collisions of the trapped electrons lead to an equilibration of the energy throughout the cluster and additional evaporative electron emission [cf. Fig. 2.16 (d)]. Finally, the cluster expands leading to a shallower cluster potential [cf. Fig. 2.16 (e)]. The following discussion on cluster fragmentation mechanisms is based on the article by Arbeiter and Fennel [117]. The disintegration of the cluster can be described as a *Coulomb explosion* when many electrons are outer ionized and the resulting high charge is homogeneously distributed in the cluster. On the other hand, when many electrons remain trapped (i.e., inner ionized), the fragmentation process is characterized as *hydrodynamic expansion*. In this case, an efficient screening of the inner region by the dense nanoplasma enables recombination in the cluster center. This is also reflected by the *frustration parameter* comparing the total number of ionized electrons to the number of outer ionized electrons. It follows that with increasing photon energy the frustration parameter decreases and the predominant fragmentation mechanism changes from hydrodynamic to Coulombic.

The extremely efficient absorption of light by clusters is mainly due to the quasifree electrons. In particular, the light field couples to the nanoplasma which leads to a heating of the plasma electrons. Because of their increased kinetic energy the electrons can either promote other electrons to the continuum via electron impact ionization or directly leave the cluster potential. Further, hot electrons in the nanoplasma have been observed to suppress recombination processes so that the cluster remains highly charged [137]. In the following, *inverse bremsstrahlung* and *plasmon resonance absorption* are presented as relevant heating processes for cluster nanoplasmas that are also discussed in Ref. [115].

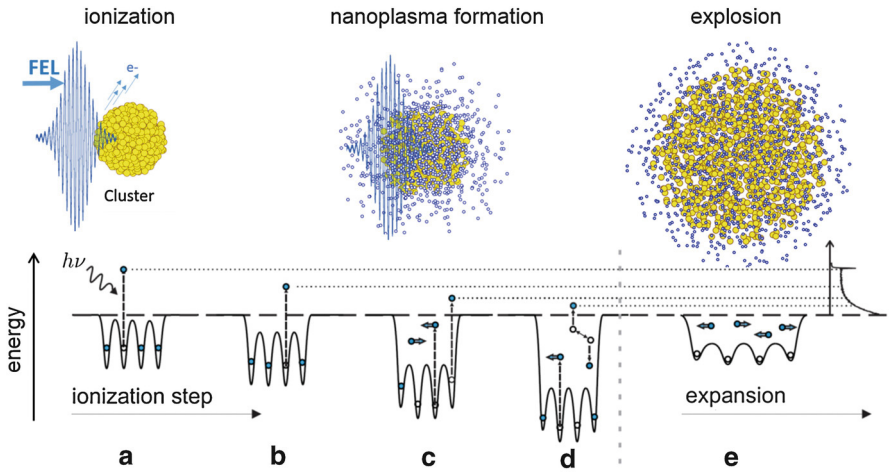

FIG. 2.16: The ionization dynamics of a cluster can be divided in three phases (top): (i) Ionization upon irradiation with the light field, (ii) formation of a nanoplasma, and (iii) explosion of the cluster. Bottom: Sketch of the cluster potential. (a) Initial ionization event. (b) The increasing charge of the cluster atoms leads to a deepening of the cluster potential and a decrease of the emitted electrons' kinetic energy. (c) The electron emission gets frustrated as the electrons cannot overcome the cluster potential. (d) A nanoplasma of quasifree electrons and ionic cores forms. Upon collision, trapped electrons can evaporate. (e) The potential gets shallower as the cluster expands accompanied by recombination and relaxation processes. The schematic is based on Refs. [114, 116, 117]. Reprinted from Ref. [119].

In general, a free electron in the plasma is accelerated by the incoming light field. The electron's quiver motion resulting from the light field's oscillation is reflected by the ponderomotive potential U_P as described above. Without interactions, the electron will not gain kinetic energy from the light field during the pulse. When the electron eventually scatters at an ion, however, it experiences a dephasing from the light field. Therefore, the electron can gain kinetic energy from the light field (especially at large scattering angles, e.g., backscattering at the ionic cores [138]), a process called inverse bremsstrahlung. Since the heating rate depends on U_P, this process is typically neglected in the x-ray regime but becomes important when using infrared light pulses. Further, an intense light field in the visible and infrared regime can drive a collective oscillation of the plasma electrons with respect to the ionic background of the cluster. A resonant energy transfer from the light field to the cluster can occur when the frequency of the light field ω matches the eigenfrequency of the oscillating electron cloud. The latter can be estimated by considering the cluster as a small metal sphere and employing Mie theory [139], which gives the frequency of the surface plasmon as

$$\omega_\mathrm{sp} = \sqrt{\frac{n_\mathrm{e} e^2}{3\epsilon_0 m_\mathrm{e}}} \tag{2.43}$$

with n_e the quasifree electron number density. The dynamics upon irradiation with a (near) infrared light pulse can be summarized as follows [114]: Starting with a neutral cluster, quasifree electrons are produced leading to a steep increase of n_e and a plasmon resonance higher than the frequency of the light field. However, when the cluster starts to expand, the electron number density decreases. Given a sufficiently long duration of the light pulse, the resonance condition $\omega = \omega_\mathrm{sp}$ is eventually fulfilled, enabling efficient heating of the nanoplasma.

In this thesis, the nanoplasma dynamics in helium nanodroplets after irradiation with an infrared light pulse are investigated. Because of the large ionization potential of helium, the power density of the infrared laser ($I_{\mathrm{NIR}} = 8 \times 10^{13}\,\mathrm{W\,cm^{-2}}$, cf. Sec. 3.2) is not sufficient to ionize the droplets [127]. Therefore, xenon atoms are embedded in the helium droplets that serve to enable tunneling ionization. Hence, the description of the nanoplasma dynamics needs to be extended to two components. As has been discussed in Sec. 2.1.3 the xenon atoms are expected to agglomerate to small clusters inside a helium droplet. In the simplest case, a single compact xenon cluster forms in the droplet. Upon irradiation with the infrared pulse a nanoplasma builds up in the xenon (sub)cluster. In consequence, the xenon dopants provide a lot of *seed electrons* that are driven by the light field through the helium environment initiating an avalanche-like ionization process [140], which in turn facilitates the ignition of a nanoplasma in the helium droplet [141]. While a pristine helium droplet would exhibit no ionization at all, complete inner ionization was reported in a theoretical study for droplets consisting of up to 1×10^5 helium atoms doped with a Xe_{13} cluster [142]. Further, theory suggests that energy absorption in the two-component nanoplasma is enhanced due to the two distinct plasmon resonances of the helium shell and the xenon core [24]. Accordingly, higher charge states have been observed for a xenon cluster embedded in a helium droplet than for a free xenon cluster of the same size that can be attributed to the resonant heating of the system effectively suppressing recombination [143]. As the helium shell expands much faster than the xenon core the resonance condition is first met for the shell and only at later times for the core, hence the final charge state also depends on the length of the light pulse [143]. The exact times for resonant excitation vary with both the helium droplet and dopant cluster size [144, 145], thus it remains unclear whether the droplets studied in this work experience resonant heating or not since the infrared pulse might already be over when its frequency is matched by the surface plasmon resonance of the helium environment. In addition, these rather detailed theoretical descriptions of two-component nanoplasmas might not match the conditions of the experiment reported here, where the xenon dopants typically constitute only 0.3 ‰ of the total number of atoms per droplet (cf. Sec. 4.1.3). Nevertheless, the xenon dopants enable the ignition of a nanoplasma in the helium droplets, thus inducing ionization dynamics in the droplets leading to their subsequent fragmentation.

2.4.3 Light Scattering on Small Particles

Light scattering techniques have become an important tool for structure determination of nanometer-sized gas phase particles. For example, cluster morphology has been an active field of research, with recent scattering experiments revealing xenon cluster growth by coagulation [11] and twin cluster structures [146] or an unexpected multitude of shapes for large silver clusters [13]. The novelty of these studies was to image the particle shapes in free flight, i.e., in the absence of a substrate that could influence their structure. In order to generate sufficient scattering signal, intense light sources are needed. The required intensity can be reached when using very short pulses (e.g., in the femtosecond range). Since the particle will suffer severe radiation damage during the interaction with the intense light pulse, the short pulse length is also important to take a snapshot of the particle before its disintegration, a principle known as *diffraction before destruction* [18, 147, 148]. Further, the wavelength of the light needs to be on the order of the particle size, i.e., typically in the XUV or x-ray regime. In contrast to

optical wavelengths, no lenses are available to sufficiently focus radiation in this regime to generate a real image as in common light microscopy. An alternative approach that is often used to circumvent this general problem is called *coherent diffraction imaging* (CDI), a lensless technique where the final image of the sample is retrieved from its diffraction pattern using algorithmic reconstruction methods. In simple words, the optical lens is replaced by a mathematical one.

In the following, the use of light scattering to determine the shapes of nanoparticles is presented with a focus on the techniques employed in this work. The description of the diffracted light field is based on the textbook by Hecht [149], assuming an electromagnetic plane wave incident on a two-dimensional, arbitrary aperture. The light field at the aperture is given by the aperture function

$$\mathcal{A}(x,y) = \mathcal{A}_0(x,y)\mathrm{e}^{i\phi(x,y)}, \tag{2.44}$$

where $\mathcal{A}_0(x,y)$ is the amplitude of the field across the aperture and $\exp\{i\phi(x,y)\}$ describes the variation of the phase from point-to-point. For a screen that is placed in the far-field limit, i.e., the distance from the object to the screen is much larger than the size of the object and the wavelength of the light, the Fraunhofer approximation holds and the field distribution at the screen is then given by

$$\tilde{\mathcal{E}}(k_x,k_y) = \iint \mathcal{A}(x,y)\,\mathrm{e}^{i(k_x x+k_y y)}\,\mathrm{d}x\,\mathrm{d}y. \tag{2.45}$$

From this equation it can be seen that in the two-dimensional case the diffracted light field $\tilde{\mathcal{E}}(k_x,k_y)$ is linked to the Fourier transform of the aperture function $\mathcal{A}(x,y)$:

$$\tilde{\mathcal{E}}(k_x,k_y) \propto \mathfrak{F}\{\mathcal{A}(x,y)\}, \tag{2.46}$$

hence, the diffraction pattern contains information on the aperture in reciprocal space. The aperture function is then given by the inverse Fourier transform of the diffraction pattern

$$\mathcal{A}(x,y) \propto \mathfrak{F}^{-1}\{\tilde{\mathcal{E}}(k_x,k_y)\}. \tag{2.47}$$

In the case of light incident on a non-absorbing phase object, the aperture function can be identified with the target's projected electron density. Therefore, from the diffraction pattern of a nanoparticle, its two-dimensional shape can be reconstructed. However, the scattered intensity measured at the screen I_{sc} is the modulus square of the scattered electrical field

$$I_{\mathrm{sc}} \propto \left|\tilde{\mathcal{E}}(k_x,k_y)\right|^2, \tag{2.48}$$

which means that the phase is lost during the measurement of the diffraction pattern. Hence, it is impossible to reconstruct the particle shape by a simple inverse Fourier transform. Instead, the phase has to be recovered using sophisticated algorithms, which is commonly done in two ways: Either by employing iterative phase retrieval algorithms based on oversampling [150] or by forward-fitting calculated diffraction patterns of model shapes to the recorded scattering images [13]. The choice which method to use is typically determined by the wavelength of the radiation used in the experiment, since it affects the maximum scattering angle θ_{max} that can be recorded. As will be shown in the following, it is helpful to distinguish between *small-angle scattering*, where phase retrieval algorithms can be applied, and *wide-angle scattering*, where forward-fitting methods have to be employed.

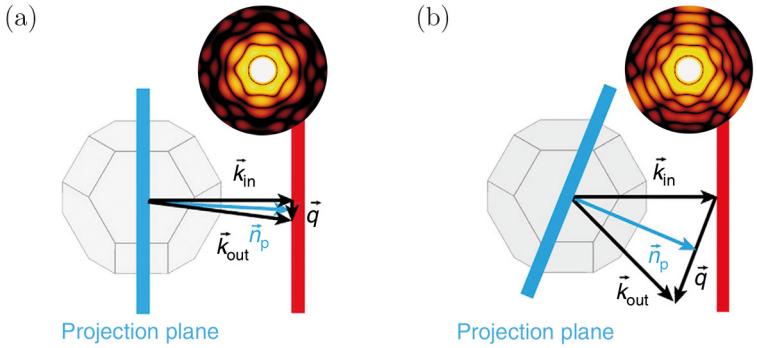

FIG. 2.17: Schematic of light scattering on small particles. The detector plane is shown in red with exemplary diffraction patterns shown in the insets. (a) For small-angle scattering, the normal on the projection plane $\boldsymbol{n}_\mathrm{p}$ is approximately parallel to the wave vector $\boldsymbol{k}_\mathrm{in}$, regardless of momentum transfer $\boldsymbol{q}$. Hence, the diffraction pattern is proportional to the Fourier transform of the projected particle density. (b) In the case of wide-angle scattering, $\boldsymbol{n}_\mathrm{p}$ varies with $\boldsymbol{q}$, therefore multiple projection planes add tomographic information on the particle shape and orientation to the diffraction pattern. Adapted from Ref. [13].

For an electromagnetic wave scattered at a particle, the momentum transfer $\boldsymbol{q}$ from the incoming wave to the outgoing wave with wave vectors $\boldsymbol{k}_\mathrm{in}$ and $\boldsymbol{k}_\mathrm{out}$, respectively, reads

$$\boldsymbol{q} = \boldsymbol{k}_\mathrm{out} - \boldsymbol{k}_\mathrm{in}. \tag{2.49}$$

According to Porod's law the scattered intensity rapidly decreases with q^{-4} [13]. Thus, depending on the dynamical range of the detector, the resolvable scattering signal is limited to a critical value for q that is in turn connected to the wavelength λ and the scattering angle θ via the relation

$$q = \frac{4\pi}{\lambda} \sin \frac{\theta}{2}. \tag{2.50}$$

For a fixed q it follows that at longer wavelengths larger scattering angles are experimentally accessible. Further, larger scattering angles give access to three-dimensional information on the particle shape. This is schematically shown in Fig. 2.17 for small and large $\boldsymbol{q}$. The projection plane of the particle is defined by the projection vector $\boldsymbol{n}_\mathrm{p} = \boldsymbol{k}_\mathrm{in} + \boldsymbol{q}/2$ and depicted in blue, while the detector plane is depicted in red. The diffraction pattern is shown in the inset. Fig. 2.17 (a) illustrates the small-angle scattering scenario: As the incoming wave is only slightly deflected in the scattering process, the momentum transfer is small ($q \ll k_\mathrm{in}$) and therefore the projection vector is approximately parallel to the wave vector of the incoming wave ($\boldsymbol{n}_\mathrm{p} \parallel \boldsymbol{k}_\mathrm{in}$). Hence, the resulting diffraction pattern is given by a Fourier transform of the particle density projected onto a single plane, which is also reflected by its point symmetry. In Fig. 2.17 (b) the wide-angle scattering scenario is shown. When the momentum transfer is large ($q \approx k_\mathrm{in}$) also the projection vector $\boldsymbol{n}_\mathrm{p}$ varies greatly, which leads to multiple projection planes contributing to the diffraction pattern. Therefore, tomographic information is encoded in a single scattering image and, in the case of a non-spherical particle, most likely point symmetry is lost.

In experiments using hard x-ray radiation, the detectable signal is usually limited to small scattering angles [depending on the brightness of the light source and the sensitivity of the detector, cf. Eq. (2.50)]. Further, absorption in the particle is typically negligible.

The projected particle shape can then be reconstructed from the diffraction pattern using phase retrieval algorithms [151] that are in general based on two-dimensional Fourier transforms, in principle with atomic resolution. On the other hand, in experiments utilizing XUV radiation, diffraction patterns can be recorded up to large scattering angles [cf. Eq. (2.50)]. While the choice of a longer wavelength is in general accompanied by a decrease of resolution it enables to collect three-dimensional information on the particle shape and orientation. In consequence, phase retrieval algorithms are not applicable and forward-fitting methods have to be used. Furthermore, absorption and refraction in the particle become important, especially close to atomic resonances. An analytic solution to the problem is given by Mie theory [139] for spherical particles taking into account their optical properties. It can be extended to other basic shapes, such as coated spheres, spheroids, and cylinders (see, e.g., Ref. [152]) but it is not suited to describe the scattering from arbitrary shapes. Alternatively, numerical methods can be used to simulate the scattering process. However, they typically come at a very high computational cost since multiple scattering events in forward and backward direction have to be included. Furthermore, each electron has to be considered as a point scatterer, thus with increasing particle size this quickly becomes a problem when used in an iterative shape retrieval approach. As an approximation that is less expensive in memory usage, dividing the model shape into consecutive slices, calculating the far-field diffraction pattern for each slice via a Fourier transform, and performing a phase correct summation of the individual Fourier transforms results in a wide-angle diffraction pattern containing three-dimensional information. This method has pioneered in electron scattering [153–155] and was successfully adapted to light scattering [13, 22]. In my thesis, wide-angle scattering images of rotating helium nanodroplets are presented and analyzed in a forward-fitting manner using the *multi slice Fourier transform* method to calculate the diffraction patterns (see also Sec. 4.2.2). The complete characterization of the droplet shapes enabled a comparison to theoretical shape models, underscoring the usefulness of this approach for structure determination on the nanometer scale.

Chapter 3

Experimental Setup

The aim of this thesis is to study the structure and the light induced fragmentation dynamics of individual nanoparticles using light scattering techniques. In order to take a snapshot of the structural configuration of the particle, the irradiation has to be shorter than the fragmentation dynamics, i.e., on the order of a few femtoseconds [18]. Further, to record a meaningful diffraction pattern of the sample, the wavelength of the incident light pulse has to be smaller than the size of the sample and in a single shot, a sufficiently large number of scattered photons has to be collected. Therefore, a source of intense coherent radiation with a high temporal and spatial resolution is needed.

As sources of intense, coherent, and monochromatic radiation, lasers play an important role in science, engineering and our everyday life. The word laser itself is an acronym for the underlying process of *light amplification by stimulated emission of radiation*. Stimulated emission occurs when a photon triggers the transition of an excited electron to a lower energy level. The energy of the incident photon has to match the energy difference of the two levels and because of the electron dropping to a lower state, a second photon with the same wavelength and phase as the first photon is emitted. A laser consists therefore of three parts: An active medium with at least three energy levels, an energy pump that generates a population inversion of these levels to have sufficient excited electrons available, and an optical resonator that amplifies the emitted radiation. The wavelength of the radiation depends on the energy difference of the levels and is therefore dictated by the material used as active medium. Conventional lasers emit radiation down to wavelengths of about 150 nm (e.g., excimer lasers). For shorter wavelengths, i.e., in the extreme ultraviolet (XUV, 124 nm to 10 nm) or x-ray (10 nm to 0.01 nm) regime, lifetimes of excited states become so short that it is increasingly difficult to accomplish a population inversion. In these wavelength regimes, the generation of laser-like radiation has to be achieved differently.

An alternative approach for the coherent emission of radiation has been laid out by John M. J. Madey in 1971 [156], where he described the stimulated emission of radiation from a relativistic electron moving in a periodic magnetic structure. This concept was also experimentally realized by Madey and coworkers [157, 158] and called a *free-electron laser* (FEL), with the first FEL emitting in the infrared regime. Since then, a tremendous progress has been made to extend the emission of FELs to higher photon energies. Because of the lack of highly reflective optics for short wavelengths (i.e., XUV and below), up to now, the active medium of the FEL (i.e., the periodic magnetic structure) could not be enclosed in an optical resonator. Instead, the magnetic structure

had to be prolonged to sufficiently amplify the emitted radiation in a single pass of the electrons, leading to several hundred meter long machines (in addition to the accelerator that is needed to provide relativistic electrons). The first XUV / soft x-ray FEL started user operation at Deutsches Elektronen-Synchrotron (DESY) in Hamburg in 2005 (Free-Electron Laser in Hamburg, FLASH) [159] and the first hard x-ray FEL came into operation at SLAC National Accelerator Laboratory in Stanford (Linac Coherent Light Source, LCLS) in 2009 [160]. With FERMI (acronym for Free-Electron Laser Radiation for Multidisciplinary Investigations) at the ELETTRA research center in Trieste the first seeded FEL – another step towards improved laser-like emission – started user operation in 2012 [161].

In the experiment described here, scattering images of helium nanodroplets were recorded using extreme ultraviolet (XUV) light pulses from the FERMI FEL. In the following Sec. 3.1 the basic principles of a seeded FEL are explained, the characteristics of FERMI are presented, and the optical laser system for pump-probe experiments is shown. In Sec. 3.2, the experimental setup, the detection of scattered XUV photons, and the helium nanodroplet source are discussed in detail.

3.1 The FERMI Free-Electron Laser

In this section, the fundamentals of FELs are explained with a special focus on the FERMI FEL. For a comprehensive description of the underlying physics, see e.g. the books by P. Schmüser, M. Dohlus, J. Rossbach, and C. Behrens [162] and E. Jaeschke, S. Khan, J. R. Schneider, and J. B. Hastings [163], on which the following considerations are based.

The generation of intense light pulses at FELs relies on the emission of radiation by an accelerated charge. When at rest or moving uniformly, electrostatic field lines originating from the charged particle regularly spread into space. A sudden acceleration of the particle will distort the field lines, as the information on the acceleration of the particle travels with the finite speed of light away from the particle. While to the one end, the field lines in vicinity of the particle are directed radially to the charge, to the other end, they still point to the location of the field lines where they would have been before the acceleration. This distortion of the field lines propagates with the speed of light and is known as electromagnetic radiation. For an electron on a circular trajectory it follows that it will constantly emit electromagnetic radiation, which has been called *synchrotron radiation* as it was first observed in a synchrotron [164]. In the beginning of cyclic particle accelerator research, this kind of radiation was regarded as an unwanted channel for losses of electron beam energy. However, its potential as source for intense radiation in the XUV and x-ray regime has later been seen and led to the development of synchrotron facilities dedicated to photon science. At an FEL, synchrotron radiation is generated by a high quality electron bunch traveling through a linear periodic magnetic structure. In this so-called *undulator*, alternating magnetic fields force relativistic electrons on a sinusoidal (or helical) trajectory causing the emission of linear (or circular) polarized light. First, this basic principle and the specifics of a seeded FEL will be discussed. For simplicity, the discussion will be restricted to planar (i.e., sinusoidal) movement of the electrons. Then, the characteristics of the FERMI FEL and the optical laser used in this experiment will be described.

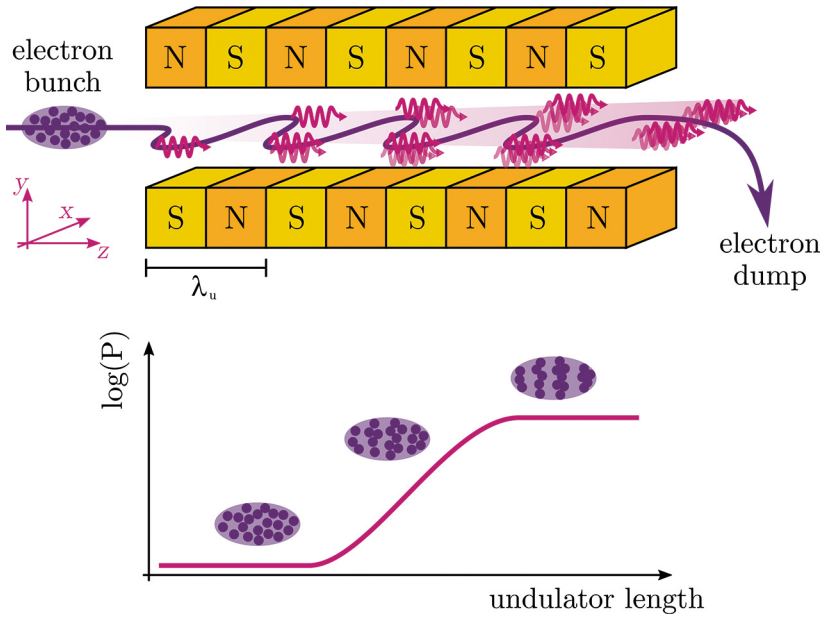

FIG. 3.1: Principle of a SASE free-electron laser. Top: An electron bunch enters an alternating magnetic structure with period λ_u that forces the electrons onto a sinusoidal orbit. This so-called *undulator* causes the electrons to emit radiation that interacts with the electron bunch. Bottom: Along the undulator length z, slices of higher electron density start to form inside the bunch, leading to coherent emission. The radiated power P grows exponentially until these microbunches have fully developed and then saturates. Adapted from Ref. [165].

3.1.1 Principle of a Seeded Free-Electron Laser

The fundamental mechanism for generating intense light pulses in a high gain FEL is illustrated in Fig. 3.1. A relativistic electron bunch enters the undulator, where a sinusoidal movement is imposed onto the electrons by the alternating magnetic structure with a period length λ_u. Along the electron beam axis (z-direction) the magnetic field is then oriented as $B_y(z) = B_0 \sin(2\pi z/\lambda_u)$ with B_0 being the magnetic field strength. The electron moves along this sinusoidal orbit with a velocity v close to the speed of light c_0. In the coordinate system of the moving electron, the period is reduced to $\lambda_u^* = \lambda_u/\gamma_0$ due to the relativistic length contraction with the Lorentz factor

$$\gamma_0 = \frac{1}{\sqrt{1-(v/c_0)^2}} = \frac{E_0}{m_0 c_0^2}, \tag{3.1}$$

where E_0 denotes the energy of the electron beam and m_0 is the electron rest mass. In the moving frame, the electron can be seen as a dipole oscillating with the corresponding frequency $\omega^* = 2\pi c_0/\lambda_u^*$. It therefore emits radiation that is strongly concentrated in forward direction because of the electron's relativistic energy. In the laboratory frame, for an observer looking along the beam axis onto the approaching electron, the emitted radiation is blue-shifted due to the relativistic Doppler shift to a wavelength $\lambda_0 \approx \lambda_u^*/(2\gamma_0) \approx \lambda_u/(2\gamma_0^2)$. While the undulator period is on the order of cm, high energy electrons of, e.g., 500 MeV emit radiation on the order of tens of nm.

An accurate treatment of a relativistic electron traversing an undulator can be found in Ref. [162]. It follows that the emitted radiation along the electron beam axis is centered

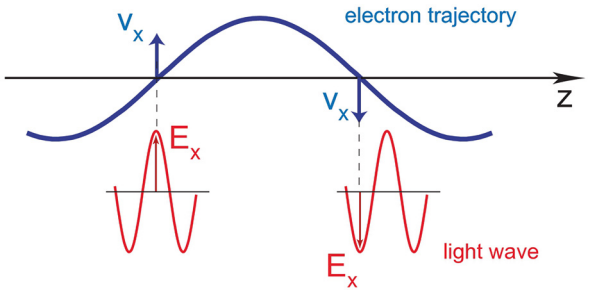

FIG. 3.2: Energy transfer from an electron to the light wave in an undulator. The x-component of the electron velocity v_x has to point in the same direction as the electric field E_x of the light wave. During half a cycle of the electron trajectory the light wave has to propagate by $\lambda_0/2$ to achieve a sustained energy transfer. Reprinted from Ref. [162].

around the wavelength

$$\lambda_0 = \frac{\lambda_\mathrm{u}}{2\gamma_0^2}\left(1 + \frac{K^2}{2}\right), \qquad \text{with} \quad K = \frac{eB_0\lambda_\mathrm{u}}{2\pi m_0 c_0}. \tag{3.2}$$

Here, K is the so-called *undulator parameter* with e the electron charge. The wavelength λ_0 of the photons emitted by a bunch of electrons traversing an undulator can thus be changed by altering the kinetic energy of the electrons, by varying the strength B_0 of the magnetic field (e.g., by changing the undulator gap), or, less conveniently, by changing the undulator period λ_u [166, 167]. Further, the energy has to be transferred from the electrons to the light wave. For an energy transfer, the x-components of the velocity of the electrons v_x and the electric field of the light wave E_x have to point in the same direction. While the light wave propagates in z-direction with speed c_0, the electrons have a smaller longitudinal velocity that will be further decreased as the electrons follow a sinusoidal orbit along the undulator. Therefore, a slip between the transverse velocity of the electrons v_x and the phase of the light wave will be introduced. A sustained energy transfer can only be achieved when the light wave propagates by $\lambda_0/2$ during half a cycle of the electron trajectory, see Fig. 3.2.

In forward direction, the electrons may emit at the fundamental wavelength λ or odd higher harmonics $\lambda_m = \lambda_0/m$ $(m = 1, 3, 5, \dots)$. However, this emission is in general incoherent, meaning that the electrons emit at random positions within the electron bunch. Therefore, the intensity I of the radiation emitted by an undulator scales linearly with the number of electrons N_e in the bunch, $I \propto N_\mathrm{e}$. Coherent emission would only be possible if the electrons emit as if they were a single particle, i.e., if they were concentrated in a bunch that is shorter than the light wavelength, which is technically not feasible for the large number of electrons needed per bunch. Nevertheless, since the wavelength λ_0 of the emitted photons is significantly shorter than the length of the electron bunch, the radiated field can interact with the electron bunch, given a good electron beam quality (low emittance, low energy spread, high charge) and a sufficient overlap between the electron bunch and the light field along the undulator length. In an FEL, these conditions are met. Then, depending on the position of an electron in the bunch with respect to the phase of the light field, the electron will gain or lose energy which leads to a change of the amplitude of its trajectory. This modulation of longitudinal speed will drive the electrons to form slices of higher electron density along the bunch, a process that is called *microbunching*. The formation of

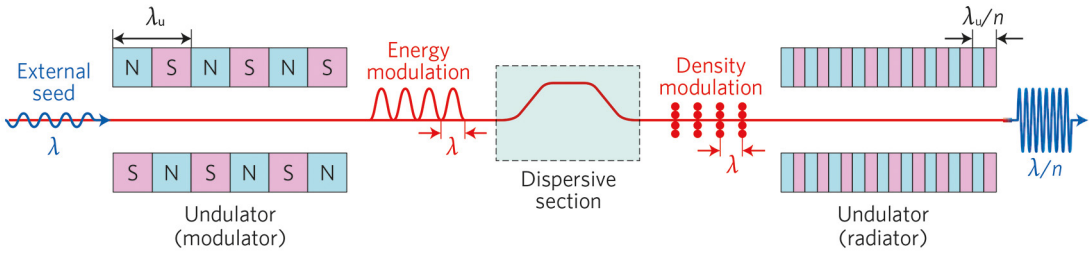

FIG. 3.3: Layout of the FERMI seeded free-electron laser. In the modulator the external seed laser with wavelength λ imprints an energy modulation onto the electron bunch with the same period length. A dispersive section changes the energy modulation into a density modulation. The pre-bunched electron cloud enters the radiator that is tuned to a higher harmonic order n of the seed laser, resulting in FEL emission with $\lambda_{\mathrm{FEL}} = \lambda/n$. Reprinted from Ref. [171].

these microbunches is schematically shown in the bottom panel of Fig. 3.1. Within the electron bunch, the positions of the microbunches are close to the positions for optimal energy transfer from the electrons to the light wave. As the electrons in a microbunch are concentrated in a region that is comparable to the wavelength of the light field, they radiate like a single, highly charged particle, and all electrons emit in phase. Therefore, the intensity of the light field emitted by an FEL scales as $I \propto N_{\mathrm{e}}^2$. The strong coherent radiation that is emitted adds to the process of microbunching even more, resulting in an exponential rise of radiated power P with increasing undulator length. When the microbunches are fully developed, the laser power saturates. This principle, that can be used to create short-wavelength intense light pulses, is called *self amplified spontaneous emission* (SASE). However, because of the stochastic nature of the emission, the resulting spectrum of the laser pulses has a spiky structure exhibiting shot-to-shot fluctuations around the central wavelength λ_0.

One possibility to get a clean spectrum with only one central wavelength present in each shot is to use a "seed" laser. The basic idea is to trigger the microbunching process by an external (seed) laser and therefore impose the spectral characteristics (wavelength stability, coherence) of the seed laser onto the FEL. At FERMI, the *high gain harmonic generation* (HGHG) scheme [168] for a seeded FEL is employed. It was mainly developed and first demonstrated [169] at the National Synchrotron Light Source of Brookhaven National Laboratory with FEL emission reaching the deep ultraviolet spectral region [170], and can roughly be divided in three steps: (i) Introducing a defined energy modulation to the electron bunch using a seed laser, (ii) transforming the energy modulation to a density modulation in the electron bunch, and (iii) causing the electron bunch to radiate at higher harmonics of the seed laser.

In Fig. 3.3 the general layout of FERMI is shown. Rather than starting from shot noise as in a SASE FEL, a seed laser with wavelength λ is introduced into an undulator that is tuned to be in resonance with the seed laser: By choosing appropriate values for the electron beam energy, the undulator period λ_{u}, and the undulator parameter K [cf. Eq. (3.2)], the undulator radiation becomes $\lambda_0 \approx \lambda$. In this case, the electric field of the seed laser will modulate the energy of the electrons in the bunch with a period of λ. This is why the first undulator at FERMI is called *modulator*. The energy modulated electron bunch then enters a magnetic chicane that acts as dispersive section converting the energy modulation into a density modulation with period λ. Finally, the pre-bunched electron cloud enters the last section of undulators, called *radiators*,

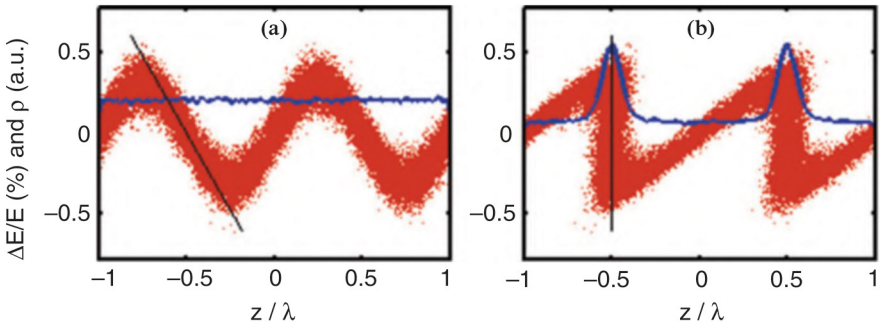

FIG. 3.4: Calculated distribution of electron energy $\Delta E/E$ and density ρ in the bunch along the undulator axis z in units of the seed laser wavelength λ, where $z/\lambda = 0$ is the center of the bunch. (a) The electron bunch after leaving the modulator. The electron energy is modulated by the seed laser wavelength λ while the density ρ stays constant. (b) The electron bunch after leaving the dispersive section. Because of different path lengths in the magnetic chicane, electrons with higher energies advance in the bunch while electrons with lower energies fall back, leading to a saw tooth-like distribution. This results in slices of higher electron density with a distance of λ (microbunches). Reprinted from Ref. [174].

that are tuned to a higher harmonic of the order n, i.e., with an undulator period λ_u/n. The electron then quickly exhibits microbunching leading to a high gain of coherent emission at a wavelength λ/n. A calculated energy distribution of the electron bunch before and after the dispersive section is shown in Fig. 3.4. The horizontal axis is the relative longitudinal position in the bunch z in units of the seed laser wavelength λ (with the center of the bunch at $z = 0$). The electron energy offset $\Delta E/E$ is shown in red and the electron density ρ in blue. In Fig. 3.4 (a), the electron distribution is shown before entering the magnetic chicane. The energy of the electrons in the bunch is modulated by the seed laser with period λ while the electron density ρ remains constant. The deviation of the electrons in the chicane depends on their energy, therefore their path lengths differ. High energy electrons travel a shorter path and move forward in the bunch, low energy electrons fall back. This leads to a sawtooth-like energy distribution and therefore to a density modulation of the electron bunch with slices in intervals of λ, which can be seen in Fig. 3.4 (b). The HGHG process will only be initiated if the amplitude of the energy modulation is sufficiently high as compared to the influence of the SASE process. On the other hand, a larger dispersion of the electrons in the bunch leads to less defined microbunches. As is exemplified by the electron density profile in Fig. 3.4 (b) the HGHG process relies on microbunches with periodicity λ whose spatial extent has to be much shorter than λ to amplify higher harmonics. It follows that a smearing out of the beam energy leads to a steep decrease of radiated power with increasing harmonic number. Therefore, in order to generate soft and hard x-ray FEL radiation using an external seed laser, more sophisticated approaches have to be considered, such as a cascaded (i.e., double stage) HGHG scheme [172] or *echo-enabled harmonic generation* (EEHG) [173].

3.1.2 Characteristics of the FERMI Free-Electron Laser

Seeding an FEL leads to enhanced laser-like emission of radiation. The ∼350 m long FERMI FEL at the ELETTRA synchrotron in Trieste, Italy, was the first user facility providing XUV FEL radiation based on the HGHG scheme. It comprises two FEL lines:

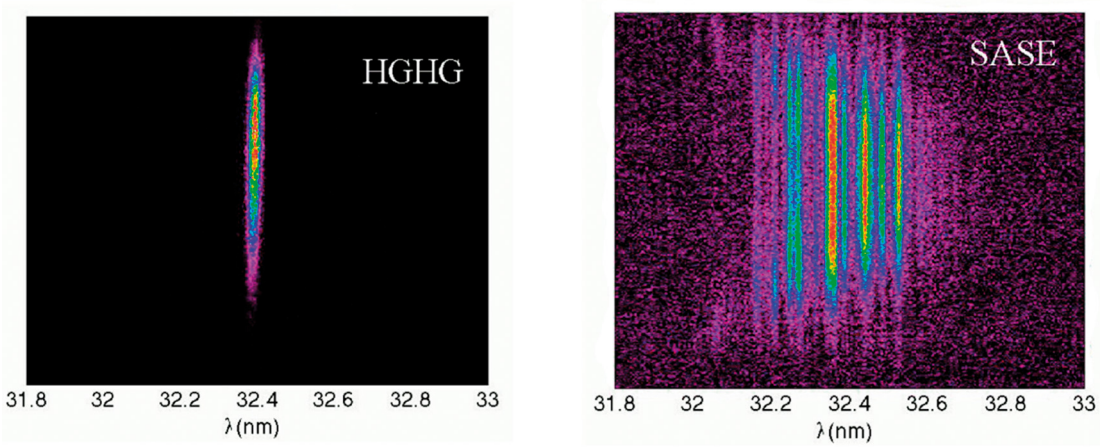

FIG. 3.5: Single-shot spectra of HGHG and SASE processes. (a) FERMI operated in HGHG mode exhibiting a single emission line at the central wavelength $\lambda_{\mathrm{FEL}} = 32.4\,\mathrm{nm}$. (b) FERMI operated in SASE mode at the same wavelength. A typical spiky structure can be observed in the spectrum. Reprinted from Ref. [176].

FEL-1 in the HGHG configuration [161] covers the wavelength regime from 100 nm to 20 nm and FEL-2, that uses FEL-1 as seed in a two-stage HGHG cascade [175], covers wavelengths from 20 nm to 4 nm. A recent overview on the facility, its performance and future prospects is given in Ref. [176]. The following description of FERMI's characteristics will be restricted to FEL-1 as only the first FEL line was used in this experiment. The undulator system of FERMI FEL-1 consists of one modulator and six radiator modules. The modulator is 3 m long and has a period of $\lambda_{\mathrm{u}} = 100\,\mathrm{mm}$ with a variable gap that can be closed down to 10 mm [177] to match the resonance condition $\lambda_0 \approx \lambda$ of the undulator and the seed laser [cf. Eq. (3.2)]. The radiators are each 2.4 m long with a period of $\lambda_{\mathrm{u}} = 55\,\mathrm{mm}$ and also a variable gap. A special APPLE-II undulator configuration gives full control on the electron trajectory (horizontal or vertical sinusoidal or helical) in the magnetic structure [178, 179] and thus the polarization of the emitted FEL radiation [180]. The FERMI FEL can be operated in SASE mode as well as in HGHG mode. In Fig. 3.5, a comparison of typical spectra of single FEL pulses ($\lambda_{\mathrm{FEL}} = 32.4\,\mathrm{nm}$) measured at FERMI [176] are shown. One can clearly see the monochromatic emission in HGHG mode [Fig. 3.5 (a)] with a well defined line at the radiator resonance while Fig. 3.5 (b) shows a spiky spectrum typical for the SASE process. The interplay of the seed laser with the electron bunch causes a transfer of the seed laser's emission properties (pulse length, coherence, central wavelength, bandwidth, intensity) to the FEL radiation. In Fig. 3.6 the pulse stability of FERMI in seeded mode is shown for a single shot [Fig. 3.6 (a)] and 500 consecutive shots [Fig. 3.6 (b)]. For the single shot, the photon energy offset for the seed laser emission line ($\lambda = 260\,\mathrm{nm}$, solid blue line) is compared with the FEL radiation spectrum of the eighth harmonic ($\lambda_{\mathrm{FEL}} = 32.5\,\mathrm{nm}$, dashed red line), yielding an FEL bandwidth of 20 meV (r.m.s.) [161]. From the multi-shot spectra it can be seen that the central photon energy is very stable (black line) and the FEL intensity (red line) shows little fluctuations. Therefore, in terms of spectral quality, emission stability and control of photon parameters, FERMI surpasses all SASE FELs, however, being limited to the XUV / soft x-ray regime.

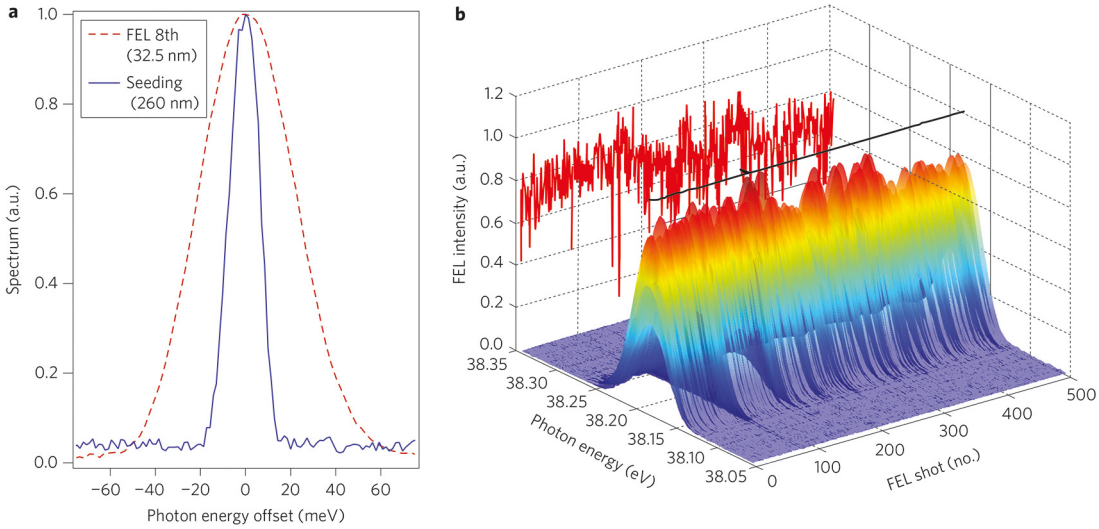

FIG. 3.6: Spectral stability of FERMI in seeded (HGHG) mode. (a) Single-shot spectra (photon energy offset from central wavelength) for the seed laser ($\lambda = 260\,\mathrm{nm}$, solid blue line) and the FEL at the eighth harmonic ($\lambda_{\mathrm{FEL}} = 32.5\,\mathrm{nm}$, dashed red line). The FEL bandwidth is 20 meV (r.m.s.). (b) Multi-shot spectra for 500 consecutive shots exhibiting a very stable position of the emission peak (solid black line). Reprinted from Ref. [161].

3.1.3 The Optical Laser System

A precise synchronization of the seed laser with the electron bunch is needed to accomplish emission of seeded FEL radiation. The repetition rate of FERMI's optical laser system is locked to the same master oscillator that also initiates the generation and acceleration of the electron bunch. The position of the seed laser pulse relative to the electron bunch has to be controlled with femtosecond resolution [181]. Therefore, a particular effort was made to generate and distribute a highly stable timing signal to all subsystems, as the main source for timing instability of the seed laser is its synchronization to the reference signal provided by the FEL timing distribution. In Fig. 3.7 the optical layout of the seed laser is shown. The timing reference signal ("OptRef") is fed to the balanced optical cross correlator (BOCC) that in combination with a timing unit (TMU) especially developed at FERMI locks the titanium-sapphire (Ti:S) oscillator to the FEL timing. The femtosecond Ti:S oscillator output is sent to a chirped pulse amplifier delivering 100 fs near infrared pulses with an energy of up to 7 mJ [182]. The amplified beam is then split into two arms, one for the seed laser and one for the user laser. For the seed laser, about 70 % of the amplified beam's energy is used to pump an optical parametric amplifier (OPA). Frequency mixing of the OPA's signal beam with the pump beam and subsequent frequency doubling generates the ultraviolet seed laser beam [182]. As the signal- and idler-wavelengths of the OPA can be varied from 1.08 µm to 2.6 µm [177], this scheme enables seed laser pulses with a wavelength of 230 nm to 261 nm. Depending on the specific setup, the pulse duration of the seed laser is typically in the range from 100 fs to 200 fs with a pulse energy of up to 0.1 mJ. Alternatively, one can also use the third harmonic (THG) of the Ti:S amplifier to seed the FEL at a fixed wavelength. This results in a higher pulse energy enabling FEL emission at higher harmonic orders. The remaining 30 % of the beam are sent to the experimental stations via the other arm to be used as user laser with a

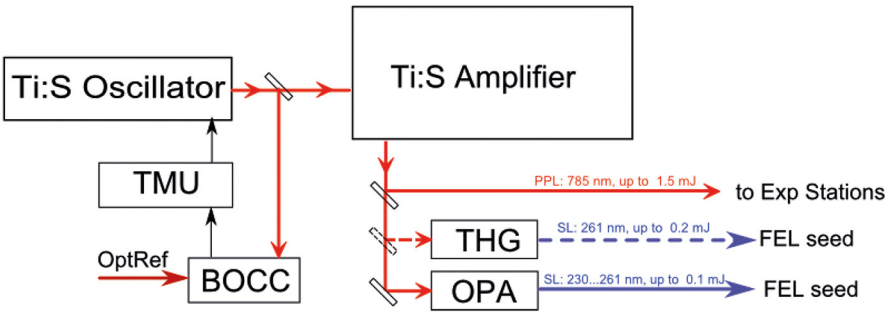

FIG. 3.7: Optical layout of the seed laser. The titanium-sapphire (Ti:S) oscillator is locked to the reference timing signal ("OptRef") by a balanced optical cross correlator (BOCC) and a dedicated timing unit (TMU). After passing the Ti:S amplifier the beam is split to a seed laser and a user laser arm. The seed laser pulse is generated using an optical parametric amplifier (OPA) and subsequent frequency doubling resulting in wavelengths ranging from 230 nm to 261 nm or alternatively by using the third harmonic (THG) of the Ti:S pulse. In the other arm, near infrared pulses ($\lambda_{\mathrm{NIR}} = 785\,\mathrm{nm}$) with up to 1.5 mJ pulse energy are transported to the experimental stations for user pump-probe experiments. Reprinted from Ref. [182].

fundamental wavelength of $\lambda_{\mathrm{NIR}} = 785\,\mathrm{nm}$ and pulse energies up to 1.5 mJ. This part of the beam can be used for pump-probe experiments. As both the seed and the user laser originate from the same laser system, the relative temporal jitter can be kept very low. Further, the emission of the FEL pulse is closely linked to the seed pulse in time, i.e., with a precision of below 1 fs [182]. For pump-probe experiments at FERMI, the relative timing jitter between the user laser and the FEL pulse is typically below 10 fs, with a temporal jitter as low as 2 fs reported [183].

3.2 Helium Droplet Diffraction Experiment

The experiment was performed at FERMI's Low Density Matter (LDM) end-station that is dedicated to atomic, molecular, and cluster physics research. The LDM end-station provides several sources for relevant gas-phase targets as well as a range of detectors for ion- and electron spectroscopy (e.g., a velocity map imaging spectrometer and a magnetic bottle), mass spectroscopy (e.g., an ion time of flight spectrometer), and the detection of scattered light [184]. With the possibility to operate multiple detectors at the same time, it is a versatile instrument to collect comprehensive data sets.

In the following section the experimental layout will be presented while in Sec. 3.2.2 the scattering detector and in Sec. 3.2.3 the helium nanodroplet source will be discussed.

3.2.1 Setup at the Low Density Matter Instrument

The design of the LDM instrument enables to record electron and ion spectra as well as scattered photons simultaneously. However, as this thesis focuses on the analysis of the scattering images, the ion and electron spectrometer are not separately introduced in the following description of the experiment. A detailed presentation of the LDM end-station and its detectors can be found in Ref. [184].

A schematic of the experimental setup is shown in Fig. 3.8. The general layout of the

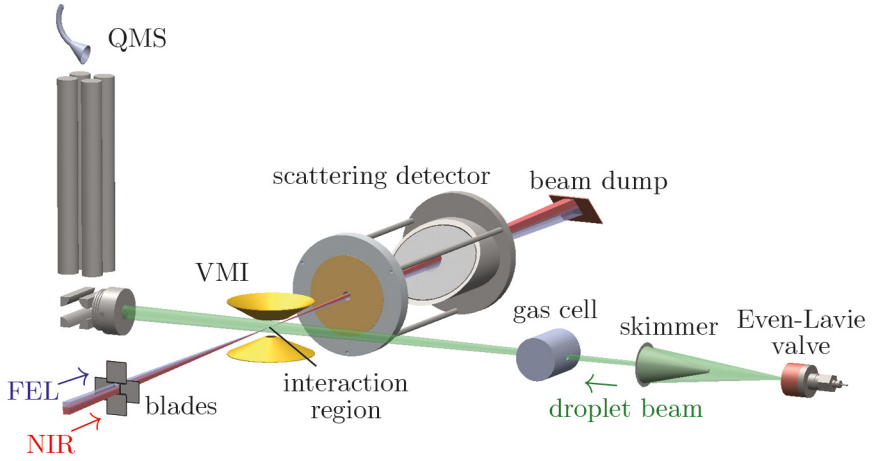

FIG. 3.8: Experimental layout of the LDM end-station. The droplet beam is produced by an Even-Lavie valve. It traverses a skimmer and a gas cell before reaching the interaction region where it gets intersected by the FEL and the NIR laser beam. A system of blades is used to reduce straylight from the beamline. Along the optical axis the scattering detector is placed to record the scattered light from the droplets. Atop the interaction region, a VMI is placed. A QMS is used for alignment of the droplet beam. Adapted from Ref. [184].

experiment is a pump-probe setup, where the helium droplets are excited using a near infrared (NIR) pump pulse and subsequently imaged using an XUV probe pulse. The helium droplet beam is produced by a pulsed source equipped with an Even-Lavie [185] valve (cf. Sec. 3.2.3). The droplet beam traverses a skimmer that extracts the central region of the beam and a gas cell that can be used for doping of the helium droplets. A quadrupole mass spectrometer (QMS) is used for alignment and diagnostic of the cluster beam. The NIR laser beam is coupled into the experimental chamber quasi collinearly with respect to the FEL beam. A system of four blades is placed around the beams for straylight reduction. In the interaction region, the droplet beam is intersected by the NIR laser beam and the XUV FEL beam. Atop the interaction region, a velocity map imaging (VMI) spectrometer [186] is mounted. When a helium nanodroplet is hit with an intense XUV pulse from the FEL, the scattered light will be collected by a scattering detector that is described in Sec. 3.2.2. The scattering detector assembly has central holes to let the NIR laser and FEL beams pass until they finally reach the beam dump.

In Fig. 3.9 a sketch of the LDM instrument along the droplet beam is shown. It consists of several differentially pumped vacuum chambers that are all equipped with turbomolecular pumps. The helium droplet source is attached to the expansion chamber that has a high pumping speed (two $2300\,\mathrm{L\,s^{-1}}$ turbomolecular pumps) for high gas loads. The pressure in the expansion chamber with the valve in operation is typically $p_{\mathrm{exp}} = 1 \times 10^{-5}\,\mathrm{mbar}$. In order to obtain a well defined droplet beam with low atomic fraction, a skimmer with an opening of $\varnothing 4\,\mathrm{mm}$ is placed 215 mm away from the nozzle. In the doping chamber, a cylindrical gas cell is installed perpendicular to the cluster beam with an inner diameter of $L = 35.3\,\mathrm{mm}$ that can be filled with a dopant gas. The base pressure in the doping chamber (i.e., with an empty gas cell and the valve in operation) is $p_{\mathrm{dop}} = 3 \times 10^{-7}\,\mathrm{mbar}$. In the detector chamber, the VMI spectrometer and the scattering detector are installed. With the valve running, the pressure in the detector chamber is $p_{\mathrm{det}} = 3 \times 10^{-9}\,\mathrm{mbar}$. In the QMS chamber, an Extrel MAX-1000 quadrupole mass spectrometer is installed. The pressure with the valve in operation is

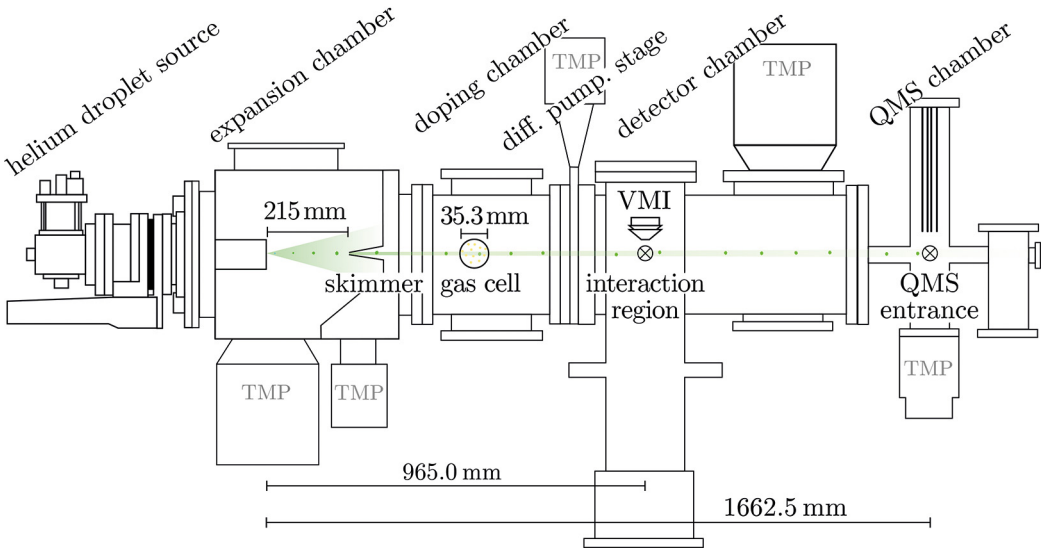

FIG. 3.9: Sketch of the LDM instrument. The helium droplet source is attached to the expansion vacuum chamber where the droplet beam is produced. The central region of the beam gets extracted by a ∅4 mm skimmer before it covers a 35.3 mm distance in a gas cell. The interaction region is located in the detector chamber 965 mm away from the nozzle. Signal from ionic fragments is collected by a VMI spectrometer placed atop the interaction region. A QMS is used to align the droplet beam and to measure the droplet velocity $v_D \approx 320\,\mathrm{m\,s^{-1}}$ by analyzing the flight time of the helium dimer signal.

$p_{QMS} \leqslant 1\times10^{-9}$ mbar. The alignment of the source is done by observing and maximizing the helium dimer signal at the QMS. The maximum intensity of the helium dimer (i.e., the droplet signal) is at a measured flight time of 5.18 ms. With the distance from the nozzle to the QMS entrance of 1662.5 mm the droplet velocity is $v_D \approx 320\,\mathrm{m\,s^{-1}}$. The interaction region is at a distance of 965 mm from the nozzle, therefore the droplets should arrive after a flight time of 3.0 ms.

In general, the FEL was tuned to wavelengths ranging from $\lambda_{FEL} = 32$ nm to 65 nm delivering pulse lengths below 100 fs and focal intensities exceeding $3\times10^{14}\,\mathrm{W\,cm^{-2}}$, as will be discussed in the following. The main FEL parameters are summarized in Tab. 3.1. The FEL beam was focused to the interaction region using two bendable mirrors in a Kirkpatrick-Baez setup [187]. The focal spot size σ_{FEL} (FWHM) depends on the FEL wavelength and was measured using a Hartmann type wavefront sensor [188, 189] for three wavelengths: (i) $\sigma_{FEL} = 5\times6\,\mu m^2$ at $\lambda_{FEL} = 32$ nm, (ii) $\sigma_{FEL} = 8\times12\,\mu m^2$ at $\lambda_{FEL} = 57.7$ nm, and (iii) $\sigma_{FEL} = 9\times13\,\mu m^2$ at $\lambda_{FEL} = 64$ nm. The FEL pulse energy, denoted by I_0 following FERMI's convention, was measured on a shot-to-shot basis with a dedicated intensity monitor that relies on the ionization of nitrogen by the FEL radiation in a vacuum chamber at a low particle density (pressure $\sim3\times10^{-5}$ mbar) [190, 191]. During the experiment, the measured values were calibrated using a calibration table from 2012. However, later measurements that were done in 2016 showed that this calibration table underestimates the pulse energy [191]. The FEL pulse length τ_{FEL} depends on the seed laser that has an estimated pulse length $\tau_{seed} = 120$ fs [192]. It scales with the harmonic order n as [183]

$$\tau_{FEL} = \begin{cases} \tau_{seed}\cdot n^{-1/2} & \text{(normal FEL regime)} \\ \tau_{seed}\cdot \frac{7}{6}n^{-1/3} & \text{(saturated FEL regime),} \end{cases} \tag{3.3}$$

TABLE 3.1: FEL parameters. The seed laser wavelength λ, harmonic order n, FEL wavelength λ_{FEL} and pulse length τ_{FEL}, overall beamline transmission T_{BL}, mean pulse energy $\langle I_0 \rangle$, and FEL focus intensity I_{FEL} are given. See text for details on the calculation of τ_{FEL} and I_{FEL}.

λ (nm)	n	λ_{FEL} (nm)	T_{BL}[a] (%)	$\langle I_0 \rangle$ (µJ)	I_{FEL} (W cm^{-2})
257.7	8	32.2	51	50	7.9×10^{14}
261.5	5	52.3	32	220	8.0×10^{14}
230.4	4	57.6[b]	29	100	3.4×10^{14}
236.1	4	59.0	28	300	8.0×10^{14}
241.6	4	60.4	27	330	8.7×10^{14}
255.2	4	63.8[b]	23	300	6.6×10^{14}
260.0	4	65.0	23	300	6.5×10^{14}

[a] Values from Ref. [188]
[b] These values are for the *static* data (cf. Sec. 4.2). For the *dynamic* data (cf. Sec. 4.3), slightly different values were used.

yielding an FEL pulse length as long as 90 fs in the case of saturated FEL operation. The polarization of the FEL was set to right circular as this yields a higher output power because of a better coupling between the electron bunch and the light wave [162]. With the wavelength-dependent beamline transmission T_{BL}, the mean pulse energy $\langle I_0 \rangle$, the upper estimate for the FEL pulse length $\tau_{\mathrm{FEL}} = 90$ fs, and the focal spot size σ_{FEL}, a lower limit for the FEL focus intensity I_{FEL} can be given as:

$$I_{\mathrm{FEL}} = \frac{\langle I_0 \rangle \cdot T_{\mathrm{BL}}}{\tau_{\mathrm{FEL}} \cdot \sigma_{\mathrm{FEL}}} \tag{3.4}$$

The calculated values for the FEL focus intensity are shown in Tab. 3.1. It should be noted that the values for T_{BL} refer to horizontal polarization [188]. As the transmission for horizontal polarization is lower than for vertical polarization, this should give a lower limit for the transmission of the right circular polarized light used in this experiment. Further, the effective transmission of the beamline and therefore the focus intensity can be lower depending on how much the blades were closed to minimize straylight. The divergence (r.m.s., in µrad) of FERMI FEL-1 scales with the wavelength as $1.25\,\lambda_{\mathrm{FEL}}$ (in nm) [188]. Given the beamline geometry described in Ref. [188] and a typical opening of the blades of 11×11 mm^2, it is assumed the blades reduce the overall transmission by up to a few tens of percent [193].

The NIR laser delivers 90 fs pulses with a mean pulse energy of 577 µJ that are focused to a 100 µm ($1/e^2$ diameter) spot in the interaction region. This results in a power density of $I_{\mathrm{NIR}} = 8 \times 10^{13}$ W cm^{-2}. Please note that the NIR focus has been left intentionally larger than the FEL focus to ensure that each droplet that is hit by the FEL beam was also hit by the NIR beam before. Further, a good spatial and temporal overlap of the two beams has to be established. The delay Δt between the XUV and the NIR pulses can be varied using a delay stage in the NIR laser beam path with a maximum delay range of 1140 ps and a minimum step size of 1.6 fs [194]. By definition, both beams overlap at $\Delta t = t_0$, which will be referred to as *time zero*. In the following, the procedures used in this experiment to overlap both beams are described. A first coarse alignment is performed by overlapping both beams on a phosphor screen that can be

inserted in the interaction region. Then, a coarse temporal overlap can be achieved by inserting a high-bandwidth coaxial copper cable [194] to the interaction region: the incident XUV and NIR photons induce a current in the cable's inner conductor resulting in two current pulses that can be monitored. Both pulses are then overlapped by varying the delay of the NIR laser which results in a value for time zero with a precision of about 20 ps [195]. Given a coarse spatial and temporal overlap, a higher accuracy can be achieved by resonant two-photon ionization of helium gas: Therefore, the FEL is tuned to a long-lived resonance of atomic helium (e.g., $1s5p$ at $\lambda_{\mathrm{FEL}} = 51.6\,\mathrm{nm}$ [196]) to excite atoms, while the subsequent NIR pulse ionizes the already excited atoms. The delay of the NIR pulse is initially set to the XUV pulse coming first and the NIR pulse arriving a few tens of picoseconds later for optimization of the spatial overlap. Then, the delay of the two pulses is scanned, i.e., their separation in time is decreased. As soon as the XUV pulse starts to arrive after the NIR pulse, the signal will suddenly decrease, as neither the XUV nor the NIR pulse alone are able to ionize the atoms. This results in a Gauss error function from which time zero can be derived with sub-picosecond precision. This method needs only very little energy per pulse in either color. On the other hand, the intensities of the FEL and the NIR pulses have to be monitored, as saturation of one of the processes leads to a shift of t_0 in time. Also, the FEL has to be tuned to a resonance which can be a time consuming procedure. Finally, with a good spatiotemporal overlap already established, a fine-tuning of the temporal overlap can be performed by observing *sidebands* in the photoelectron spectrum of helium gas [197]. There, an XUV photon promotes an electron to the continuum, where it can gain or lose energy by absorption or stimulated emission of one or several NIR photons. While the absorption of an XUV photon leads to a photoemission line at an energy E_{XUV}, the interaction with the NIR pulse transfers intensity to the sidebands at energies $E_{\mathrm{XUV}} \pm m_{\mathrm{sb}} \cdot E_{\mathrm{NIR}}$, where E_{NIR} is the NIR photon energy, and m_{sb} is the order of the sideband ($m_{\mathrm{sb}} = 1, 2, 3, \dots$) [183]. This is a true cross-correlation method as the signal is zero when there is no spatiotemporal overlap. Further, the signal is not easily saturated: for higher NIR intensities, more sidebands (i.e., higher orders) will appear that presumably do not exhibit saturation.

While the procedures for a coarse overlap were performed once at the beginning of the experiment, the resonant two photon ionization method and the sideband method were performed to optimize the spatial and temporal overlap for each seed laser wavelength.

3.2.2 Detection of Scattered XUV Photons

The scattering detector consists of a microchannel plate (MCP) that is stacked onto a phosphor screen, similar to the one described in Ref. [116]. A schematic of the scattering detector setup is shown in Fig. 3.10. The scattered XUV photons $h\nu$ create electrons in the MCP that get amplified and lead to visible fluorescence on the phosphor screen. A camera system that is equipped with an Andor Neo sCMOS camera [198] with a resolution of $2560\,\mathrm{px} \times 2160\,\mathrm{px}$ then takes a picture of the phosphor screen via a 45° mirror. All elements along the FEL- and NIR-beam axis have central holes (MCP and phosphor screen: ∅3 mm, mirror: ∅10 mm) to let the beams pass. The MCP is a spatially resolving detector made of a multitude of channels with a diameter of 25 µm, that each act as an electron multiplier. For amplification, a voltage of 1.3 kV to 1.5 kV is applied between the front and the back of the MCP. An incident photon hitting a channel wall produces a secondary electron that gets accelerated and initiates an

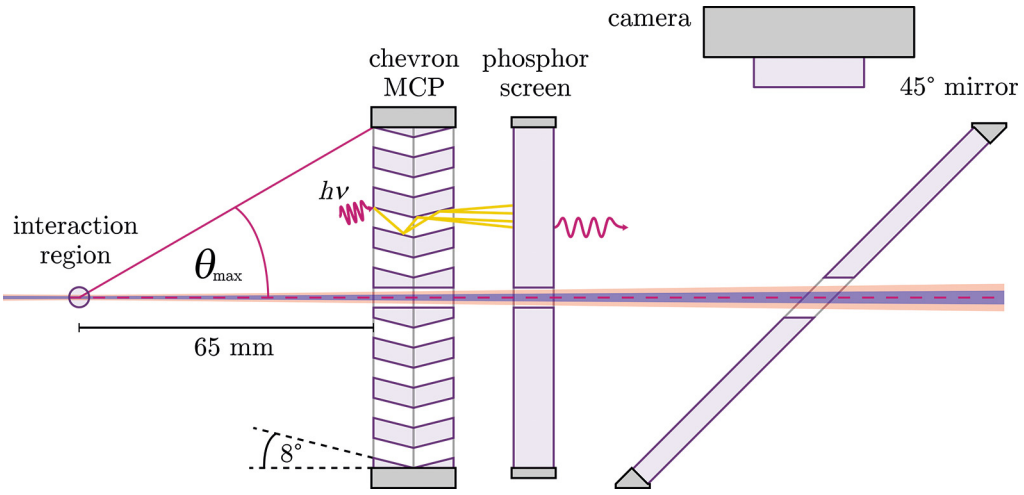

FIG. 3.10: Schematic of the scattering detector. It consists of a chevron type MCP (bias angle 8°) that is stacked onto a phosphor screen and is placed 65 mm away from the interaction region. With a diameter of 75 mm, it can record scattered photons $h\nu$ up to a maximum angle $\theta_{\max} \approx 30°$. The incident photons cause an electron cascade amplifying the signal that gets converted to visible photons by the phosphor screen. A picture of the screen is taken by a sCMOS camera via a 45° mirror.

electron cascade by subsequent collisions with the channel wall. To increase the collision probability of the incident photon with the channel wall, the channels are tilted by 8° (the so-called *bias angle*). Also, a second MCP plate that is rotated by 180° is attached to the first MCP for a further increase of the collision probability during the acceleration phase of the electrons, and to prevent unwanted signal from ions that are generated at high amplification at the back of the MCP and travel back to the front of the MCP. This arrangement is referred to as *chevron MCP* because of its channels' chevron-like look (cf. Fig. 3.10). The front of the MCP is coated with gold and a 300 nm layer of magnesium fluoride to decrease the total MCP resistance and enhance the conversion efficiency for XUV photons, respectively. After exiting the channel, the electron cloud is accelerated towards a phosphor screen, where it generates a visible image of the electron charge distribution along the MCP. The P43-type phosphor screen emits at a peak wavelength of 545 nm. In general, the intensity of the fluorescence depends on the number of incident XUV photons. However, the whole amplification process is nonlinear. This is especially important for diffraction patterns, where most intensity gets scattered to the central region of the image. While a large scattering signal in the center leads to saturation of the detector, considerably weaker intensity at larger scattering angles can still be detected.

The bias angle of the MCP channels increases the collision efficiency. At the same time, it leads to an angular dependent response of the detector when recording signal from a point source [199]. In Fig. 3.11 the calculated relative response to a point source of an MCP detector with channels tilted by 8° [200] is shown. It has been taken into account that the probability to generate a secondary electron depends on the angle of incidence (because of the penetration depth into the channel wall) as well as the wavelength of the photon (because of total reflection). Further, the quantum efficiency also depends on the scattering angle: As the coating for an increased conversion efficiency only reaches a few channel diameters into the channel, there is a decreased quantum efficiency for photons entering the channel under an angle that leads to a collision with the wall

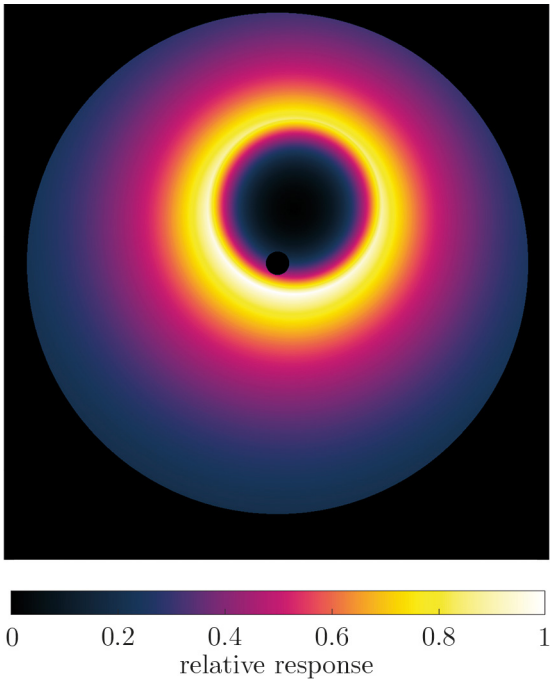

FIG. 3.11: Calculated relative response of the scattering detector to a point source. The 8° tilt of the MCP channels and the angular dependency of the quantum efficiency have been taken into account. Adapted from Ref. [200].

further inside the channel, i.e., where no additional coating is present.

The nonlinearity and spatial sensitivity of the detector have to be taken into account when comparing measured intensity distributions to calculated ones. However, the features (e.g., fringe spacing) of the scattering image are not affected, which already points to the usefulness of a feature-based analysis. The MCP has an effective diameter of 75 mm and is placed 65 mm away from the interaction region, thus leading to a maximum scattering angle $\theta_{\mathrm{max}} \approx 30°$ that can be recorded.

As the MCP detector is sensitive not only to scattered photons but also to ions and electrons generated during the interaction of the FEL pulse with the helium droplet, unwanted signal from charged particles needs to be suppressed. The front of the MCP is at a negative voltage that keeps electrons from reaching the detector. On the other hand, this accelerates positively charged ions onto the detector. As they need more time to reach the detector than the scattered photons, signal created by those ions can be effectively suppressed by switching the detector off (i.e., periodically reducing the amplification voltage) just after the photons have arrived. This process is referred to as *gating*.

Further, to improve the quality of the scattering image, background stray light coming from the FEL beamline needs to be subtracted. The background stray light depends on several FEL parameters (e.g., its wavelength, its intensity, its beam path / pointing) and therefore changes with time, but it is expected that shot to shot fluctuations are sufficiently small to be neglected. In order to monitor the straylight conditions during the measurement, a background image (i.e., with only the FEL and no sample present) is recorded every sixth FEL shot by automatically changing the source trigger and thereby intentionally not hitting a helium droplet with the FEL pulse.

3.2.3 The Helium Nanodroplet Source

The helium nanodroplet source was especially designed for being used in an imaging experiment. Its setup and characterization have been described in detail in my master's thesis [201]. The main design goal was to produce very large droplets (i.e., $N > 10^7$ atoms per droplet) that provide a sufficient (i.e., detectable) number of scattered photons when hit by an intense light pulse. The helium droplets are produced via supersonic expansion of helium into vacuum. The mean droplet size $\langle N \rangle$ depends on the temperature T_0 and the pressure p_0 of the helium in the gas reservoir, and the equivalent nozzle diameter d_{eq} (cf. Sec. 2.1). Larger droplets will form when increasing the pressure, using nozzles with a larger orifice, and decreasing the temperature. A higher pressure in the gas reservoir or increasing the nozzle diameter will lead to high gas loads in the expansion vacuum chamber, i.e., the droplet size is limited by the pumping speed of the vacuum pumps. Also, when the background pressure in the expansion chamber gets too high (e.g., because of a large amount of gas flowing through the nozzle), the droplets will be destroyed. In order to reduce the gas load while applying a high pressure, a pulsed valve is recommended. However, the operation of the valve will lead to an additional heat load at the cluster source that also depends on the opening time and the repetition rate of the valve, which will in turn decrease the mean droplet size. Further, stationary flow conditions in the supersonic beam will only be reached for sufficiently long opening times [202]. On the other hand, longer opening times will lead to more pronounced rebounces of the valve [202] that can be seen as additional weaker gas/droplet pulses after the main gas/droplet pulse. This behavior has also been observed for the helium droplet source used in this experiment [203]. As the occurrence of large droplets is less frequent in the pulses following the main gas/droplet pulse, the opening of the source should be exactly triggered in a way that the main gas/droplet pulse reaches the interaction region at the same time as the FEL pulse. For a high hit rate, it is important to ensure that the imaged droplets stem from the main pulse. This illustrates that the source parameters have to be carefully chosen. In general, the source should be able to reach very low temperatures at high gas loads for short (but not too short) gas/droplet pulses. The ideal pulse length also depends on the valve assembly and has to be checked experimentally.

A schematic drawing of the helium nanodroplet source is shown in Fig. 3.12 (a). It consists of a pulsed Even-Lavie valve [185] that is mounted on a closed-cycle cryostat. In general, the Even-Lavie valve is designed to deliver gas pulses that are about 50 µs long at pressures of up to 100 bar with a repetition rate of up to 1 kHz [185]. It is especially optimized for cryogenic operation and therefore attached to a Sumitomo RDK-205E cold head with a cooling power of 1 W. The cold head has two cooling stages delivering temperatures of 40 K and 4 K, respectively. At the first cooling stage, a gold plated heat shield made of oxygen free copper is attached, shielding thermal radiation from the vacuum chamber walls off the valve. At the second cooling stage, a gas pre-cooling and the Even-Lavie valve are attached. The gas supply and the operating current for the valve are provided via high vacuum feedthroughs. For temperature control, another two feedthroughs are used: One connecting two silicon diodes for exact temperature measurement that are attached to the heat shield and the copper body of the valve, and another one connecting two 50 Ω resistors that are attached to the valve as heaters. With this setup, the temperature T_0 that is measured directly at the valve can be controlled from cryogenic values to room temperature while the cryostat is constantly

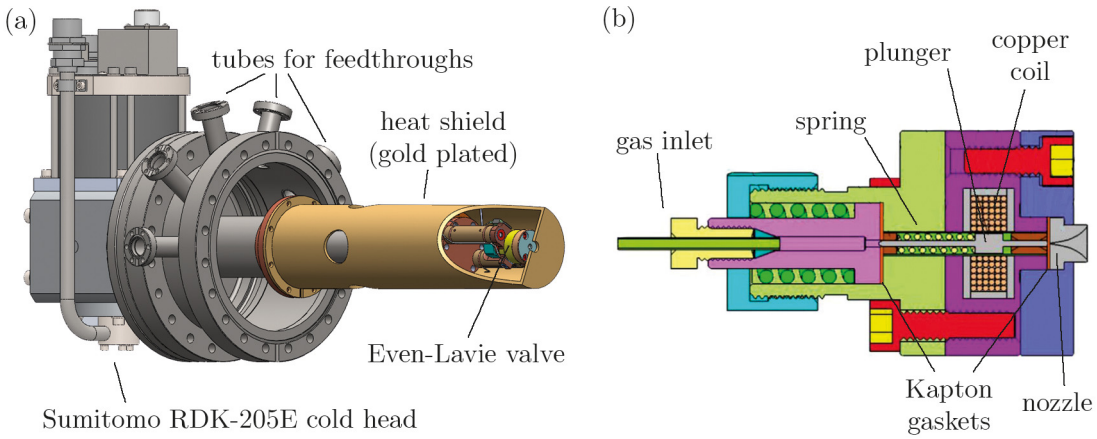

FIG. 3.12: Drawings of helium droplet source and Even-Lavie valve. (a) The source consists of an Even-Lavie valve that is mounted on a closed-cycle cryostat. A gold plated copper heat shield is mounted onto the cold head. (b) Drawing of the Even-Lavie valve. The plunger is made of a magnetic steel alloy and blocks the valve opening until it is retracted by the magnetic field applied through the copper coil. Adapted from Ref. [185].

running. The lowest temperature that can be reached depends mostly on the repetition rate of the valve, its opening time, and on the stagnation pressure p_0. In Fig. 3.12 (b), a schematic drawing of the Even-Lavie valve is shown to illustrate its working principle. It is equipped with a trumpet shaped nozzle that has a throat diameter of 100 µm and a half opening angle of 20°. A plunger is pressed by a spring against the nozzle (sealed with a Kapton gasket) to close the valve. The plunger, made of a magnetic steel alloy, is surrounded by a copper coil. When a current is applied to the coil, the plunger will be retracted and the gas can flow through the nozzle.

The operating conditions for the valve in this experiment are summarized in Tab. 3.2. The repetition rate of the valve was set to match the pulse structure of FERMI, which was operating at 10 Hz. Although the valve can handle repetition rates of up to 1 kHz, one should keep in mind that a higher repetition rate increases the heat load, thus raising the lowest temperature that can be reached. The opening time of the valve was set to 26 µs. Please note that the opening time of the valve describes the pulse length of the current that is applied to the copper coil retracting the plunger from its resting position, and not the duration of the resulting gas pulse. In the course of this experiment, the helium nanodroplet source exhibited very stable working conditions, i.e., a stable temperature of $T_0 = (5.4 \pm 0.1)$ K. For low temperature operation the valve must not be contaminated with gases other than helium, otherwise there is a high risk of gases solidifying inside the valve that may block the nozzle which may cause a complete maintenance of the source. In order to prevent this, the valve should be purged with high purity (99.9999 %) helium, e.g., by leaving the source running under vacuum for at least 12 hours at room temperature before cooling down. During the experiment, the source was running at low temperatures around-the-clock for seven consecutive days. This high reliability is an important prerequisite for an FEL experiment, where beam time is limited and should not be sacrificed for servicing or repairing equipment. As FERMI is nowadays operating at 50 Hz, a higher repetition rate for the valve can be considered. Although this will result in smaller droplets because of the higher heat load and therefore increased temperature T_0 at the valve, the droplet size should still be

TABLE 3.2: Source parameters used in this experiment

Parameter	Value
Repetition rate	10 Hz
Opening time	26 µs
Stagnation pressure p_0	80 bar
Temperature T_0	5.4 K
Nozzle diameter	100 µm
Nozzle half opening angle	20°

sufficiently large for a scattering experiment (stable operation was observed at 50 Hz repetition rate for an opening time of 23 µs, $T_0 = 5.9$ K), which will be tested in future experiments.

Chapter 4

Results and Discussion

A great advantage of recording wide-angle scattering images of individual nanoparticles is that from a single diffraction pattern, the three-dimensional particle shape and its orientation can be retrieved [13]. Further, the fragmentation dynamics of the particle can be traced by applying pump-probe schemes [124, 125] for time-resolved studies. This work follows both pathways.

In this thesis, the three-dimensional shapes and light induced dynamics of helium nanodroplets are determined from wide-angle scattering patterns. Pioneering studies on the shapes of helium nanodroplets using x-ray scattering were performed in the group of Andrey Vilesov by Gomez *et al.* [12] and Bernando *et al.* [15] at the LCLS FEL, while studies employing wide-angle scattering were conducted by Daniela Rupp *et al.* [22] at the Max Born Institute in Berlin and in the course of this thesis at the FERMI FEL [17]. They showed extreme deformations of the superfluid droplets by analyzing their two-dimensional shape projections [12, 15] and identified both oblate and prolate shapes by evaluating wide-angle scattering signal [15, 22]. The results of this work trace the transition from oblate to prolate shapes in detail [17], thus giving for the first time a complete three-dimensional characterization of the superfluid droplet morphology. Also, the first results of a time-resolved study on the dynamics of xenon doped helium nanodroplets after irradiation with an NIR laser pulse are presented. Therefore, an NIR pump-XUV probe setup at the FERMI FEL was employed to record a large data set of wide-angle scattering images of helium nanodroplets (cf. Sec. 3.2).

This chapter is organized as follows: In Sec. 4.1 an overview of the data is given. The data set is divided into two parts: First, *static data* are presented, where only the XUV pulse was used to record diffraction patterns of pristine helium nanodroplets. From these data, the three-dimensional droplet shapes are retrieved in Sec. 4.2. A comparison to theoretical models reveals that spinning superfluid helium nanodroplets exhibit the same shapes as rotating normal liquid droplets. Second, *dynamic data* are evaluated, where diffraction patterns of xenon doped helium nanodroplets were recorded with a delay of up to 800 ps after irradiation with the NIR pulse. These data give a first insight into the light induced dynamics in helium nanodroplets that are discussed in Sec. 4.3. While some droplets exhibit randomly distributed density fluctuations upon NIR excitation also structured fluctuations can be observed.

TABLE 4.1: Overview of the static data. The photon energy E_{ph}, FEL wavelength λ_{FEL}, FEL focus intensity I_{FEL}, and hit rate are given.

E_{ph} (eV)	λ_{FEL} (nm)	I_{FEL} (W cm^{-2})	Hit rate (%)
19.1	65.0	6.5×10^{14}	21.1
19.4	63.8	6.6×10^{14}	28.5
20.5	60.4	8.7×10^{14}	26.1
21.0	59.0	8.0×10^{14}	17.9
21.5	57.6	3.4×10^{14}	17.8
23.7	52.3	8.0×10^{14}	16.7
38.5	32.2	7.9×10^{14}	13.2

TABLE 4.2: Overview of the dynamic data. The photon energy E_{ph}, FEL wavelength λ_{FEL}, FEL focus intensity I_{FEL}, hit rate, and doping level of xenon atoms embedded in the helium nanodroplets are given.

E_{ph} (eV)	λ_{FEL} (nm)	I_{FEL} (W cm^{-2})	Hit rate (%)	Doping level
19.4	63.9	6.7×10^{14}	23.2	Low
19.4	63.9	3.0×10^{14}	14.7	Medium
19.4	63.9	5.3×10^{14}	19.3	High
21.5	57.7	4.2×10^{14}	13.6	Medium

4.1 Data Overview

In the course of this experiment, a total of ∼220 000 images exhibiting scattering signal from helium nanodroplets have been recorded at different photon energies, doping levels and pump-probe delays. In general, the recorded scattering images can be divided into XUV-only measurements (which are referred to as static data) and NIR pump-XUV probe measurements (also referred to as dynamic data). For the results shown in this thesis ∼85 000 images were analyzed: (i) The static data set comprises 38 150 images of pristine helium nanodroplets that were recorded using only the XUV FEL pulse. An overview of the static data is given in Tab. 4.1. (ii) The dynamic data set consists of 46 852 images of xenon doped helium nanodroplets at various delays after NIR laser excitation, which is only a fraction of the total number of pump-probe images that were recorded. The analysis had to be performed manually: Because of the complexity of the data, an automated approach was not feasible. In general, a manual classification of the scattering patterns is always needed before sophisticated algorithms for pattern recognition can be developed that are able to handle the specific data. Therefore, the whole data set was reviewed, and as no substantial differences in the diffraction patterns were observed (i.e., the images exhibited similar features), the analysis was deliberately restricted to this smaller subset comprising about one quarter of the pump-probe images. An overview of the dynamic data is given in Tab. 4.2.

Overall, the hit rate (i.e., the percentage of images exhibiting detectable scattering signal) ranges from 10 % to 30 %. It fluctuates with the performance of the FEL

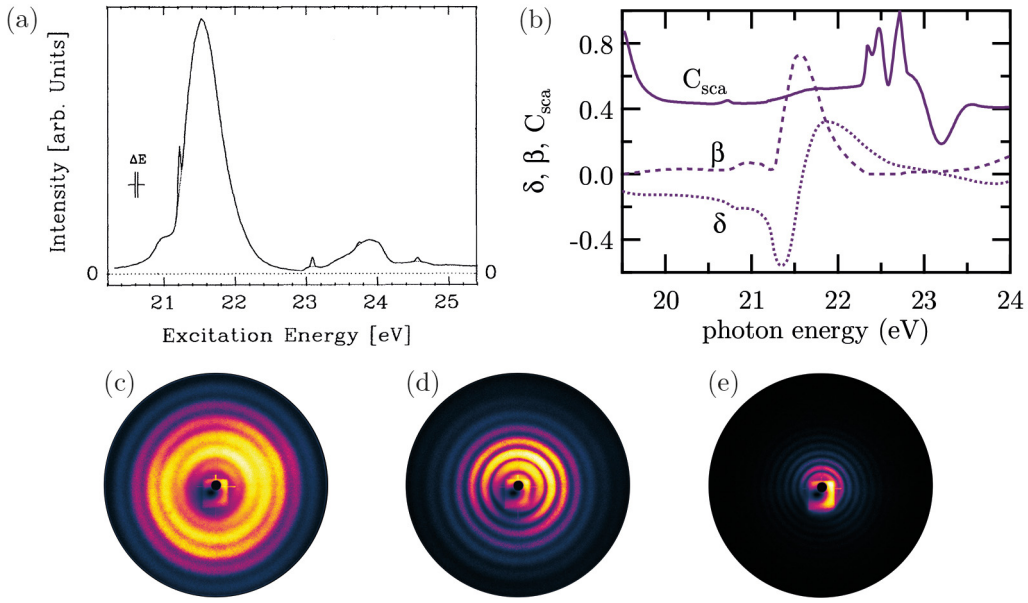

FIG. 4.1: (a) Fluorescence excitation spectrum of helium nanodroplets (mean radius $\langle R \rangle \approx 5\,\text{nm}$). A broad absorption band can be observed around 21.5 eV, which corresponds to the dominant $1s \rightarrow 2p$ transition. Adapted from Ref. [204]. (b) Refractive index $\underline{n} = 1 - \delta + i\beta$ for liquid helium (data are taken from Ref. [205]) and calculated normalized scattering cross section C_{sca} for a droplet with radius $R = 450\,\text{nm}$ using a Mie scattering code [206, 207]. The unusual behavior of the scattering cross section is due to the droplet size as the approximation $C_{\text{sca}} \propto \delta^2 + \beta^2$ is not valid for large droplets. (c)-(e) Representative raw scattering images of a droplet with $R = (450 \pm 10)\,\text{nm}$, recorded at photon energies $E_{\text{ph}} = 19.4\,\text{eV}$ (below resonance), $E_{\text{ph}} = 21.5\,\text{eV}$ (on resonance), and $E_{\text{ph}} = 38.5\,\text{eV}$ (above resonance), respectively.

as well as the helium nanodroplet source and is, in general, dependent on the FEL wavelength. An overview on the optical properties of helium nanodroplets is given in Fig. 4.1. In this experiment, photon energies ranging from $E_{\text{ph}} = 19.4\,\text{eV}$ to $38.5\,\text{eV}$ were used (cf. Tables 4.1 and 4.2), thus covering the resonance of liquid helium. In Fig. 4.1 (a), a fluorescence excitation spectrum of helium nanodroplets (mean radius $\langle R \rangle \approx 5\,\text{nm}$), taken from Ref. [204], is shown. It is assumed that this represents the absorption cross section of medium sized helium nanodroplets for photon energies below the ionization potential $E_{\text{IP}} = 24.6\,\text{eV}$ of helium [204]. The sharp lines in the spectrum are due to atomic transitions of the surrounding helium gas, while the first band at around $\sim$21.0 eV is attributed to the otherwise forbidden $1s \rightarrow 2s$ transition which is allowed at the surface of the droplets where the symmetry is broken. The dominant absorption band at $\sim$21.5 eV corresponds to the atomic $1s \rightarrow 2p$ transition, while the bands observed at higher photon energies belong to the higher lying $1s \rightarrow np$ transitions ($n > 2$). It follows that with the photon energies provided by the FERMI FEL, helium nanodroplets can be probed non-resonantly (i.e., below the $1s \rightarrow 2s$ resonance at $E_{\text{ph}} \sim 21.0\,\text{eV}$), on the resonance ($E_{\text{ph}} \sim 21.5\,\text{eV}$) and above their ionization potential at $E_{\text{ph}} \sim 24.6\,\text{eV}$, yielding a different absorption of the FEL pulse (and its energy) in the droplet. In Fig. 4.1 (b), the complex refractive index $\underline{n} = 1 - \delta + i\beta$ for bulk liquid helium is shown (data are taken from Ref. [205]). Here, δ describes the deviation of the refraction from unity and β represents the absorption. In the case of scattering by a multi-electron atom, the scattering cross section C_{sca} is proportional to $\delta^2 + \beta^2$ (cf.

chapter 2 in the book *X-Rays and Extreme Ultraviolet Radiation* by D. Attwood and A. Sakdinawat [208]), i.e., C_{sca} is larger the more δ and β deviate from zero. While this approximation might be transferred to small droplets, it is not applicable for large droplets. In the latter case, the scattering cross section C_{sca} can be calculated from δ and β using Mie theory [139]. It is the analytical solution of the Maxwell equations for scattering of a plane wave on a homogeneous sphere in a nonabsorbing environment, when the diameter of the sphere is comparable to the wavelength of the incident light. For the calculation of C_{sca}, a MATLAB computer code [206, 207] is used that is based on the book *Absorption and Scattering of Light by Small Particles* by C. F. Bohren and D. R. Huffman [152]. In Fig. 4.1 (b), the calculated scattering cross section C_{sca} for a droplet with radius $R = 450\,\mathrm{nm}$ is shown. It can be seen that for large droplets, C_{sca} is particularly high in regions where β is close to zero and δ is different from zero. In this case, there is almost no absorption while the refraction deviates from one, and the scattering signal increases with the length the light wave has traveled inside the medium, i.e., with increasing particle size. On the other hand, when the absorption is high, the influence of the refraction on the scattered light decreases. Therefore, for photon energies $E_{\mathrm{ph}} < 20\,\mathrm{eV}$ the scattering cross section increases, while the resonance at $E_{\mathrm{ph}} \sim 21.5\,\mathrm{eV}$ has no drastic influence on C_{sca}. A peak can be observed for photon energies around $E_{\mathrm{ph}} \sim 22.7\,\mathrm{eV}$ with a significant decrease of the scattering cross section for higher photon energies. Please note that this behavior of C_{sca} depends on the droplet size (in Appendix A, calculations of C_{sca} for different droplet sizes are shown). In Figs. 4.1 (c)–(e), raw scattering images of droplets with a radius $R = (450 \pm 10)\,\mathrm{nm}$ are shown for photon energies $E_{\mathrm{ph}} = 19.4\,\mathrm{eV}$ (below resonance), $E_{\mathrm{ph}} = 21.5\,\mathrm{eV}$ (on resonance), and $E_{\mathrm{ph}} = 38.5\,\mathrm{eV}$ (above resonance), respectively. The clearly visible change in scattered intensity on the images is probably due to the development of the scattering cross section C_{sca} with photon energy E_{ph}.

In the following, the processing of the scattering images for further analysis is presented, the droplet size distribution is retrieved from the diffraction patterns of spherical droplets, and the number of dopants per droplet is determined for the three doping levels employed in this experiment.

4.1.1 Processing of Scattering Images

Before the recorded scattering images can be analyzed in detail, they have to be corrected for several artifacts. At FEL facilities, the laser pulses typically have to travel a distance of several tens or hundreds of meters until they reach the experiment. During the propagation along the beamline and also in the experimental chamber, unwanted straylight is produced that obfuscates the scattering signal. While a lot of effort is already made during the experiment to reduce the straylight (e.g., by using movable apertures and blades along the beam path), it can never be fully suppressed. Further, imperfections of the detector such as an inhomogeneous sensitivity across its surface or saturation effects have to be compensated for. This is conveniently done in the post processing of the data.

In Fig. 4.2, the processing of the scattering images is exemplified. The raw image, i.e., without any corrections, is shown in Fig. 4.2 (a). Several features are clearly visible that can be directly attributed to the detector geometry as discussed in Sec. 3.2.2. The central hole of the detector can be seen that lets the FEL- and NIR laser-beam pass. To the bottom left, a region of decreased intensity can be seen that is due to the 8°

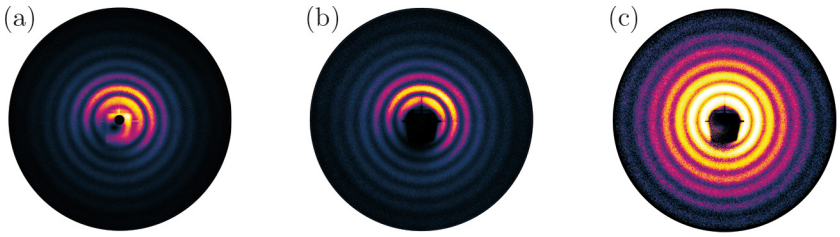

FIG. 4.2: Processing of scattering images. (a) Raw data. (b) Background subtracted and $\cos^{-3}(\theta)$ correction applied. (c) Background subtracted, with $\cos^{-3}(\theta)$ and detector sensitivity correction applied, logarithmic scaling.

bias angle of the channels. An additional decrease of intensity is probably due to the hole in the mirror behind the MCP/phosphor screen stack. Because of the laser beam divergence, this second hole has to be larger than the detector hole. As the camera is filming the detector's phosphor screen via the mirror, an offset of the mirror with respect to the optical axis leads to a spot of seemingly reduced intensity on the detector. In this experiment, the mirror was probably not perfectly aligned, as on the detector a darker region was observed whose position could be moved around by tilting the camera. In order to minimize its impact on the quality of the scattering images, the camera was slightly tilted in a way that this region was brought to overlap with the spot of decreased sensitivity caused by the 8° bias angle. Reduction of the straylight coming from the beamline was performed using a system of four blades (cf. the experimental setup in Sec. 3.2.1). It is designed to be tightly closed around the FEL beam, i.e., to cut out the straylight around the center of the detector. However, as the incoupling of the NIR laser beam is under a small angle with respect to the FEL, one side of the blade system could not be closed as much as the other sides. In the scattering image, this results in a rectangular region of intense straylight shifted to the bottom of the detector center. Further, diffraction at the blades leads to a fine cross that can be seen at the edges of the straylight rectangle.

The straylight is removed from the recorded scattering images by performing a background subtraction as shown in Fig. 4.2 (b). The straylight background, e.g., the rectangle and the cross, is present in every shot of the FEL, also when no droplet is hit. Such an *empty* image can be used to subtract the straylight from an image where scattering from a droplet is visible. However, the straylight strongly depends on the current conditions of the FEL (e.g., intensity, pointing, wavelength, etc.) and it is desirable to record the background image shortly before or after the scattering image was taken. At FERMI, background images can be recorded at a fixed period by automatically changing the trigger of the source valve that, e.g., every sixth shot of the FEL does not overlap with the droplet pulse of the source. A working background subtraction turns the straylight regions in the image dark, as can be seen in Fig. 4.2 (b). Further, as the scattered light is mapped onto the flat detector, a correction dependent on the scattering angle θ is performed that multiplies the recorded intensity by a factor of $\cos^{-3}\theta$ [120], thus increasing the signal at higher scattering angles. These are the corrections included in the further analysis of the images.

In a last step, the inhomogeneous detector sensitivity is addressed. As can be seen in Fig. 4.2 (c), it compensates for the fluctuations of the angular intensity (i.e., along the rings). A detector response function is determined by summing up all scattering images exhibiting concentric circles and dividing the detector into equal sectors. Then,

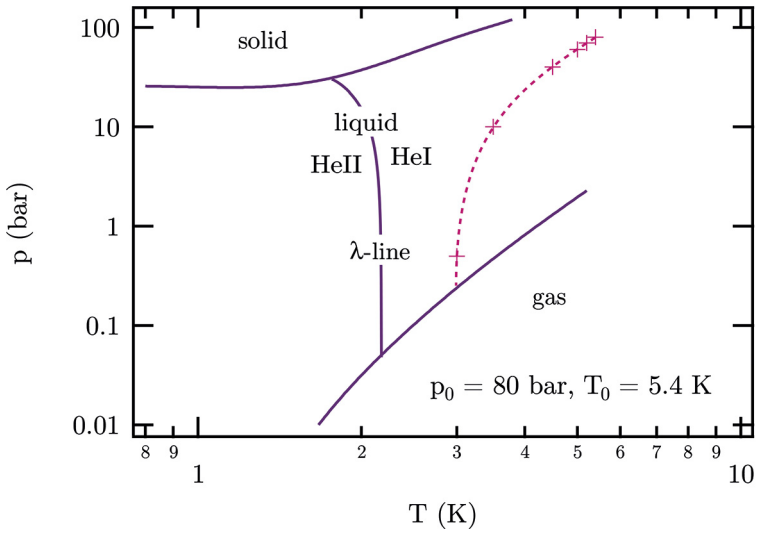

FIG. 4.3: Phase diagram showing the isentropic expansion of He at $p_0 = 80\,\text{bar}$ and $T_0 = 5.4\,\text{K}$. Data for isentrope (crosses, dashed line as a guide to the eye) are taken from Ref. [211]. The so-called *λ-line* separates the normal liquid phase (HeI) from the superfluid phase (HeII).

a sector from the upper right quadrant of the detector is chosen as a reference for the intensity distribution from the center to the edge of the detector. All other sectors get adjusted to that reference by either increasing or lowering their radial intensity, resulting in the evenly distributed angular intensity shown in Fig. 4.2 (c). Please note that this processing step is only performed for presentation purposes, leaving the data unchanged for further analysis where the detector's inhomogeneous sensitivity and its nonlinear signal amplification still need to be considered. Finally, the image is set to logarithmic scaling, also only for presentation purposes. All scattering images shown in the following have been processed in this way.

4.1.2 Size Distribution of Spherical Helium Nanodroplets

An important parameter for all cluster beam experiments is the mean number of atoms per cluster $\langle N \rangle$, as many physical properties change with cluster size. For gas phase clusters, it is in general difficult to experimentally retrieve. For helium nanodroplets, mean droplet sizes have been determined using crossed beam methods [209], electrostatic deflection techniques [210], or titration measurements [64]. As discussed in Sec. 2.1, the mean droplet size $\langle N \rangle$ depends on the expansion conditions, i.e., on the stagnation pressure p_0 and the temperature T_0 of the helium in the reservoir. Further, the resulting size distribution was reported to be log-normal for expansion from the gas phase [209] and exponential for expansion from the liquid phase [210]. In this experiment the stagnation conditions were $p_0 = 80\,\text{bar}$ and $T_0 = 5.4\,\text{K}$. In Fig. 4.3, the isentropic expansion of helium is shown for these conditions (crosses, dashed line as a guide to the eye). From the phase diagram, one can clearly see that the expansion takes place in the supercritical regime. Therefore, an exponential size distribution is expected.

In order to retrieve the droplet size distribution, scattering images of spherical droplets are analyzed. As is shown in Fig. 4.1 (c)–(e), they exhibit concentric rings. The spacing of the rings is determined by the radius of the droplet and can therefore be used to

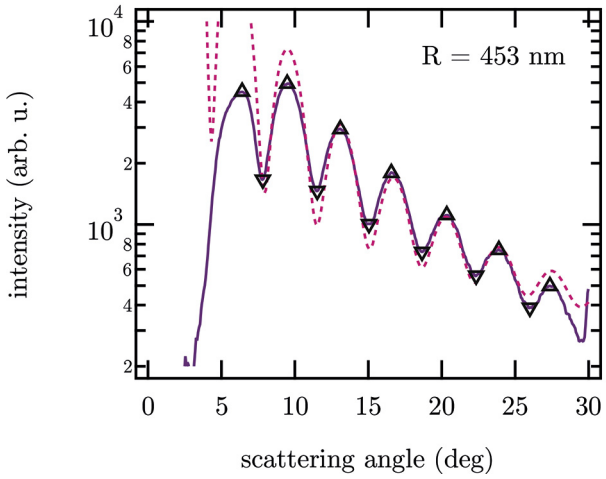

FIG. 4.4: Determination of droplet radius R. The radial profile (solid line) of a spherical droplet's diffraction pattern is fitted with a calculated Mie profile (dashed line, $\lambda_{\mathrm{FEL}} = 57.6\,\mathrm{nm}$, for refractive index see Tab. 4.3). The intensity of the measured profile deviates from that of the calculated one because of saturation effects and the nonlinearity of the detector. However, to determine the droplet radius only the positions of the maxima and not their intensities have to be taken into account.

retrieve the particle size. The basic idea is to compare the spacing of the maxima in the radial profile of the scattering pattern (i.e., the normalized integrated intensity along concentric circles) to a simulated profile. For each scattering image of a spherical droplet, the profile is computed by radially integrating over the upper right quarter of the scattering detector. For comparison, a simulated Mie profile of the forward-scattered light is calculated using the same Mie code as mentioned in Sec. 4.1. The values for the complex refractive index of liquid helium $\underline{n} = 1 - \delta + i\beta$ depend on the wavelength and are given in Tab. 4.3 for the wavelengths used in this experiment. To exemplify the droplet size analysis, in Fig. 4.4 the radial profile (solid line) of a scattering image taken at $\lambda_{\mathrm{FEL}} = 57.6\,\mathrm{nm}$ is compared to a calculated Mie profile (dashed line) up to the maximum scattering angle $\theta_{\mathrm{max}} = 30°$. It can be seen that the intensity of the measured profile deviates from the calculated one. This is due to saturation effects and the nonlinearity of the scattering detector. However, the droplet size analysis only depends on the positions of the maxima and not their intensities, which are therefore not taken into account. An automated algorithm [212] minimizes the discrepancy of the maxima positions returning the droplet radius R with an accuracy of 1 nm (under the assumption of a perfectly spherical particle and correct optical properties). For small droplets, where only the first minimum at a scattering angle θ_1 is visible on the detector, the droplet radius can be estimated using the formula for the Airy disk:

$$R \approx 0.61 \cdot \frac{\lambda_{\mathrm{FEL}}}{\sin\theta_1}. \tag{4.1}$$

Overall, the radii for 18 392 droplets have been retrieved from scattering images recorded at photon energies $E_{\mathrm{ph}} = 19.4\,\mathrm{eV}$ to $38.5\,\mathrm{eV}$, thus covering almost the whole range used in this experiment. However, as it had to be manually checked that the simulated profiles match the experimental data, the size determination was restricted to about half the static data set. The resulting distribution is very broad (FWHM $\approx 190\,\mathrm{nm}$), as can be seen in Fig. 4.5 (a). From Eq. (4.1) it follows that for droplets smaller than 80 nm

TABLE 4.3: Refractive index $\underline{n} = 1 - \delta + i\beta$ of liquid helium in the XUV regime, selected for wavelengths λ_{FEL} used in this experiment.

λ_{FEL} (nm)	E_{ph} (eV)	$(1-\delta)$	β
32.2	38.5	0.9864[a]	0.0196[a]
52.3	23.7	1.0543[b]	0.0518[b]
57.6	21.5	1.3035[b]	0.7028[b]
59.0	21.0	1.2138[b]	0.0700[b]
60.4	20.5	1.1473[b]	0.0263[b]
63.8	19.4	1.0845[b]	0.0000[b]
65.0	19.1	1.0403[b]	0.0000[b]

[a] Ref. [213]
[b] Ref. [205]

the first minimum cannot be detected, as $\theta_1 > \theta_{\max}$. The smallest droplet detected in this experiment has a radius $R = 89\,\mathrm{nm}$. As this value is well above the smallest detectable droplet size, it is assumed that the size distribution is fully covered and not cut off at the lower end. However, it should be noted that the scattering technique tends to overestimate larger droplets, as for small droplets, the scattered intensity might be below the detection limit: In order to create sufficient scattering signal, smaller droplets have to be exposed to higher FEL intensities. Assuming a gaussian profile for the FEL beam, the focal volume where this condition is met decreases for smaller droplet sizes yielding a lower probability to detect small droplets. Also, the scattering cross section changes with droplet size: The increase that can be seen in Fig. 4.1 (b) around 19.5 eV and 22.7 eV is mainly due to larger droplets. This presumably results in a further dominance of larger droplets, especially for these photon energies. Towards larger radii, the resolution of the detector limits the maximum detectable droplet size. The largest droplet observed has a radius $R = 1300\,\mathrm{nm}$, with fringes that can still be resolved without any problems. Again, it follows that the size distribution is probably not cut off at the upper end. The number of atoms per droplet N is connected to the droplet radius R via the expression [53]

$$N = (R/0.222\,\mathrm{nm})^3, \tag{4.2}$$

resulting in the droplet size distribution shown in Fig. 4.5 (b). The expansion from the liquid phase yields an exponential distribution from which the mean droplet size $\langle N \rangle$ can be determined by fitting a function $f(N) = \text{const.} \times \exp(-N/\langle N \rangle)$ to its falloff [210]. This gives a mean droplet size $\langle N \rangle = 6 \times 10^9$ atoms per droplet which corresponds to a mean radius $\langle R \rangle \approx 400\,\mathrm{nm}$ using Eq. (4.2). However, the arithmetic mean of the determined droplet radii is $\bar{R} = 350\,\mathrm{nm}$, which is about 13 % smaller than $\langle R \rangle$. This discrepancy is probably caused by the exponential fit underestimating the smaller droplet sizes, thus leading to a smaller slope of the fit and therefore a larger mean droplet size. It is possible that the fitting procedure proposed in Ref. [210] cannot be transferred to droplet sizes determined via light scattering on individual droplets, where parts of the size distribution are suppressed due to insufficient scattering signal. Nevertheless, in order to enable a comparison to literature [210] it is reasonable to determine the mean number of atoms per droplet as described.

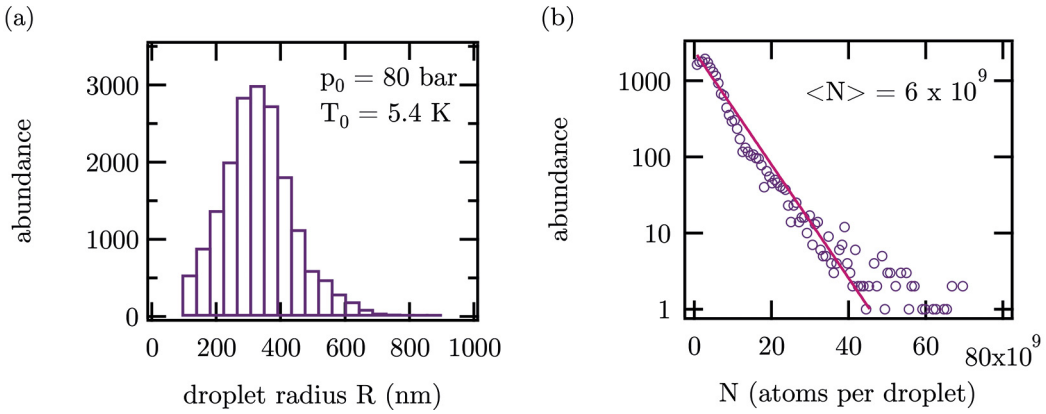

FIG. 4.5: Droplet size distribution for expansion parameters $p_0 = 80\,\mathrm{bar}$, $T_0 = 5.4\,\mathrm{K}$, as determined by Mie fits to diffraction patterns of spherical helium nanodroplets (cf. Fig. 4.4). (a) Distribution of droplet radii R. (b) Distribution of droplet sizes N. The mean size $\langle N \rangle = 6 \times 10^9$ atoms per droplet was determined by a fit of the function $f(N) = \text{const.} \times \exp(-N/\langle N \rangle)$ to the exponential falloff of the distribution [210].

4.1.3 Doping of Helium Nanodroplets

Doping of helium nanodroplets is a relatively straight forward technique, as a dopant atom or molecule gets effectively cooled upon collision with the droplet and will be therefore trapped inside the droplet or attached to its surface. The cooling of the dopant atom is promoted by a significant number of helium atoms evaporating from the droplet, a process keeping the helium nanodroplet at a temperature of 0.4 K. Therefore, the droplet has to be sufficiently large (typically, at least $\langle N \rangle > 1000$) in order to survive the doping process. In most experiments employing doping of helium nanodroplets, the droplets serve as a cooling matrix to enable high resolution spectroscopy of the dopant species (for a review, see Ref. [26]). In this experiment, however, the dopant atoms are used to facilitate the ignition of a nanoplasma inside the helium droplet by irradiation with an intense NIR laser pulse [142] in order to investigate the subsequent fragmentation dynamics. In the course of this study, three different levels of xenon atoms embedded in helium nanodroplets – referred to as low, medium, and high doping (cf. Tab. 4.2) – have been used. In the following, these doping levels are further quantified in terms of the average number of dopant atoms per droplet and the decreased droplet radius because of the evaporation of helium atoms.

The pick up statistics for dopant atoms in helium nanodroplets have already been discussed in Sec. 2.1.3 and it has been shown that when a large number of atoms are picked up, the number of dopant atoms per droplet k is simply given by the number of collisions $\tilde{z}$ [cf. Eq. (2.16)]. This is typically the case for large helium droplets (i.e., with a radius R of a few hundred nanometers), where already particle densities in the range of ultra high vacuum ($\sim 1 \times 10^{15}\,\mathrm{m}^{-3}$ at $1 \times 10^{-7}\,\mathrm{mbar}$) lead to the capture of foreign species. The captured atoms move freely inside the superfluid droplet and may coagulate inside the ultracold environment. For the coagulation cross section σ_{coag}, an upper limit can be approximated by the classical cross section of the droplet $\sigma_{\mathrm{tot}} = \pi R^2$, as $\sigma_{\mathrm{coag}} \leq \sigma_{\mathrm{tot}}$ [57]. The particle density of the xenon atoms in the gas cell is given by $n_{\mathrm{Xe}} = p_{\mathrm{Xe}}/(k_{\mathrm{B}} T_{\mathrm{Xe}})$, where p_{Xe} is the pressure in the gas cell, k_{B} is the Boltzmann constant and T_{Xe} is the temperature of the xenon atoms. For a droplet with a mean

TABLE 4.4: Summary of the values used for the calculation of the average number of picked up xenon atoms per droplet $\bar{k}$ [Eq. (4.3)].

Parameter	Quantity	Value
Mean droplet radius[a]	$\langle R \rangle$	400 nm
Droplet velocity[b]	v_D	320 m s^{-1}
Molar mass of He	M_He	4 g mol^{-1}
Gas cell length[b]	L	35.3 mm
Temperature of Xe in gas cell	T_Xe	293 K
Molar mass of Xe	M_Xe	131 g mol^{-1}
Velocity of Xe in gas cell[c]	v_Xe	218 m s^{-1}

[a] cf. Sec. 4.1.2
[b] cf. Sec. 3.2.1
[c] cf. Eq. (2.17)

radius $\langle R \rangle$, the average number of picked up atoms $\bar{k}$ is then given by

$$\bar{k} = n_\mathrm{Xe}\sigma_\mathrm{tot}L\frac{\sqrt{v_\mathrm{D}^2 + v_\mathrm{Xe}^2}}{v_\mathrm{D}} = \frac{p_\mathrm{Xe}}{k_\mathrm{B}T_\mathrm{Xe}}\pi\langle R\rangle^2 L\frac{\sqrt{v_\mathrm{D}^2 + v_\mathrm{Xe}^2}}{v_\mathrm{D}}, \tag{4.3}$$

where v_Xe is the mean thermal velocity of the xenon atoms in the gas cell [cf. Eq. (2.17)]. The experimental values needed to calculate $\bar{k}$ are summarized in Tab. 4.4.

During the experiment, the pressure of the xenon atoms in the gas cell p_Xe has not been measured directly, but the pressure in the doping chamber surrounding the gas cell, p_dop, was measured. Nevertheless, using general equations for the flow of gases [214], p_Xe can be estimated from pressure values measured for helium gas in the cell p_He by O. Plekan [215] with the helium droplet source running at the same conditions, cf. Fig. 4.6. In general, the volumetric flow rate $\dot{Q}$ from the doping chamber through the vacuum pump should equal the throughput from the gas cell to the doping chamber: $\dot{Q} = S_M \cdot p_\mathrm{dop} = C_\mathrm{a}\Delta p$. Here, S_M is the pumping speed for the dopant gas, and $C_\mathrm{a} = 1/4 \cdot v_M A \sim 1/\sqrt{M_M}$ is the molecular orifice conductance with aperture area A, velocity v_M, and molar mass M_M of the respective gas. The pressure difference $\Delta p = p_M - p_\mathrm{dop}$ is given by the pressure of the dopant gas in the cell p_M and the pressure in the doping chamber p_dop. Since the pressure in the gas cell is several orders of magnitude higher than in the doping chamber, it is $\Delta p \approx p_M$. In the case of the gas cell filled with xenon, p_Xe, and in the case of helium, p_He, when the pressure in the doping chamber p_dop is the same, it follows:

$$p_\mathrm{Xe} = p_\mathrm{He}\sqrt{\frac{M_\mathrm{Xe}}{M_\mathrm{He}}} \cdot \frac{S_\mathrm{Xe}}{S_\mathrm{He}}. \tag{4.4}$$

Assuming that the pumping speed for xenon S_Xe is typically about half the pumping speed for helium S_He, this yields $p_\mathrm{Xe} \approx 3 \cdot p_\mathrm{He}$. The doping levels used in this experiment and corresponding average number of dopants per droplet $\bar{k}$ are summarized in Tab. 4.5.

Each dopant atom that is captured by the helium droplet introduces an additional energy E_tot to the droplet that is given by Eq. (2.21). It is the sum of the collisional

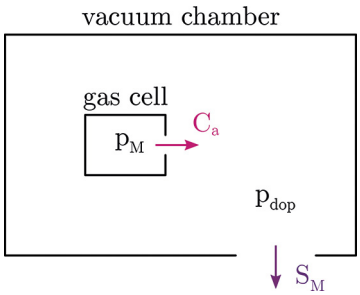

FIG. 4.6: Pressure measurement in the doping chamber of the LDM end station. When the pressures in the gas cell p_M and in the doping chamber p_{dop} are known for the gas cell filled with one dopant gas (e.g., helium, p_{He}), the pressure in the gas cell for another dopant gas can be estimated using the molecular orifice conductance of the cell C_{a} and the pumping speed of the dopant gas S_M (e.g., xenon, $p_{\mathrm{Xe}} \approx 3 \cdot p_{\mathrm{He}}$). For details see text.

TABLE 4.5: Doping levels and corresponding number of dopants $\bar{k}$ that get picked up by a droplet with radius $\langle R \rangle = 400\,\mathrm{nm}$. The additional energy introduced to the droplet by picking up a xenon atom leads to the evaporation of $\Delta N_{\mathrm{evap}} = 508$ helium atoms from the droplet and therefore to a reduction of the droplet size. Depending on the doping level, the resulting droplet radius $\langle R' \rangle$ and the ratio of xenon atoms to helium atoms in the droplet Xe/He are given.

Doping level	p_{dop} (mbar)	p_{Xe} (mbar)	$\bar{k}$	$\langle R' \rangle$ (nm)	Xe/He (‰)
Low	5×10^{-7}	5×10^{-4}	2.7×10^{5}	397	0.05
Medium	3×10^{-6}	3×10^{-3}	1.6×10^{6}	381	0.3
High	1×10^{-5}	1×10^{-2}	5.3×10^{6}	328	1.6

energy $\langle E_{\mathrm{coll}} \rangle$ (assuming a complete energy exchange), the binding energy of the dopant atom to the droplet E_{bind}, and the binding energy E_{M} of the dopant atom to a pre-existing dopant cluster in the droplet. With the values given in Tab. 4.4, the internal rovibrational energy of a xenon atom $E_{\mathrm{int}}(\mathrm{Xe}) = 0$, the binding energy of xenon to bulk liquid helium $E_{\mathrm{bind}}(\mathrm{Xe}) = 26\,\mathrm{meV}$ [59], and the binding energy of bulk xenon $E_{\mathrm{Xe}} = 172\,\mathrm{meV}$ [216] it follows:

$$E_{\mathrm{tot}} = \frac{3k_BT}{2} + \frac{M_{\mathrm{Xe}}v_{\mathrm{D}}^2}{2N_{\mathrm{A}}} + E_{\mathrm{bind}}(\mathrm{Xe}) + E_{\mathrm{Xe}} \approx 305\,\mathrm{meV}. \tag{4.5}$$

The number of helium atoms that are evaporated from the droplet following the capture of each xenon atom can then be calculated using the binding energy of bulk liquid helium $E_{\mathrm{He}} = 0.6\,\mathrm{meV}$ [59] as

$$\Delta N_{\mathrm{evap}} = \frac{E_{\mathrm{tot}}}{E_{\mathrm{He}}} \approx 508. \tag{4.6}$$

With the average number of captured xenon atoms per droplet $\bar{k}$, the total number of evaporated helium atoms and therefore the decreased radius $\langle R' \rangle$ of the droplet after passing the gas cell can be calculated. The resulting values for the different doping levels are given in Tab. 4.5. It can be seen that in the case of high doping, this yields a shrinking of the mean droplet radius of up to 20 %. However, at medium doping, where most of the scattering images of the dynamic data set were recorded, the droplets

shrink about 5 % because of the doping process, which is assumed to be a negligible decrease. Overall, the amount of xenon atoms per droplet stays well below 2 ‰ and would not exceed this value even if the smaller average radius $\bar{R} = 350\,\text{nm}$ is assumed for the droplets. It should be noted that during the process of doping and cooling by evaporation, the continuous decrease of the droplet radius and therefore the droplet's geometrical cross section leads also to a decrease of the number of collisions (i.e., fewer dopants are picked up), which has not been taken into account for the estimate of the total number of dopants captured by the droplet. In order to give a more accurate estimate of the final droplet radius, this should be considered in a refined model of the pick up process, as it has been addressed, e.g., for alkali clusters in Ref. [217]. Nevertheless, even with the rough estimate presented here giving a lower limit for the final droplet radius, the droplets remain large (i.e., $\langle R' \rangle > 300\,\text{nm}$) and therefore no significant influence on the fragmentation dynamics is expected from this effect. Further, as the ratio of xenon atoms to helium atoms in the droplet remains small, it is assumed that once the number of xenon atoms needed to ignite a nanoplasma inside the droplet is exceeded, the doping levels used in this work do not fundamentally change the following dynamics.

4.2 Shapes of Helium Nanodroplets

Helium nanodroplets are weakly bound systems that have to be produced artificially by a free jet expansion at cryogenic temperatures and that can only exist in vacuum. When expanded from the liquid phase, the droplets can gain angular momentum. In a *normal liquid* droplet this leads to pronounced deformations: With increasing angular momentum, because of the balance of centrifugal force and surface tension, the droplets exhibit at rest spherical, then oblate and prolate shapes that have been described both experimentally [100, 104–107, 218] and theoretically [102, 103, 108] before (see also Fig. 2.13). In contrast, a *superfluid liquid* cannot rotate as a rigid body [93]. In a superfluid droplet, the rotational energy is expected to be stored in surface waves [109] or quantized vortices inside the droplet [110, 111] that might affect its equilibrium shape. Studying the shapes of individual helium nanodroplets can therefore give an insight into the interplay of superfluidity and droplet morphology on a nanometer scale. While first indications of vortices in helium nanodroplets have been found by investigating deposited residuals of silver doped droplets via transmission electron microscopy [112], their existence was proven in a pioneering CDI experiment at the LCLS FEL [12]. In the latter study, also the droplets' shape projections were reconstructed from the scattering patterns revealing extreme deformations. These were explained by the superfluid droplets becoming more and more oblate, thus exhibiting a stability range that extends beyond the classical limit for equilibrium shapes [12]. The existence of the extremely oblate, wheel-shaped droplets was ultimately attributed to the presence of vortex arrays inside the droplets [113]. However, retrieving the shape of a particle from its two-dimensional projection is a complicated task. Therefore, three-dimensional information on individual helium nanodroplets was collected in subsequent studies by recording diffraction patterns up to large scattering angles, giving clear evidence that also prolate helium nanodroplets exist [15, 22]. Assuming it is unlikely that both oblate and prolate equilibrium solutions of the droplet shape are stable configurations at the same time, this raises the question whether the shapes of spinning superfluid droplets keep evolving along the oblate branch when reaching the stability limit or start following

the prolate branch, just like their classical counterparts.

In order to address this question, the present work aims at thoroughly characterizing the three-dimensional shapes of spinning helium nanodroplets. Therefore, the three-dimensional shape-retrieval procedure based on the scattering images of individual helium nanodroplets is explained in detail. For the analysis, only images from the static data set were used. Most of the results presented here have been published in Langbehn *et al.*, Phys. Rev. Lett. **121**, 255301 (2018) [17].

First, the classification of the characteristic features in the diffraction patterns is described in Sec. 4.2.1. Second, the procedure to determine the three-dimensional shapes of the droplets is presented in detail in Sec. 4.2.2. Third, the retrieved shapes of spinning helium nanodroplets are discussed and compared to theoretical shapes of normal liquid rotating droplets in Sec. 4.2.3. It follows that the superfluid droplets exhibit the same shapes as classical droplets, while the previously reported extremely oblate shapes [12, 15] are not observed. Finally, possible implications of this finding for the superfluid phase transition are examined.

4.2.1 Classification of Static Diffraction Patterns

The diffraction patterns were recorded up to large scattering angles, therefore each image contains three-dimensional information on the particle shape and orientation. In particular, this leads to pronounced asymmetries in the pattern (cf. Sec. 2.4.3). Depending on their angular momentum the helium nanodroplets exhibit various deformations. In conjunction with each droplet's arbitrary orientation this leads to a great variety of features that can be observed in the scattering images. In order to be able to connect these features to certain droplet shapes, it is important to understand their origin. It is instructive to study the patterns that would result from light scattering on the shapes of rotating droplets discussed in Sec. 2.3, namely, spherical, oblate, and prolate shapes. For a sphere, the diffraction pattern consists of concentric circles, i.e., a ring pattern similar to the Fourier transform of a pinhole. The fringe spacing is connected to the size of the scattering object, i.e., for a given detection geometry, the larger the droplet the more rings can be seen in its scattering image. For oblate and prolate deformations of the droplet, the characteristic features in the wide-angle diffraction pattern are summarized in Fig. 4.7. In general, the shape of an oblate spheroid or a prolate ellipsoid can be described by its principal semiaxes a, b, and c, where we arbitrarily choose $a \geq b \geq c$ with c being the droplet's rotational axis. We choose a coordinate system where the unit vectors $\hat{x}$ and $\hat{y}$ define the scattering plane and $\hat{z}$ defines the optical axis. Any given orientation of the droplet can then be described by two tilt angles: the angle α describing a rotation around the y-axis [i.e., $\alpha = \angle(\hat{x}, \hat{a})$], and the angle γ describing a rotation around the droplet's long principal semiaxis a [i.e., $\gamma = \angle(\hat{y}, \hat{c})$]. A rotation of the droplet around the optical axis $\hat{z}$ will only rotate the diffraction pattern. Fig. 4.7 (a) shows a biaxial (i.e., $a = b > c$) oblate droplet that is not tilted with respect to the scattering plane (i.e., $\alpha = 0$, $\gamma = 0$). This results in a diffraction pattern exhibiting elliptic rings as the fringe spacing in direction of the dotted line is determined by the short semiaxis c and in perpendicular direction by the long semiaxis $a = b$. Tilting the short semiaxis c out of the scattering plane by γ [Fig. 4.7 (b)] introduces a characteristic one-sided asymmetry of the ring spacing in the diffraction pattern as can be observed along the dotted line (from the center of the diffraction pattern, there are three maxima in the upper half and four maxima in the lower half). This asymmetry occurs because

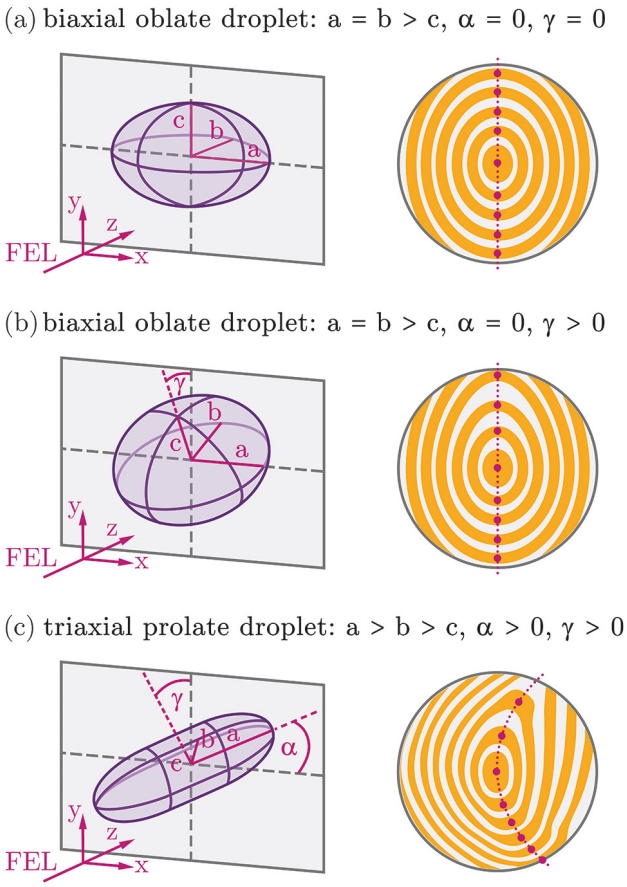

FIG. 4.7: Origin of characteristic features in the wide-angle diffraction patterns. The droplet is defined by its principal semiaxes a, b, and c and the two tilt angles α (rotation around the y-axis) and γ (rotation around the droplet's long principal semiaxis a). (a) The diffraction pattern of a biaxial oblate droplet ($a = b > c$) that is not tilted exhibits elliptical rings. (b) A tilt of the droplet's short principal semiaxis c out of the scattering plane (i.e., $\gamma > 0$) leads to a pronounced asymmetry in the diffraction pattern's ring spacing: From the center of the pattern, there are three maxima towards the top and four maxima towards the bottom (indicated by dots). (c) A triaxial prolate droplet ($a > b > c$) that is tilted out of the scattering plane. The tilt angle $\gamma > 0$ leads to an asymmetry in the diffraction pattern (cf. the number of dots in the upper half vs. the lower half) while the tilt angle $\alpha > 0$ introduces a characteristic bending (cf. the dashed line), that is only apparent in the case of prolate droplets.

the fringe spacing to the top is dominated by the length of c while to the bottom it is dominated by the length of b. It will therefore be largest for $\gamma = 45°$. Please note that the described asymmetry is a direct consequence of the wide-angle scattering and can not be observed for small scattering angles: The diffraction pattern of a tilted oblate droplet in the small-angle scattering regime exhibits elliptical rings similar to the pattern shown in Fig. 4.7 (a), but with a smaller ellipticity as the aspect ratio of the particle's projection decreases the more the particle is tilted. Finally, in Fig. 4.7 (c), a triaxial (i.e., $a > b > c$) prolate droplet is shown with $\gamma > 0$ and also $\alpha > 0$. Tilting the long principal semiaxis a by α introduces a bending of the diffraction pattern (see dotted line), while the tilt of the short principal semiaxis c leads again to an asymmetry of the fringe spacing (two maxima in the upper and five maxima in the lower half). The bending is a clear and easily detectable indication for a prolate shape that can not be observed in small-angle scattering images. Furthermore, the projections of an oblate and a prolate particle can be indistinguishable for certain orientations thus leading to small-angle diffraction patterns showing identical, centrosymmetric features. It is important to note that asymmetry and bending will only be observed in wide-angle scattering images. They are the key to accurately retrieve all three axes and the orientation of a droplet from a single diffraction pattern.

In Fig. 4.8, a selection of processed scattering images taken at various FEL wavelengths is shown. Each row depicts a certain feature getting more and more pronounced from left to right. In Fig. 4.8 (a), scattering images exhibiting concentric circles are shown with a decreasing fringe spacing (i.e., an increasing number of rings because of an increasing droplet size) from left to right. The vast majority of the scattering images belongs to this class that can be attributed to spherical droplets. The patterns of the remaining images exhibit various deformations. For example, scattering images with elliptical rings are shown in Fig. 4.8 (b), with an increasing ellipticity. As well as the images in the first category, these images possess point symmetry. Only a small fraction of the data exhibits *non*centrosymmetric features. In Fig. 4.8 (c) elliptical patterns are shown that have a one-sided asymmetry as it would be expected for a tilted oblate particle [cf. Fig. 4.7 (b)]. From left to right, the asymmetry is increasing due to the increasing tilt of the droplet's short principal axis by γ. In Fig. 4.8 (d), scattering images are shown with elliptical rings that exhibit a bending (i.e., $\alpha > 0$, $\gamma = 0$), while in Fig. 4.8 (e) an additional asymmetry can be observed [i.e., $\alpha > 0$, $\gamma > 0$, cf. Fig. 4.7 (c)]. Because of the bending, these images *must* depict prolate droplets. Finally, the scattering images shown in Fig. 4.8 (f) exhibit a pronounced *streak* that is due to the extreme aspect ratio of prolate, *pill-shaped* droplets ($a \gg b \sim c$). With an increasing tilt of the long principal axis out of the scattering plane, the bending of the streak increases. Asymmetries are less pronounced, as the b and c axes are of similar length. Please note that the scattering images shown in Figs. 4.8 (b)–(c) could also be produced by prolate droplets in a specific orientation. Nevertheless, it is reasonable to assign these images to oblate droplets: (i) Most of the droplets are almost spherical which lets one assume that overall, the droplets possess no or only small angular momentum. It is likely that oblate droplets occur more often than prolate droplets, where larger angular momentum is needed. (ii) The probability to image a prolate droplet in an orientation that no bending can be observed is comparably low. In summary, it follows that for a unique shape determination, asymmetries and bending in the diffraction patterns can be utilized to fix the orientation and lengths of the droplet axes.

Therefore, it is important to identify all scattering images in the data set exhibiting

(a) Concentric circles

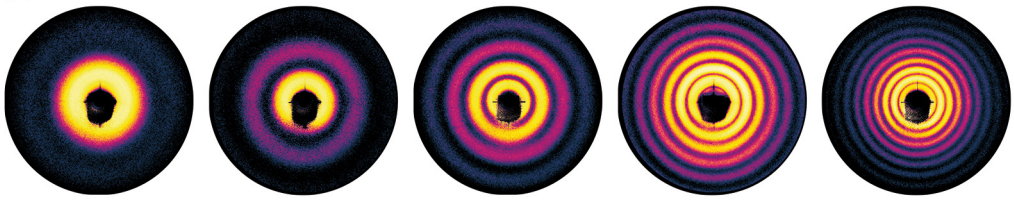

(b) Elliptic rings

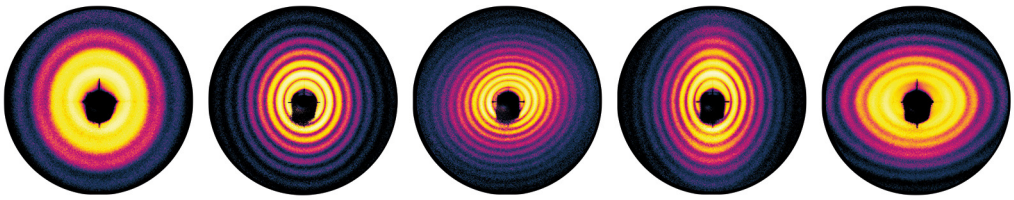

(c) Elliptic rings, asymmetric

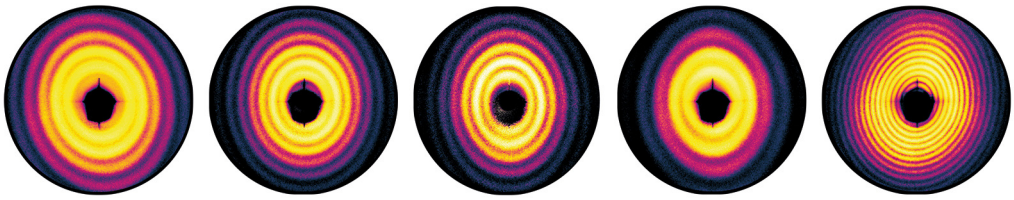

(d) Elliptic rings, bent

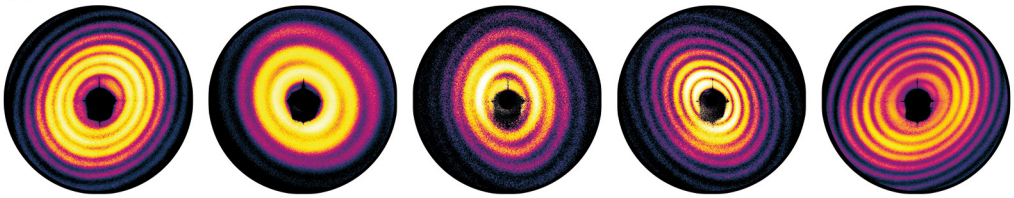

(e) Elliptic rings, asymmetric, bent

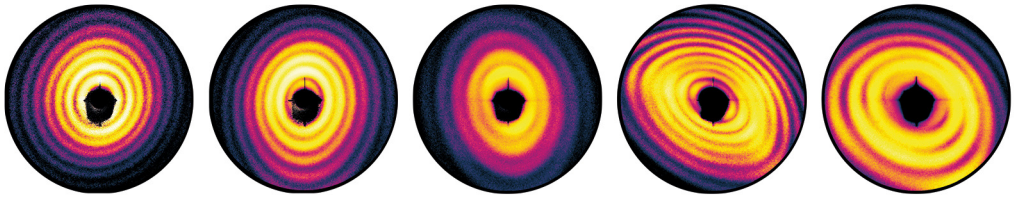

(f) Streaks

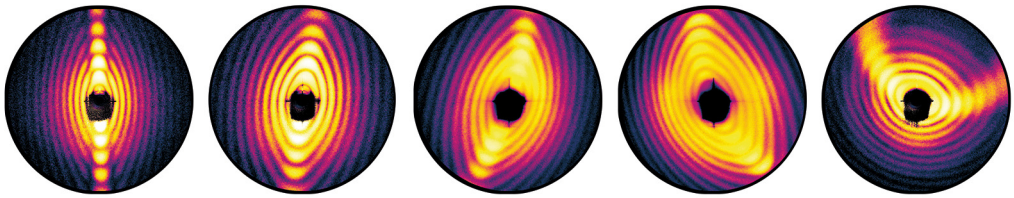

FIG. 4.8: Overview and classification of characteristic features in scattering images. (a) Concentric circles, with decreasing fringe spacing. (b) Elliptic rings, with increasing ellipticity [cf. Fig. 4.7 (a)]. (c) Elliptic rings exhibiting increasing asymmetries [cf. Fig. 4.7 (b)]. (d) Elliptic rings, showing a more and more pronounced bending. (e) Elliptic rings, with increasing asymmetry and bending [cf. Fig. 4.7 (c)]. (f) Patterns showing *streaks*, with increasing bending.

TABLE 4.6: Classification of the data set. A neural network [219] was used to automatically assign the three exclusive main classes (spherical, oblate, prolate) to the scattering images. All 38 150 images of the data set were analyzed. A mere 2.6 % of the images show noncentrosymmetric (i.e., asymmetric or bent) features and only 0.6 % of the images exhibit streaks, which are nonexclusive classes: Asymmetric patterns can belong to the oblate as well as to the prolate class while a bending or streaks indicate prolate shapes.

Class	No. of images	(%)
Spherical	35 457	92.9
Oblate	2139	5.6
Prolate	554	1.5
Asymmetric	533	1.4
Bent	464	1.2
Streaks	242	0.6

noncentrosymmetric features, which can be a problem given that typically FEL experiments produce large amounts of data. For example, in the present experiment 38 150 scattering images need to be classified, which makes an automated approach advantageous. However, this is a complicated problem due to the high dimensionality of the scattering data. Nevertheless, recent developments in automated pattern recognition using neural networks enable such an approach. In a collaboration with Julian Zimmermann the whole data set was classified using a deep neural network that is described in detail in Ref. [219]. In short, a sub set of the data containing 6829 images was manually labeled according to the features presented in Fig. 4.8. A major part (85 %) of this sub set was used to train a neural network especially designed for scattering data, while the remaining part was used for evaluation. The trained network was able to classify the evaluation data set with an accuracy of 96.2 %. The results of the subsequent automated pattern recognition procedure are summarized in Tab. 4.6. The scattering images were labeled for the three main shape groups: (i) Spherical [92.9 %, cf. Fig. 4.8 (a)], (ii) oblate [5.6 %, cf. Figs. 4.8 (b)–(c)], and (iii) prolate [1.5 %, cf. Figs. 4.8 (d)–(f)]. Additionally, all images exhibiting noncentrosymmetric features (i.e., asymmetric and/or bent patterns, 2.6 %) were identified as well as all images showing pronounced streaks (0.6 %) and manually checked after classification. The labeled data set for training and evaluation of the neural network has been made openly available at the Coherent X-ray Imaging Data Bank (CXIDB ID 94, see Ref. [220]).

4.2.2 Three-Dimensional Shape Determination

When it comes to the shape determination of individual nanoparticles using light scattering, several challenges need to be overcome. Ideally, the nanoparticles are not bound to a substrate or embedded in a matrix to be free from interactions with their surroundings that might influence the shape and the structure of the particles. In the case of free-flying particles, their structure has to be captured in a single exposure. Therefore, a light field is needed that is strong enough to generate a detectable scattering signal. To resolve the shape of the particle, the wavelength of the incident light has to

be smaller than the particle under investigation, i.e., in the XUV or x-ray regime. In an optical microscope, the far-field of the light diffracted at the sample is transformed into a real image using a lens. However, classical optics such as lenses are in general not available for XUV and shorter wavelengths. These issues are addressed by a method called *coherent diffraction imaging* (CDI). This lensless imaging technique enables using single-shot scattering images to reconstruct the shapes of free-flying nanometer-sized particles. A comprehensive overview on reconstruction methods for different wavelength regimes is given in Ref. [221]. Typically, when using x-rays the scattered light can only be detected up to small scattering angles (i.e., $\theta < 5°$) while when using XUV light, also signal at larger scattering angles can be accessed. In the case of hard x-ray small-angle scattering, iterative phase retrieval algorithms can be used to reconstruct the projected electron density of the particle from the scattering image [10, 222, 223] resulting in a two-dimensional image of the shape outline. In contrast, for wide-angle scattering images, there is so far no phase retrieval algorithm available that can reconstruct the particle shape from the diffraction pattern. Alternatively, a forward-fitting approach can be employed [13]: For a given model shape, the diffraction pattern is simulated and compared to the experimental data. Then, by altering the model shape, the simulated pattern is subsequently changed until a good match with the recorded pattern is reached. However, this approach needs (i) a reasonable physical model for possible shapes of the system under investigation (e.g., platonic solids for metal clusters), (ii) a sufficiently fast algorithm to compute the scattered field of the model shape, and (iii) a feature-based fit algorithm. One should keep in mind that the best fit resulting from this approach can only be as good as the shape model and need not be a unique solution. Nevertheless, this method has proven to be able to retrieve three-dimensional (3D) information on a particle from a single wide-angle scattering image. However, although a 3D characterization of the particle shape is always desirable, it has to be noted that using longer wavelengths to access large scattering angles comes with a loss of the high resolution x-rays provide. In this work, a variety of particle shapes is addressed that would be indistinguishable from their 2D outline, which particularly applies to extremely oblate and prolate droplets. While the former shape is thought to be a direct demonstration of the quantum nature of a spinning superfluid drop, the latter can be explained by a purely classical configuration. The question which equilibrium shapes superfluid helium nanodroplets exhibit is therefore an ideal case to employ the wide-angle scattering method.

In the following, the model for the shapes of rotating droplets, the algorithm for the simulation of wide-angle diffraction patterns, and the fit algorithm matching the simulation to the experimental data will be explained. The method for simulating the diffraction patterns was initially developed to analyze wide-angle scattering images of metal clusters (cf. Ref. [13]) and was applied to rotating droplet shapes in the present work. In particular, the computer code for the simulation and fitting routines used in this thesis was written by K. Sander and C. Peltz from the group of T. Fennel (Universität Rostock, Germany). As the fitting routine is very time-consuming, good initial values for the model shape were determined by manually optimizing the parameters for the simulated pattern to reproduce the features in the scattering image. Further, the fits were only performed for a sub set of the data: Scattering patterns exhibiting strong asymmetries were selected from the data set as these provide most information on axes lengths and particle orientation. This was one of the major tasks performed in this work, besides the identification and classification of characteristic features in the patterns and

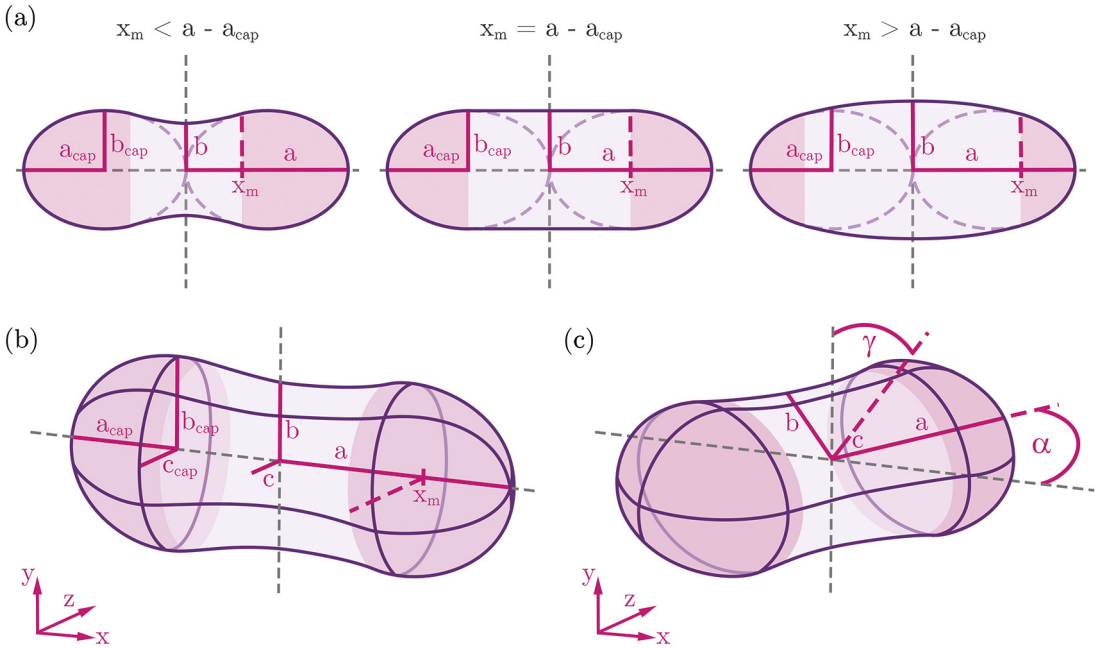

FIG. 4.9: Model for generating three-dimensional droplet shapes. (a) The model with the long principal semiaxis a is constructed of two identical ellipsoids with the principal semiaxes a_{cap}, b_{cap}, and c_{cap}. At the position x_{m}, the ellipsoids are cut and attached as caps (dark shading) to a hyperboloidal centerpiece (light shading). The curvature of the centerpiece is concave for $x_{\mathrm{m}} < a - a_{\mathrm{cap}}$, flat for $x_{\mathrm{m}} = a - a_{\mathrm{cap}}$, and convex for $x_{\mathrm{m}} > a - a_{\mathrm{cap}}$. (b) A triaxial, prolate model shape that is two-lobed, as $x_{\mathrm{m}} < a - a_{\mathrm{cap}}$. (c) The orientation of the model shape is defined by the angles $\alpha = \angle(\hat{x}, \hat{a})$ and $\gamma = \angle(\hat{y}, \hat{c})$, where $\hat{x}$, $\hat{y}$, $\hat{a}$, and $\hat{c}$ denote the unit vectors of the respective axes.

the connection of these features to shape properties (cf. Sec. 4.2.1).

For the simulation of diffraction patterns, a model for rotating droplet shapes was developed that can reproduce the shapes discussed in Sec. 2.3 without being strictly constrained to the equilibrium solutions for classically rotating drops. The model needs to be versatile enough to approximate spherical, spheroidal, ellipsoidal, pill-shaped, and dumbbell-shaped droplets. Therefore, a simple parametrized model was chosen that is shown in Fig. 4.9. In general, the shape is constructed of two identical ellipsoids (dark shaded) that are cut to serve as caps for a hyperboloidal centerpiece (light shaded), see Fig. 4.9 (a). The input parameters are the droplet's long principal semiaxis a, the semiaxes of the ellipsoidal caps a_{cap}, b_{cap}, c_{cap}, and the parameter x_{m} giving the position where the centerpiece and the caps are joined. The parameters for the hyperboloidal centerpiece are then determined in such a way that a smooth surface at the joining ($x = x_{\mathrm{m}}$) of the geometric bodies is maintained. Therefore, the parameter x_{m} dictates the curvature of the centerpiece: While for $x_{\mathrm{m}} > a - a_{\mathrm{cap}}$ the shape will be convex, for $x_{\mathrm{m}} < a - a_{\mathrm{cap}}$ it will be concave. Choosing x_{m} to be at the origin of the ellipsoidal caps, i.e., $x_{\mathrm{m}} = a - a_{\mathrm{cap}}$, will result in a pill shape. Note that it has to be $x_{\mathrm{m}} > a - 2a_{\mathrm{cap}}$ for the two ellipsoids to be connected. For the example shown in Fig. 4.9 (b) it can easily be seen that the model shape is concave, as $x_{\mathrm{m}} < a - a_{\mathrm{cap}}$. The lengths of the principal semiaxes b and c are retrieved at $x = 0$ in y and z direction, respectively. By definition, it is $a \geq b \geq c$. The coordinate system is defined by the optical axis of the incoming FEL which corresponds to the z-axis. A rotation of the model around the optical axis

will simply rotate the resulting diffraction pattern without changing its features. In Fig. 4.9 (c) the orientation of the model shape is exemplified. It is given by the angles α (rotation around y-axis) and γ (rotation around the shape's long principal semiaxis a). Please note that this is analog to the description of droplet orientation presented in Fig. 4.7.

The scattering of light at arbitrary objects can be described by solving Maxwell's equations. However, this is in general a complex and complicated task and also approximations come at a high computational cost. For example, the *discrete-dipole approximation* (DDA) algorithm [224, 225] describes the field for a set of point dipoles each interacting with the incident field and the scattered field of the other dipoles, it thus leads to an iterative computation of multiple scattering events. A computationally less expensive alternative is the *multi slice Fourier transform* (MSFT) method as described in Ref. [13] that is therefore used in this work. The basic idea is to approximate the diffraction pattern of a model shape by dividing the shape into slices and adding up the scattering patterns calculated for each slice. In particular, the droplet model shape is sampled onto a three-dimensional grid and the resulting density matrix is divided along the optical axis into multiple two-dimensional slices. For each slice of the density map, the scattering image in the far field is predicted by performing a two-dimensional Fourier transform. Summing up the scattering patterns of the single slices with consideration of the phase of the propagated wave gives the wide-angle diffraction pattern. However, this does not take into account absorption and refraction of the wave propagated through the particle. In order to include absorption, Lambert-Beer's law is implemented as an approximation: With a given effective absorption length, an exponential decay of the incident field during its propagation through the medium is assumed, reducing the scattering strength for each slice. The inclusion of refraction is particularly important when the real part of the refractive index deviates from unity (as is the case with liquid helium in the XUV regime, cf. Tab. 4.3). To account for the modified wavelength in the medium, the resulting phase slip is included in the algorithm by introducing a corresponding phase to the scattering strength. However, this simple model considers absorption and refraction only for the incident light field and not for the diffracted wave. Therefore, the *effective* phase slip δ_{eff} and absorption length ($\propto 1/\beta_{\text{eff}}$) values cannot be regarded as physically meaningful, as they differ from the actual optical parameters δ and β. They have to be determined separately, e.g., by matching diffraction pattern predictions to scattering images of spherical droplets that show no signs of detector saturation. Finally, the intensity distribution of the calculated patterns is adjusted to account for the scattering detector: As discussed in Sec. 3.2.2, the spatial sensitivity, nonlinearity, and saturation effects of the detector have to be considered. This is an important prerequisite for directly comparing the MSFT simulations with the experimental data, e.g., in an automated fit algorithm.

Starting with the manually pre-optimized model shapes, an automated fitting procedure was performed minimizing the deviation between the simulated and the measured scattering image. The fit algorithm is based on a Simplex [226, 227] Monte-Carlo approach optimizing the mean squared difference of the scattering patterns' logarithmized values for an ensemble of Simplex trajectories. As was pointed out before, the fitting procedure works best when the scattering images exhibit pronounced asymmetries caused by the different axes lengths of a tilted particle encoded in the diffraction pattern. Therefore, this approach is only feasible if the data set is large enough to contain a sufficient number of scattering images from optimally oriented particles (in

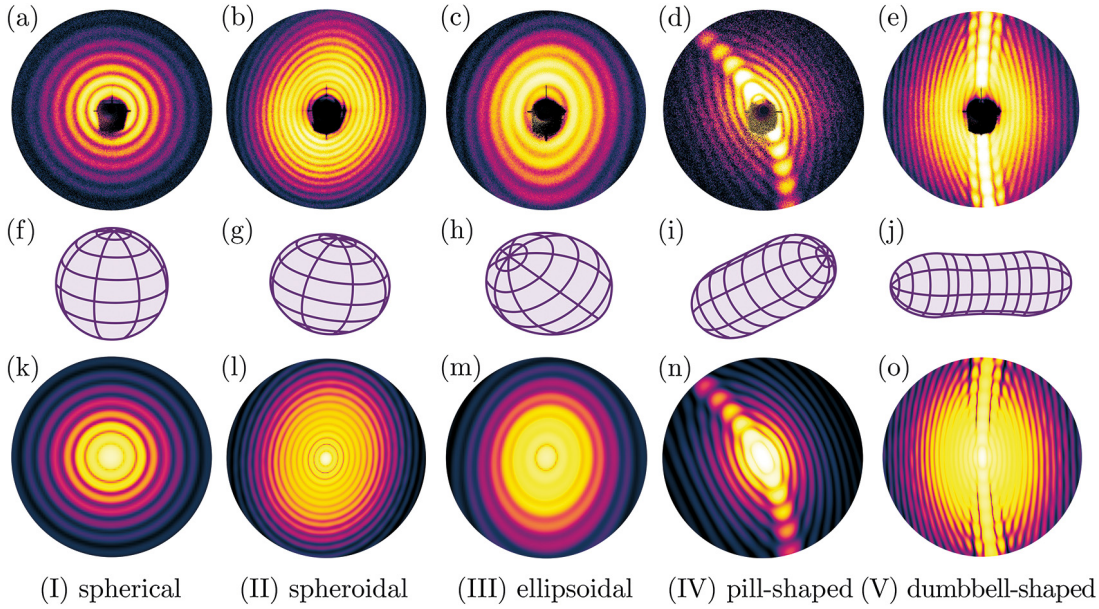

FIG. 4.10: Diffraction patterns of helium nanodroplets and corresponding shapes. Experimental data (a)-(e), retrieved model shapes (f)-(j), and matching MSFT simulations (k)-(o). The data can be classified into five groups (I)-(V), with a transition from spherical (f) to oblate (g) and prolate (h)-(j) shapes.

this case, $\gamma \sim 45°$). In the present work, 20 scattering images exhibiting the strongest asymmetry within their respective pattern class were selected from the data set for a systematic automated shape retrieval. The fit results can be found in Appendix B. In Fig. 4.10 examples for the five identified shape groups – (I) spherical, (II) spheroidal, (III) ellipsoidal, (IV) pill-shaped, and (V) dumbbell-shaped – are shown with the parameters for the depicted model shapes given in Tab. 4.7. Experimental data are presented in Figs. 4.10 (a)–(e), matching simulations in Figs. 4.10 (k)–(o), and the corresponding model shapes retrieved by the fit algorithm in Figs. 4.10 (f)–(j). It can clearly be seen that the simulated patterns reproduce the features of the scattering images and their intensity distribution very accurately. Please note that the color scaling of the simulations has been adjusted to resemble that of the experimental data. The characteristic features of the diffraction patterns presented in Fig. 4.8 can be easily identified, therefore demonstrating the connection between diffraction pattern class and droplet shape group: Concentric circles [Fig. 4.10 (a)] corresponding to a spherical droplet, asymmetric elliptical rings [Fig. 4.10 (b)] from an oblate shape, asymmetric bent rings [Fig. 4.10 (c)] inferring a prolate shape, and bent streaks [Fig. 4.10 (d)] from a pill-shaped droplet. In addition, the streaked pattern in Fig. 4.10 (e) exhibits side maxima that are due to the constriction of the dumbbell shape. The asymmetry of the fringe spacing along the streak in Figs. 4.10 (d)–(e) is not as pronounced as exemplified in Fig. 4.7 (c) since for pill-shaped and dumbbell-shaped droplets, $b \gtrsim c$.

As the spacing and the contours (i.e., asymmetries, bending) of the fringes in a diffraction pattern are very sensitive to a change of the model shape's axes lengths and orientation, the retrieved shapes reflect the geometry of the real droplets. With the droplets' dimensions (i.e., their principal semiaxes and volume) at hand, a comparison to theory is now feasible.

TABLE 4.7: Fit results for the model shapes shown in Figs. 4.10 (f)–(j).

shape	λ_{FEL} (nm)	a (nm)	b (nm)	c (nm)	V (nm^3)	a/c	b^3/V
(f)	57.6	483.0	475.8	468.6	4.59×10^8	1.03	0.23
(g)	59.0	978.2	963.4	820.9	3.26×10^9	1.19	0.27
(h)	65.0	612.6	529.9	410.4	5.63×10^8	1.49	0.26
(i)	52.3	747.3	332.5	306.4	3.85×10^8	2.44	0.10
(j)	60.4	1232.5	449.9	406.7	1.34×10^9	3.03	0.07

4.2.3 Discussion on Helium Nanodroplet Shapes

While extensive work on the shapes of rotating classical droplets is available [100, 102–108, 218], the shapes of spinning superfluid droplets have remained widely elusive (cf. Sec. 2.3). This is of course due to the experimental challenges connected with the study of fragile ultracold systems, especially when they are of small size, as it is the case for helium nanodroplets. During their formation process by expansion from the liquid phase, helium nanodroplets can gain angular momentum because of the liquid's interaction with the channel wall of the nozzle [112]. In general, angular momentum leads to a deformation of the droplets, and in particular, for superfluid droplets, to the formation of giant capillary waves or quantized vortices that store the rotational energy. In contrast to a normal liquid, a superfluid cannot rotate in the classical sense, i.e., with constant angular velocity. Therefore, the equilibrium shapes of superfluid droplets might differ from the shapes of classically rotating droplets. First scattering experiments on single helium nanodroplets reported extremely deformed oblate shapes with aspect ratios of up to $a/c = 1.92$ [12, 15], thus exceeding the stability limit for the equilibrium shape of an oblate normal liquid drop that is at $a/c = 1.5$. In addition, also prolate shapes were identified in later studies [15, 22]. However, the exact droplet geometry, i.e., the lengths of all three droplet axes, could not be retrieved. In my work, the three-dimensional shapes of spinning helium nanodroplets could be characterized for the first time in great detail, enabling to follow the shape evolution from spherical to oblate and prolate droplets. In Fig. 4.11 the retrieved helium nanodroplet shapes are compared to classical calculations. The dimensionless ratio b^3/V (V: droplet volume) is plotted versus the aspect ratio a/c. Data from this work (cf. Sec. 4.2.2) are shown as triangles. The dashed line is the analytical solution for the equilibrium shapes of oblate droplets [102] with the black circle denoting the stability limit for normal liquid droplets. The squares represent a numerical model [107] for rotating drops. It can clearly be seen that the droplet shapes follow the oblate branch up to an aspect ratio $a/c \approx 1.5$ and then evolve along the prolate branch: For $a/c > 1.8$ they become pill-shaped and for $a/c > 2.5$, the droplets exhibit dumbbell-like shapes. Surprisingly, this is not only true for the calculated shapes of normal liquid drops, but also for the shapes of superfluid helium nanodroplets – they seem to behave like their classical counterparts, with only slight deviations from the numerical model. In contrast to the pioneering works [12, 15] mentioned above, extremely oblate, "wheel-shaped" droplets with aspect ratios $a/c > 1.5$ are not observed. The occurrence of these classically unstable shapes was attributed to quantized vortices inside the superfluid stabilizing the droplet. These findings raise several questions that will be addressed in the following: (i) Are the observed helium nanodroplets in a superfluid state? (ii) If yes, do the droplets contain

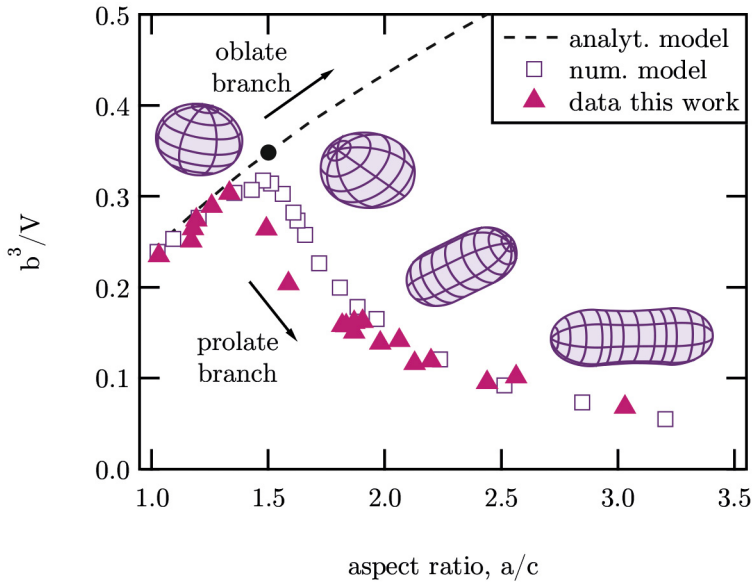

FIG. 4.11: Evolution of helium nanodroplet shapes and comparison to theory. The dimensionless ratio b^3/V is plotted versus the aspect ratio a/c. The retrieved shapes for superfluid helium nanodroplets (triangles) are compared to the equilibrium shapes of classically rotating drops: the analytical model for axisymmetric shapes (dashed line, cf. Ref. [102]) and the numerical model from Ref. [107]. The data from this work follow the oblate branch up to the classical limit of stability (indicated by the black circle) and then evolve along the prolate branch, with only slight deviations from the classical shapes.

quantized vortices? (iii) Why are there no extremely oblate, wheel-shaped droplets present?

Most experimental studies on helium nanodroplets relied on continuous sources expanding helium at low pressures around $p_0 = 20$ bar through a 5 µm sonic nozzle. Only a few studies were performed using pulsed sources [55, 56, 185, 228–230]. However, in all of the studies the produced ^{4}He droplets were assumed being superfluid as the cooling of the droplets by evaporation of helium atoms is a fundamental process keeping the droplets at a temperature of about 0.4 K [28, 29, 231]. There is no reason to believe the helium nanodroplets in the present work are at a higher temperature and therefore not superfluid.

In the pioneering CDI experiment on helium nanodroplets at the x-ray FEL Linac Coherent Light Source (LCLS) [12], extreme deformations of the droplets were observed and vortex arrays inside the droplets were made visible [12, 96, 223]. The deformations were attributed to the droplets picking up angular momentum during expansion from the liquid phase, which leads to the formation of vortices that accommodate the rotational energy. From the reconstructed shape outline, solely oblate droplet geometries were identified which were confirmed to be stable configurations for superfluid droplets containing vortices by density functional theory (DFT) calculations [113]. It is worth noting that for superfluid droplets vortex-free oblate configurations are not stable since their existence is quantum mechanically forbidden [232, 233]. A successive DFT study, triggered by the results from my work, additionally confirmed stable prolate configurations for superfluid droplets, with and without vortices [232]. In the latter case, angular momentum is stored exclusively in giant capillary waves. In Fig. 4.12

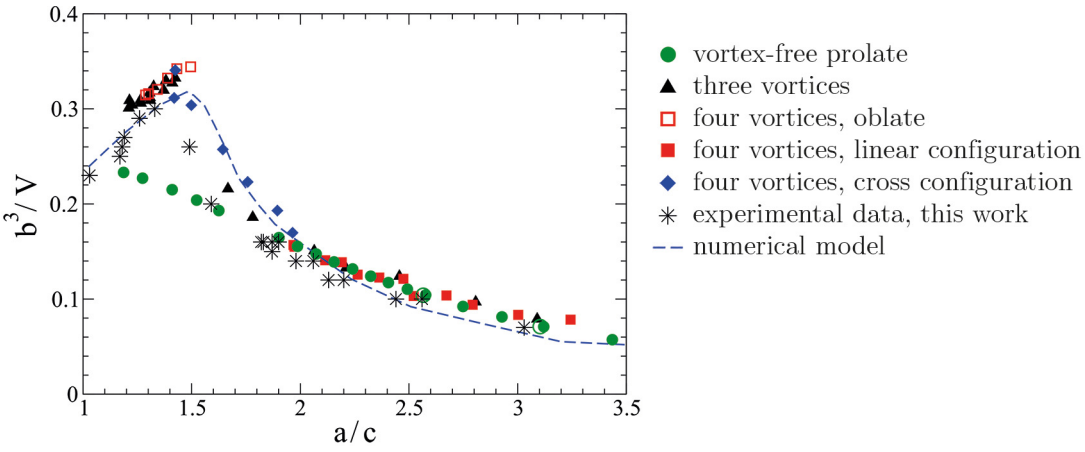

FIG. 4.12: Calculated shapes of spinning superfluid ^{4}He droplets in comparison with the experimental data from my work. Solid green circles: vortex-free prolate configurations. Black triangles, red squares, and blue diamonds: oblate and prolate configurations containing three or four vortices in different arrangements. Except for the vortex-free droplets the shapes are oblate for $a/c \lesssim 1.5$. Black starred symbols: data this work. Blue dashed line: Numerical model for normal liquid rotating drops from Ref. [107]. Adapted from Ref. [232].

the calculated ratios b^3/V and a/c are compared to the data from this work. The vortex-free prolate shapes are shown as solid green circles. The black triangles, red squares, and blue diamonds show oblate and prolate droplets containing three or four vortices in different arrangements. Except for the vortex-free droplets the shapes are oblate for aspect ratios $a/c \lesssim 1.5$; otherwise, they are prolate. The black starred symbols show the experimental data from this work and the blue dashed line shows the numerical model for normal liquid droplets from Ref. [107]. It follows that for aspect ratios $1.1 \lesssim a/c \lesssim 1.5$ the experimental data deviate from the vortex-free configuration while overall, there is a good agreement with the calculated droplet configurations containing vortices. Although further experimental proof is needed, this indicates that the observed prolate superfluid droplets indeed contain quantized vortices. In spite of irrotational flow being the main characteristic of the superfluid phase, the droplets take on the same shapes as normal liquid rotating droplets. While it has to be noted that small helium nanodroplets exhibiting identical shapes in normal liquid and superfluid phase do not possess equal angular momentum [232], recent results suggest that for large superfluid droplets the shapes closely resemble the classical shapes with the same angular momentum [97]. Therefore, this finding is reminiscent of an observation made in the 1950s: Bulk superfluid helium in a rotating bucket exhibits a parabola-like surface that was shown to be the same as for a normal liquid [94] – a behavior that is due to the presence of vortices in the superfluid.

In the articles by Gomez *et al.* [12] and Bernando *et al.* [15], extremely deformed, wheel-shaped droplets are reported. Their interpretation is based on the shape outline reconstructed from small-angle scattering patterns exhibiting streaks, while in Ref. [15] the radial intensity distribution of the reconstructed electron density was additionally analyzed and compared to calculated distributions corresponding to a variety of droplet shapes in different orientations. However, it is very difficult, if not impossible, to distinguish between a wheel-shaped and a pill-shaped droplet by looking at the outline of the reconstructed electron density. In the case of wide-angle scattering, this task

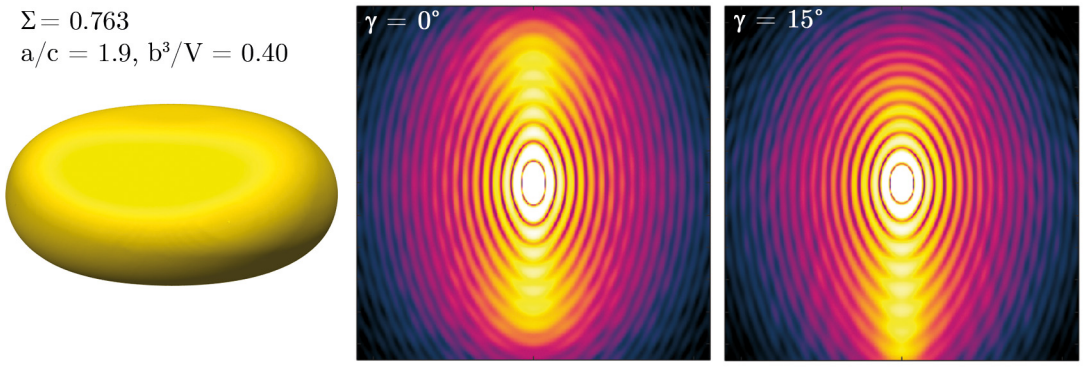

FIG. 4.13: Simulated wide-angle scattering patterns for a wheel-shaped droplet with $a = b = 1000\,\text{nm}$ and $\Sigma = 0.763$ (i.e., beyond the classical limit of instability, cf. Ref. [102]). The MSFT simulation was carried out for an XUV wavelength ($\lambda = 57.6\,\text{nm}$) with the appropriate effective optical parameters. When the droplet shape is not tilted (i.e., $\gamma = 0°$), a streak to both sides of the diffraction pattern can be observed, while for $\gamma = 15°$, a characteristic one-sided streak appears.

becomes much easier: An extremely oblate shape that is slightly tilted out of the scattering plane leads to a very obvious characteristic feature in the scattering pattern, a one-sided streak [22]. This is shown in Fig. 4.13 for an axisymmetric shape based on the analytical model by Chandrasekhar [102] with an aspect ratio $a/c = 1.9$, i.e., beyond the classical limit of instability. The aspect ratio was chosen to be the same as reported in Ref. [12]; however, the semi-major axis was set to $a = 1000\,\text{nm}$ as this is comparable to the axes lengths observed in this experiment. The simulation was carried out for an XUV wavelength ($\lambda = 57.6\,\text{nm}$) with the appropriate effective optical parameters (cf. Sec. 4.2.2). While for a non-tilted droplet ($\gamma = 0°$) the streak appears to both sides, for a slight tilt ($\gamma = 15°$) the streak develops only to the bottom side of the diffraction pattern. This pronounced asymmetry can be easily identified by eye. Nevertheless, in order to make sure that no scattering image from the data set exhibits a one-sided streak, all 38 150 images have to be checked. With the whole data set being classified by a neural network for automated pattern recognition (cf. Sec. 4.2.1), this can be reduced to the scattering images exhibiting asymmetries (in total, 533 images, see Tab. 4.6). As no diffraction pattern exhibiting this distinct feature can be found, it follows that the extremely oblate shapes are absent in this data set. This is a remarkable finding as it raises the question if the resulting shapes can be pushed beyond the classical stability limit, e.g., by the choice of expansion parameters. As was discussed before, the expansion of helium gas or liquid itself is believed to be a general process. The critical point of ^{4}He is at a temperature $T_c = 5.1953\,\text{K}$ and a pressure $p_c = 2.2746\,\text{bar}$ [47]. The expansion parameters of this experiment $T_0 = 5.4\,\text{K}$ and $p_0 = 80\,\text{bar}$ are higher, i.e., the helium is in a supercritical state. Nevertheless, as the density of the supercritical fluid $\rho_s = 196.93\,\text{kg}\,\text{m}^{-3}$ at 5.4 K is approximately the same as for the liquid $\rho_l = 197.83\,\text{kg}\,\text{m}^{-3}$ at 5.1 K [47], a liquid-like behavior is assumed already at the beginning of the expansion. From the cooling rates for helium nanodroplets [231] it can be expected that the liquid state as well as the superfluid state are reached while the expanding helium is still traversing the nozzle channel. Assuming that the droplets gain angular momentum because of the interaction with the channel walls, the nozzle geometry and the length of its expansion channel may influence the shapes of the forming droplets. While in this work a trumpet-shaped nozzle was used

with a channel length of 2.2 mm, in Refs. [12] and [15] a simple orifice with a channel length of only 2 µm was used. It could be that in the former case the transition from the normal liquid to the superfluid phase takes place inside the nozzle while in the latter case the droplets have already left the channel when turning superfluid – which could also affect the resulting droplet shapes. However, it is puzzling that in the work of Bernando *et al.* [15], both extremely oblate and prolate shapes were reported. This obviously raises the question why a portion of the droplets follows the oblate branch of the stability curve while at the same time a few droplets evolve along the prolate branch after the bifurcation point. Ultimately, this question will only be solved by performing a 3D sensitive experiment with the helium droplet source and conditions from Ref. [12].

Overall, these results nicely demonstrate how the wide-angle scattering method can add valuable information to the understanding of a nanometer-sized system. With the capability to gather 3D information on the particle in a single shot, it would be very interesting to combine this method with the high resolution x-ray CDI provides. Novel two-color schemes under development at FEL facilities [234] are a promising approach to simultaneously use an XUV pulse to record the 3D shape of a superfluid droplet and a (soft) x-ray pulse to resolve its vortex array structure. This would enable to clarify whether the predicted vortex-free prolate droplets exist or if the prolate droplets with high aspect ratios also contain vortices [232]. Also, the dynamics of the superfluid phase transition could be further explored to characterize the influence of the expansion parameters and different nozzle geometries on the formation of vortices inside the droplets. The ability to produce superfluid droplets free of vortices is a crucial technique to study the unhindered growth of nanoparticles inside an ultracold environment, as they would otherwise cluster along the vortex cores. An exact control of the formation process can therefore contribute to a new class of experiments: structure determination of large molecules embedded in helium nanodroplets at x-ray FELs, a path that was already laid out by the concept of *droplet coherent diffractive imaging* (DCDI) [223].

4.3 Light Induced Dynamics in Helium Nanodroplets

In the following, the light induced dynamics in helium nanodroplets will be discussed based on the scattering images taken of xenon doped helium nanodroplets after irradiation with a strong NIR laser pulse (i.e., the dynamic data set). In general, time resolved studies of nanometer-sized isolated samples are essential for understanding fundamental interactions of light with matter. In this context, short-wavelength FELs opened up a new route to observe ultrafast phenomena on small length scales and have been successfully employed to visualize structural changes in rare-gas clusters [124, 125, 235, 236], surface melting of metal clusters [237], and anisotropic evaporation of pristine helium nanodroplets [238]. As the NIR laser pulse deposits energy in the system that can not dissipate, the system will start to disintegrate. The xenon atoms in the droplet help to promote the ignition of a nanoplasma upon NIR irradiation [142, 145, 239]. In the simplest case, the xenon atoms form a cluster in the center of the droplet, i.e., the nanoplasma will also be ignited in the droplet center which presumably leads to an isotropic fragmentation of the droplet. However, theoretical work predicts that starting from a (small) xenon cluster inside a helium cluster ($N = 2 \times 10^4$ atoms), the nanoplasma propagates anisotropically along the polarization direction of the NIR laser field, thus forming a cigar-shaped plasma [142]. Given that the free electrons in the

plasma scatter less than the bound electrons, this could lead to a visible anisotropic signature in the scattering pattern subsequently recorded with the XUV pulse. On the other hand, experiments have shown that the xenon atoms agglomerate along the vortex cores instead of forming a compact cluster in the droplet center when vortices are present [12, 96]. In this case, the nanoplasma could be ignited at multiple sites in the droplet defined by the vortex array, probably leading to a complex fragmentation of the droplet. Therefore, it is an interesting prospect to study the fragmentation dynamics of superfluid droplets, especially when using a 3D sensitive technique.

In order to understand the dynamic data, the analysis of the scattering patterns and droplet shapes presented in the preceding Sec. 4.2 is an important prerequisite. In the course of this section the differences of the dynamic data set to the static data set will be explored to identify those features in the images that are due to the interaction with the NIR laser pulse – the so-called *dynamic* features. First, the scattering patterns will be classified based on their dynamic features. This is a challenging task as the images exhibit a much larger variety of features than in the static data set. After identifying several classes of dynamic scattering patterns, a conceivable connection to the underlying droplet density fluctuations is exemplified for two of the classes. Finally, a possible influence of the droplets' inner vortex structure on the observed dynamics is discussed.

4.3.1 Classification of Dynamic Diffraction Patterns

In this section, the characteristic features of the scattering images that are contained in the dynamic data set are described. In distinction to the static data set, the helium nanodroplets were doped with xenon atoms, irradiated with a strong NIR laser pulse (as a pump pulse) and imaged after a variable time delay Δt using an intense XUV light pulse (as a probe pulse). In Fig. 4.14 examples for scattering patterns from the dynamic data set are shown. As can be seen from Figs. 4.14 (a)–(c), the presence of dopants does not necessarily influence the diffraction patterns. These images exhibit the same features as were observed for pristine droplets in the static data set and will therefore be referred to in the following as *static* images. In particular, no difference to the static data can be observed for short time delays $\Delta t \leq 3\,\mathrm{ps}$. Still, this is a remarkably long time for nanometer-sized particles to exhibit no obvious changes. A change in the scattering patterns can only be seen for delays $\Delta t > 3\,\mathrm{ps}$: As is shown in Figs. 4.14 (d)–(f), the images then start to exhibit intensity fluctuations along the rings that can be identified as dynamic features in the data. Accordingly, diffraction patterns exhibiting such intensity fluctuations are referred to as *dynamic* images. The degree of these fluctuations varies from shot to shot, but in general increases for longer delays. However, up to the maximum delay that was set in this experiment ($\Delta t = 800\,\mathrm{ps}$), a considerable number of images does not exhibit dynamic features at all. In Fig. 4.15 the *dynamic fraction* of the scattering images is shown, i.e., the fraction of images that exhibit dynamic features is plotted for each delay Δt. The dynamic fraction is studied for different XUV photon energies ($E_{\mathrm{ph}} = 19.4\,\mathrm{eV}$, below resonance, and $E_{\mathrm{ph}} = 21.5\,\mathrm{eV}$, on resonance) and different doping levels (low, medium, and high). In general, there is an increase of the dynamic fraction during the first 100 ps to 150 ps after NIR irradiation. For longer delays, the dynamic fraction starts to saturate at 40 % to 80 % which means in turn that a significant fraction of the helium droplets is not affected by the NIR laser field (as a guide to the eye, limited growth functions were fitted to the data). This is a

surprising result, since in the design of the experiment it was taken care that when a scattering pattern of a droplet is recorded, the droplet was also hit by the NIR pulse before (cf. Sec. 3.2.1). Hence, this could be an indication for effective recombination processes in helium nanodroplets, or a nanoplasma ignition threshold for the droplets that was not reached for every shot with the present experimental parameters (both preventing the droplets from changing their equilibrium structure). On the other hand, the doping level seems not to influence the dynamic fraction. While a higher doping level should in general facilitate the nanoplasma ignition and therefore increase the dynamic fraction, no clear trend can be seen in Fig. 4.15: The data for low and high doping both exhibit a smaller maximum dynamic fraction than for medium doping. The change of the maximum dynamic fraction rather seems to be connected to the order of data recording, as it decreases with the time when the data were taken. The highest value is observed for the data taken at $E_{\mathrm{ph}} = 21.5\,\mathrm{eV}$, medium doping, which is the first data set in this sequence of measurements, while the lowest value is observed for the data taken at $E_{\mathrm{ph}} = 19.4\,\mathrm{eV}$, high doping, which was recorded last. This observation points at temporal drifts, e.g., in the performance of the droplet source (which showed a very stable operation with changes in temperature below 0.1 K within several days), or in the position of the pump and probe beam foci leading to a decreased spatio-temporal overlap that causes the dynamic fraction to drop. Also, a decrease in FEL intensity over time can lead to a seemingly smaller dynamic fraction, since smaller droplets that might exhibit a stronger response to the NIR laser pulse suddenly fall below the detection threshold. Additionally, the number of images recorded per data point is much lower for the high doping data resulting in a larger statistical error. Nevertheless, all curves equally show a steep increase followed by saturation. A similar behavior (i.e., not all diffraction patterns show signatures of precedent NIR irradiation) was observed in pump-probe scattering experiments with spherical SiO_2 nanoparticles [240] and metal clusters [241], indicating this effect might not depend on the system under investigation. There, it was speculated that this observation could be due to a certain threshold that needs to be overcome to induce dynamics in the particle – a condition that might not be met when the overlap of the pump and the probe beam is poor or in the case of an inhomogeneous focal spot of the NIR laser. Also, it could be that the pump laser power density is below the threshold while the probe laser power density is sufficient to generate a scattering signal when the particle is at the edge of the otherwise overlapping foci. However, in order to fully understand this observation, extensive studies are needed that systematically investigate the contributions of the different effects.

In the following, the dynamic images will be classified in the sense that prominent features in the patterns are identified and multiple images exhibiting similar features are assigned to categories. This approach to analyze the data set is based on the assumption that similar diffraction patterns are caused by similar structures. As was shown for the shape analysis in Sec. 4.2, fundamentally understanding the origins of the features in the diffraction patterns is crucial to successfully retrieve the droplet shapes. Nevertheless, in the case of the dynamic images, there is a much larger variety of features, rendering this approach much harder and much more time consuming. Therefore, the focus of this part of the thesis will be on how to address such a big data set of dynamic wide-angle scattering images and how to extract initial assumptions on possible model shapes from the data, rather than on a complete classification.

Figure 4.16 gives an overview on a selection of classes from which the first two will be investigated in more detail in Secs. 4.3.2 and 4.3.3. The first class, shown in Fig. 4.16 (a),

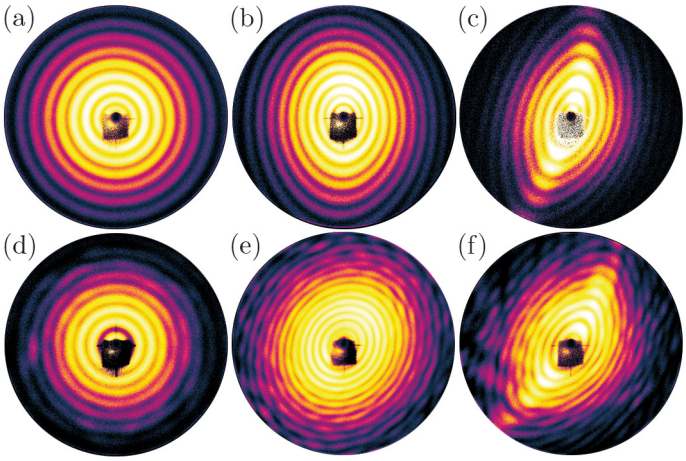

FIG. 4.14: Dynamic features in scattering images of xenon doped helium nanodroplets. (a)-(c) *Static* images. At short delays ($\Delta t \leq 3$ ps) the scattering images exhibit the same features as pristine droplets. (d)-(f) *Dynamic* images. For longer delays ($\Delta t > 3$ ps) the scattering images start to exhibit intensity variations along the rings.

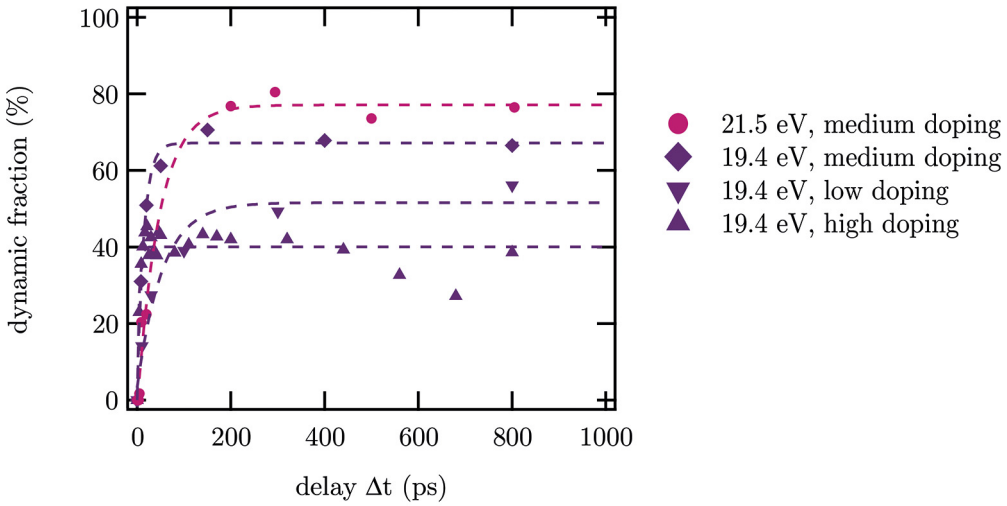

FIG. 4.15: Fraction of images exhibiting dynamic features. The dashed lines are limited growth functions as a guide to the eye. For all curves, the dynamic fraction shows a steep increase within the first 100 ps to 150 ps after NIR irradiation and then saturates. While the fraction of images showing no dynamics does not depend on the doping level, however, it increases with the time the data were recorded.

comprises images exhibiting speckle structures in different sizes. The patterns shown in Fig. 4.16 (b) were named "spider" patterns due to (multiple) pairs of "legs" sticking out either to opposing sides of the pattern or, in a more asymmetric version, to only one side of the pattern. In Fig. 4.16 (c), images are shown exhibiting polygonal structures, i.e., bright spots defining the corners of a polygon. The images in Fig. 4.16 (d) show cross-like patterns in various arrangements. The patterns in Fig. 4.16 (e) exhibit mirror symmetry and induce perceptions of object shapes such as a butterfly, the face of a seal, the greek letter Φ, etc., a phenomenon that is called *pareidolia*: falsely identifying shapes known to the observer in random objects. Finally, in Fig. 4.16 (f), some examples for complex patterns that do not fit in one of the categories mentioned before are shown. It is worth noting that using the classes presented here, the vast majority of the dynamic images has to be categorized as "diverse", since it is very difficult to identify similar features given the sheer size of the data set and the variations of the patterns. Further, it was not possible to extract a clear temporal order from the patterns, i.e., the occurrence of scattering images belonging to one of the classes is not obviously linked to the temporal delay Δt. Although there seems to be a tendency that less complex patterns (e.g., speckle and "spider" patterns) are prevalent at short delays while more complex (e.g., mirror symmetric) patterns are prevalent at long delays, this observation is to no extent exclusive (meaning that individual representatives of those categories can be found at all delays).

The classification of the patterns is the basis for a further analysis of the images. As it has been demonstrated by Barke *et al.* [13] and successfully applied to the static data set in Sec. 4.2, identifying categories for the images helps to develop a generalized model that can explain the various features observed in the patterns. Simulating patterns for different orientations and finding equivalent scattering images that add to a specific category will further improve the understanding of the model and finally lead to an extension of the model to explain also the remaining patterns in an iterative process. The dynamic data set, although being much more complex regarding the variety of features in the patterns, is approached in the same way. While it is not within the scope of this work to establish a generalized model that can explain all of the scattering images in the dynamic data set, shape models for two of the identified classes are developed, as a starting point, to provide a first insight into the fragmentation dynamics of xenon doped helium nanodroplets. In the following sections, the speckle patterns [Fig. 4.16 (a)] and the "spider" patterns [Fig. 4.16 (b)] will be analyzed in more detail, thus demonstrating the usefulness of the classification approach and how it can be extended to the remaining diffraction patterns in the future.

4.3.2 Randomly Distributed Fluctuations (Speckle Patterns)

In this section, the origin of the speckle patterns is discussed. Since the intensity fluctuations (i.e., the speckles) are distributed randomly across the patterns, it is likely that the underlying process also follows a random distribution. Diffraction patterns exhibiting speckles have already been observed in a pump-probe experiment on xenon clusters at the FLASH FEL [125] that were attributed to an expansion of the cluster accompanied by density fluctuations. Accordingly, let us assume a sphere with fluctuating density. This simple model can be easily realized: Starting with the *voxel* (volume element) representation of the model sphere described in Sec. 4.2.2, a fluctuating density can be simulated by randomly placing bubbles inside the sphere, i.e., introducing

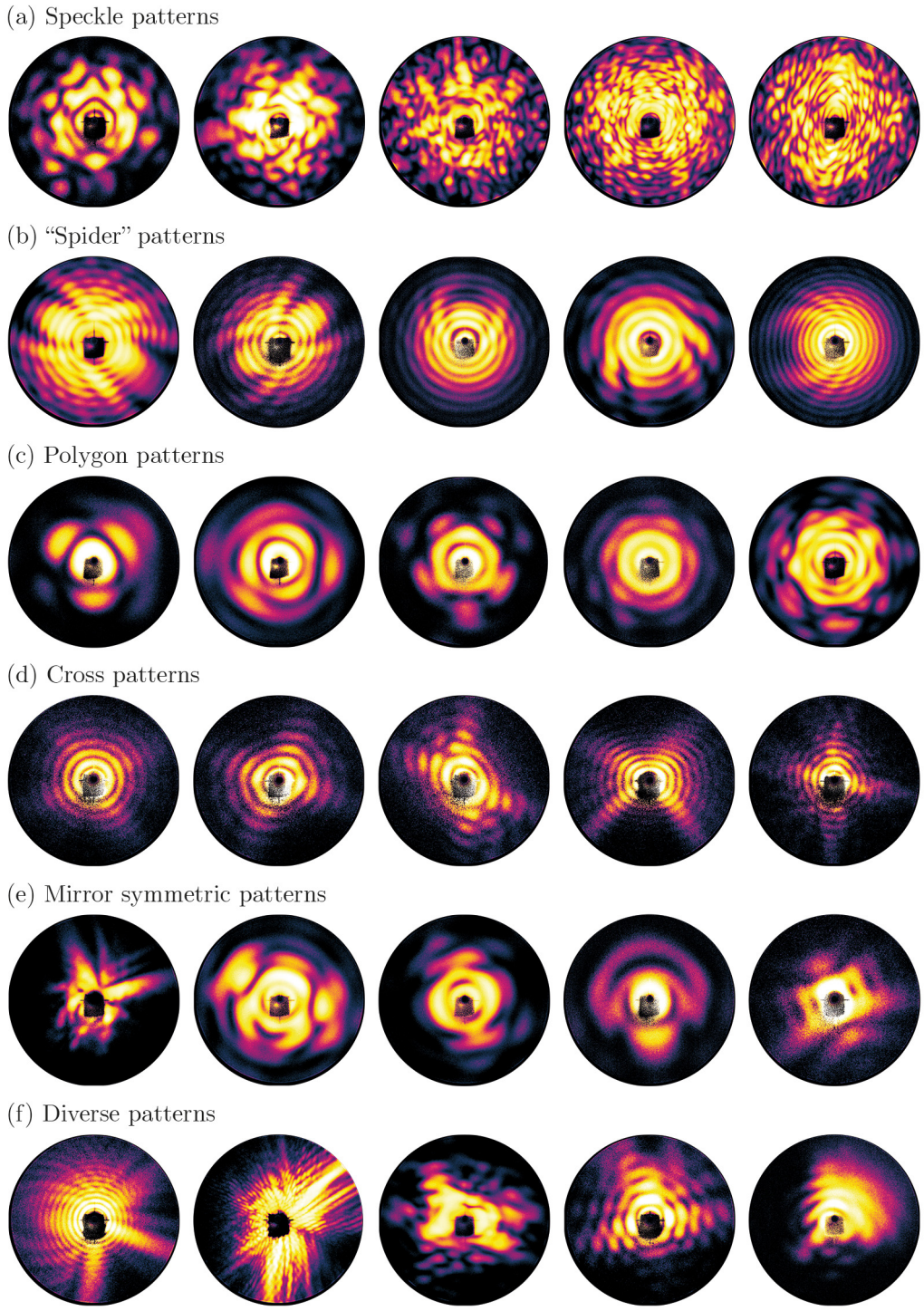

FIG. 4.16: Classification of scattering patterns exhibiting dynamics. The images were manually categorized based on their features. For details see text.

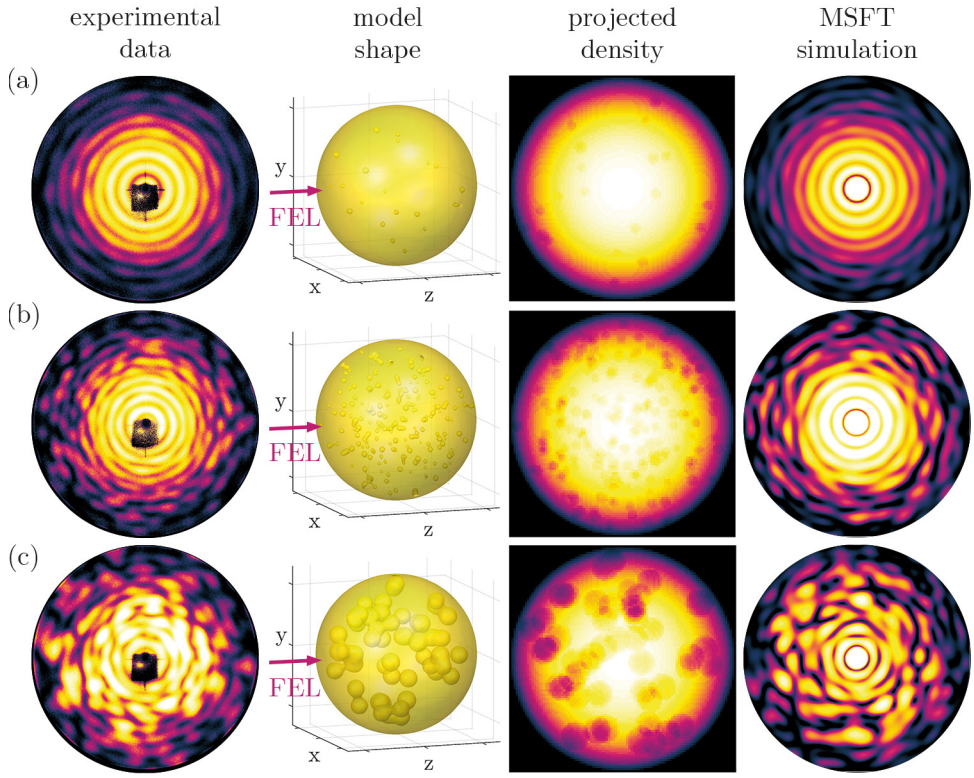

FIG. 4.17: Speckle patterns recorded at a photon energy of $E_{\mathrm{ph}} = 19.4\,\mathrm{eV}$ (i.e., off resonance) indicating randomly distributed density fluctuations inside the xenon doped helium droplet after NIR irradiation. Experimental data, the model shape, its projected density, and corresponding MSFT simulations are shown. The simulations qualitatively reproduce the main features of the experimental data that are determined by the droplet size as well as the number and size of the bubbles inside the droplet.

smaller spheres made up of voxels set to zero. The diffraction pattern of this diluted sphere can then be calculated using the MSFT algorithm described before. In Fig. 4.17, selected scattering images exhibiting speckle patterns are shown together with the model sphere, its density projection, and the corresponding MSFT simulation. The images were recorded at a photon energy $E_{\mathrm{ph}} = 19.4\,\mathrm{eV}$ (i.e., off resonance) and for the simulations, the corresponding effective optical parameters were used (cf. Sec. 4.2.2). In general, the features of the scattering patterns are well reproduced by the simulations. From Fig. 4.17 (a) it can be seen that for a slightly diluted sphere (i.e., a sphere containing a few small bubbles) the concentric ring pattern that would be expected for a solid sphere starts to dissolve. Beginning with the outer rings, intensity fluctuations can be observed while closer to the center of the image, the ring pattern remains intact. When the density of the sphere is further decreased by increasing the number of bubbles [Fig. 4.17 (b)], this trend becomes more obvious. An even lower density of the model sphere can be achieved when increasing the bubble size [Fig. 4.17 (c)]. In this case, almost the whole diffraction pattern consists of speckles. Please note that this simulation only gives an explanation for the evolution of the main features of the scattering pattern. Instead of trying to match the distribution of the speckles in the experimental pattern by exactly modeling the density distribution, the bubbles were placed randomly inside the model sphere to produce a rough resemblance of simulated to experimental data. Nevertheless, the simulations suggest that the speckle patterns are due to density fluctuations inside

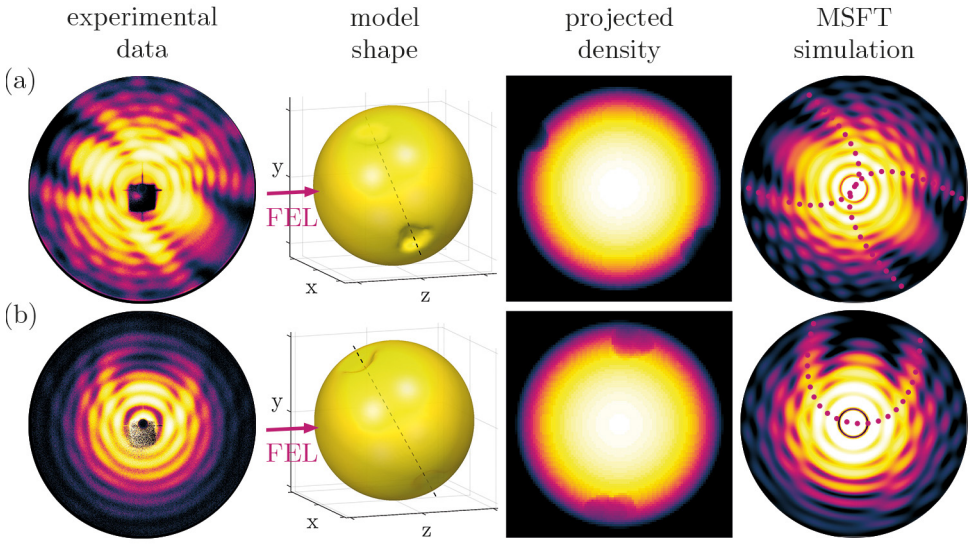

FIG. 4.18: "Spider" patterns recorded at a photon energy of $E_{\mathrm{ph}} = 19.4\,\mathrm{eV}$ (i.e., off resonance) indicating structured fluctuations of the droplet density. Experimental data, the model shape, its projected density, and the corresponding MSFT simulation are shown. The model shape consists of a sphere with multiple, overlapping bubbles placed at specific sites close to or at the droplet surface, thus forming two dimples penetrating the surface on opposite sides of the droplet. (a) The axis connecting the two dimples (dashed line) is perpendicular to the optical (FEL) axis. Both dimples contribute to the diffraction pattern leading to spider-like legs (dotted lines) on two sides of the pattern. (b) The axis connecting the two dimples (dashed line) is slightly tilted and not perpendicular to the optical (FEL) axis. Mostly the upper dimple contributes to the diffraction pattern, therefore the spider-like legs (dotted line) are only visible to one side of the pattern.

the helium nanodroplets.

4.3.3 Structured Fluctuations ("Spider" Patterns)

In the preceding section it was shown that scattering patterns exhibiting randomly distributed intensity fluctuations indicate randomly distributed fluctuations of the droplet density. However, most of the dynamic images show patterns with a pronounced anisotropic structure. Accordingly, this could be an indication for structured fluctuations of the droplet density. In the following, a possible explanation for the anisotropic intensity distribution will be presented for one of the anisotropic classes, the "spider" patterns. In Fig. 4.18, two examples of "spider" patterns recorded at a photon energy $E_{\mathrm{ph}} = 19.4\,\mathrm{eV}$ (i.e., off resonance) are shown together with the projected density of a shape model and the corresponding MSFT simulation. Images belonging to this category exhibit patterns with several pairs of streaks with increased intensity towards larger scattering angles, giving the impression of spider-like legs. They stick out to either two opposite sides [Fig. 4.18 (a)] or only one side [Fig. 4.18 (b)] of the pattern (cf. the dotted lines in the MSFT simulations shown in Fig. 4.18). The proposed shape model is that of a sphere with two small dimples on opposite sides. It is constructed by placing multiple, overlapping bubbles on or close to the droplet surface at specific sites, thus creating irregularities that penetrate the droplet surface on opposite sides. When the axis connecting these dimples is perpendicular to the optical axis [Fig. 4.18 (a)] the

diffraction pattern exhibits legs to *two* sides; when the axis is slightly tilted [Fig. 4.18 (b)], the legs show up only to *one* side. Again, the features observed in the experimental data are well reproduced by the simulated diffraction pattern, indicating that irregularities on the droplet surface are causing this kind of scattering images. However, since this forward-fitting procedure does not provide a unique solution for the model shape, several questions arise: Does the irregularity on the surface have to consist of two dimples or could it be, e.g., only one? Are the dimples necessarily facing each other or can they be randomly positioned on the surface? Or, instead of two dimples, could the patterns be caused by a channel traversing the particle from which we only see the entrance at the particle surface?

In order to address these questions, a series of simulations was performed exemplifying how different shape configurations influence the diffraction pattern. In general, the features in the pattern are caused by the particle shape and structure, its orientation, and its optical constants. Therefore, scattering images were not only simulated for several model shapes but also at different orientations as well as non-resonant and resonant photon energies ($E_{\mathrm{ph}} = 19.4\,\mathrm{eV}$ and $21.5\,\mathrm{eV}$, respectively). An overview of the main results is given in Fig. 4.19. The shapes consist of a sphere with radius $R = 580\,\mathrm{nm}$ and various irregularities introduced by placing multiple bubbles inside it. The irregularities are placed in vicinity of the model's central axis either at the surface of the sphere or distributed along the axis. A semi-transparent representation of the model is shown indicating the axis of the irregularities as a dashed line to better recognize the model's orientation. Further, the model's projected density is shown. As in all previous simulations, the FEL pulse propagates along the z-axis. The simulations were performed using the appropriate effective optical parameters for the two photon energies [cf. Sec. 4.2.2]. In Fig. 4.19 (a), the model with two dimples on opposite sides is shown when the orientation of the axis connecting the two dimples is perpendicular to the FEL axis. In this case, both dimples cause spider-like legs to two sides of the diffraction pattern. This corresponds to the scattering image in Fig. 4.18 (a). When the dimple axis is not perpendicular to the FEL axis but slightly tilted, as shown in Fig. 4.19 (b), the spider-like legs in the diffraction pattern are only bent towards one side. This is because only one dimple (in this case, the upper one) contributes to the diffraction pattern: During propagation through the medium, the FEL beam is absorbed and therefore does not "see" the second dimple on the back of the particle. The resulting pattern corresponds to the scattering image shown in Fig. 4.18 (b). However, similar diffraction patterns can be produced by different configurations: In Figs. 4.19 (c)–(d), calculations for a model shape with only one dimple instead of two are shown, first oriented perpendicular to the FEL axis [Fig. 4.19 (c)] and then slightly tilted [Fig. 4.19 (d)]. In both cases the diffraction patterns exhibit spider-like legs to only one side with almost no visible difference between the patterns in Fig. 4.19 (d) and Fig. 4.19 (b). This supports the assumption that in the case of a tilted sphere with two dimples, only the dimple on the front side of the droplet (i.e., the side facing the incoming FEL beam) contributes to the diffraction pattern. However, it is not possible to reproduce the scattering image shown in Fig. 4.18 (a) using a model shape with only one dimple. While this configuration can not be excluded for most droplet orientations, both types of "spider" images shown in Fig. 4.18 can be explained by a droplet with two dimples on opposite sides. Further, another configuration can be expected to produce similar results: Given a sufficient strong absorption, a channel-like structure traversing the whole particle can be expected to have the same influence on

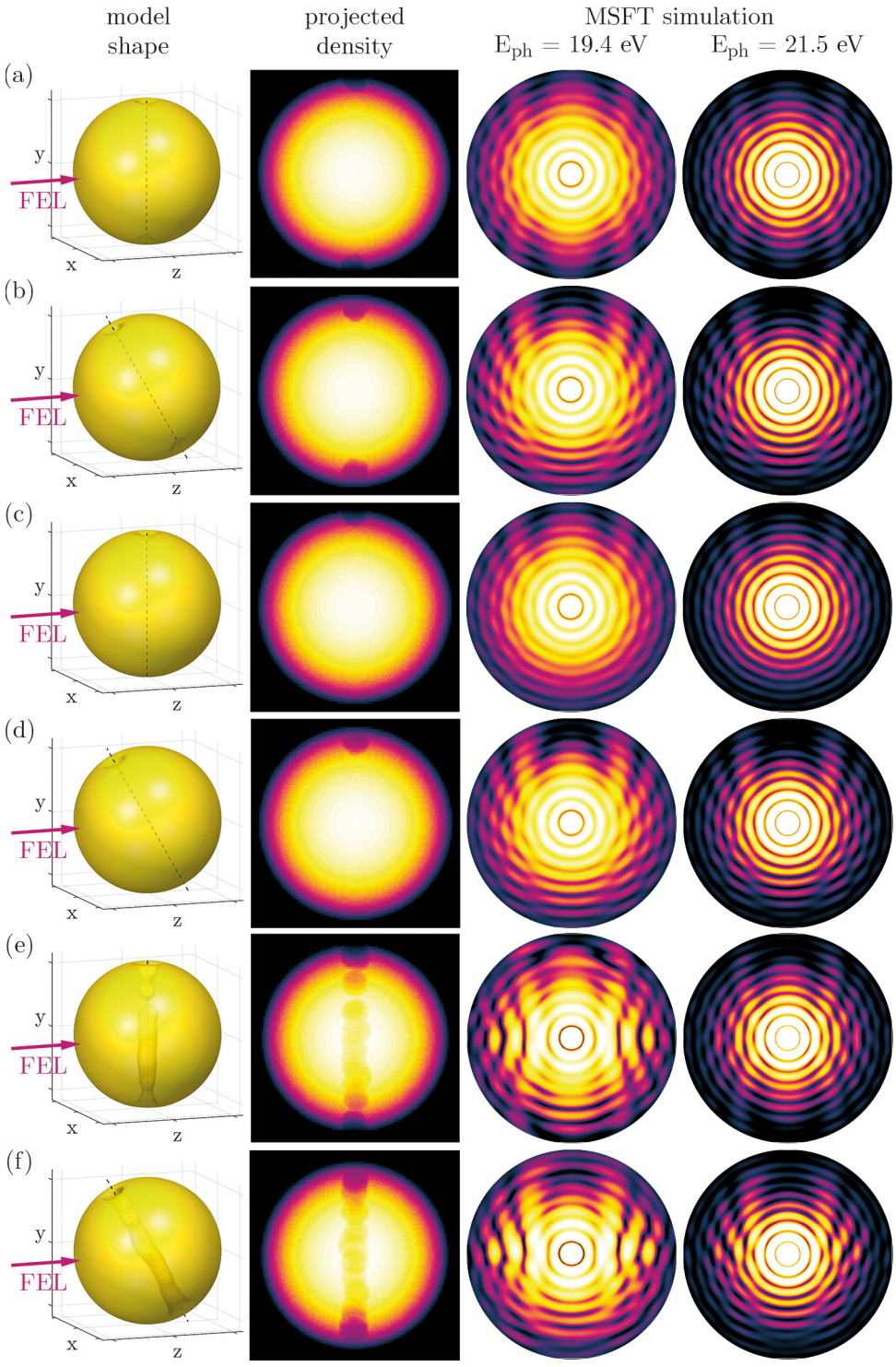

FIG. 4.19: Study of model shapes reproducing the anisotropic "spider" patterns. A three-dimensional representation of the model shape, its projected density and MSFT simulations for two different FEL photon energies, resonant and non-resonant ($E_{\mathrm{ph}} = 21.5\,\mathrm{eV}$ and $19.4\,\mathrm{eV}$, respectively), are shown. For details see text.

the diffraction pattern as two dimples, since only the surface of the particle adds to the scattering signal. This is shown in Figs. 4.19 (e)–(f) with the axis oriented perpendicular to the FEL beam and slightly tilted, respectively. It can be seen that for the resonant photon energy $E_{\mathrm{ph}} = 21.5\,\mathrm{eV}$, the resulting diffraction pattern in Fig. 4.19 (e) resembles the recorded image shown in Fig. 4.18 (a) while the pattern in Fig. 4.19 (f) resembles the recorded image shown in Fig. 4.18 (b). For this photon energy, the absorption length is significantly shorter than the radius of the particle and only the entrance of the channel adds to the diffraction pattern. However, the scattering images shown in Fig. 4.18 were recorded at a photon energy $E_{\mathrm{ph}} = 19.4\,\mathrm{eV}$, which is below the helium droplet resonance. Therefore, no absorption is expected, and a clear signature of the channel should be visible. This can be seen in the calculated diffraction patterns [Figs. 4.19 (e)–(f), MSFT simulation for $E_{\mathrm{ph}} = 19.4\,\mathrm{eV}$], but not in the experimental data [Figs. 4.18 (a)–(b), left panel]. Therefore, it can be excluded that a channel-like structure in the droplet caused the observed diffraction patterns – although it should be noted that the effective optical parameters used in the simulations were retrieved for solid spheres and might not fully apply for the models containing irregularities that are used here. Further, the current approach of placing bubbles inside the model shape to mimic density fluctuations is certainly a very rough one that needs to be refined for a higher accuracy in matching the simulations with the experimental data. Nevertheless, it could be shown that the scattering images in Fig. 4.18 are caused by structured irregularities on opposite sides of the droplet surface. This observation is a clear indication that irradiation with an NIR laser pulse triggers structured dynamics inside the droplet.

4.3.4 Discussion on the Influence of Doping on Droplet Dynamics

In this section, the influence of doping on the observed dynamics in helium nanodroplets is discussed. Doping the droplets with xenon atoms was instrumental to ignite a nanoplasma inside the droplets. Since the intensity of the NIR laser is not sufficient to ionize the helium atoms [127], the energy is mainly introduced into the system at the location of the xenon dopants. In contrast to previous time-resolved studies investigating homogeneous systems such as pure xenon clusters [124, 125], the ignition of the two-component system used in this work (i.e., xenon doped helium nanodroplets) can trigger randomly distributed fluctuations of the droplet denstiy, as it was shown in Sec. 4.3.2, as well as structured fluctuations at specific sites on the droplet surface, as it was shown in Sec. 4.3.3. In the following, possible reasons leading to this remarkable observation are presented.

Theory predicts that rare gas dopants form a cluster in the center of the helium nanodroplet [242]. In the case of a xenon core, irradiation with a strong NIR pulse efficiently turns the droplet into a nanoplasma [142]. In previous pump-probe CDI studies, speckle patterns have been observed for laser-excited clusters and attributed to density fluctuations caused by, e.g., a homogeneous expansion of xenon clusters [125] or formation of gas bubbles in silver clusters [237]. Such processes can in principle also be envisioned for helium nanodroplets, but should be further explored by theoretical work. On the other hand, it has been suggested before that xenon dopants can form clusters at multiple sites in a helium nanodroplet [243], based on a speckle pattern recorded during an x-ray CDI study from which the positions of the xenon atoms were determined by reconstructing the particle's electron density. Assuming such a distribution of xenon clusters in the droplet, a nanoplasma ignition or heating of the droplet at multiple sites

could also lead to the observed density fluctuations: Although the XUV pulse is not directly sensitive to the xenon atoms, turning the helium atoms in vicinity of the xenon dopants into a plasma would be accompanied by a local change of refractive index that could be visible in the diffraction pattern. Therefore, it would be certainly interesting to extend the theoretical studies on cluster formation of rare gas dopants in helium nanodroplets to the size range of the droplets investigated in recent CDI experiments.

The observation of structured density fluctuations raises the question why there are irregularities localized at specific sites on the droplet surface in the first place. Intuitively, one would not expect any structured behavior from a spherical superfluid droplet. However, anisotropic evaporation from a helium droplet has been reported before [238]. There, pristine helium nanodroplets (i.e., without any dopants inside the droplet) were investigated in a pump-probe setup using a strong ($\sim 4 \times 10^{15}\,\mathrm{W\,cm^{-2}}$) NIR laser for ionization and a subsequent x-ray FEL pulse to record a scattering pattern. While the diffraction patterns were showing concentric circles when both pulses arrived at the same time, they became more and more elliptic the longer the temporal delay was chosen. Further, the orientation of the semi-major axis in the pattern was connected to the polarization of the NIR laser. Also, for small helium droplets doped with a cluster of a few xenon atoms, a theoretical study predicted an anisotropic, "cigar"-shaped evolution of a nanoplasma upon NIR irradiation [142]. Again, the direction of the nanoplasma propagation was linked to the polarization of the incoming NIR laser beam. In contrast, the anisotropies observed in the "spider" patterns are obviously not connected to the polarization of the NIR laser: As can be seen from Fig. 4.16 (b), the orientation of the spider-like legs changes which means that the surface irregularities (cf. Sec. 4.3.3) are randomly oriented. Further, there are several other differences: (i) The power density of the NIR laser is about two orders of magnitude lower than in Ref. [238], which might induce fundamentally different processes. (ii) The number of xenon atoms embedded in the droplet is significantly higher and the droplet itself is significantly larger than in Ref. [142]. (iii) The droplets are in a size range where also the nearly spherical droplets presumably contain vortices. It has been shown before that dopants in a superfluid helium nanodroplet get trapped by [244] and align along the vortices [12, 112]. In the present experiment, the ignition of the nanoplasma in the droplet after NIR irradiation is promoted by the xenon dopants. Thus, it could be that the vortex structure of the droplet defines the ignition spots of the nanoplasma and therefore influences the subsequent dynamics. In the simplest case of a single central vortex in the droplet, the xenon atoms aligned along the vortex get ionized, and, as theory supports [242], ejected from the droplet. The xenon ions close to the surface, i.e., at the sites where the vortex intersects the droplet surface, will be the first leaving the droplet. In the course of this process, helium atoms will be ripped off the droplet's surface by the xenon ions, thus creating a dimple. Accordingly, the occurrence of "spider" patterns would mean that the beginning of a real change of the droplet surface is observed rather than mere density fluctuations. As the vortex traverses the whole droplet, two dimples develop on opposite sides of the droplet. In this sense, the dimples on the droplet surface could reveal the underlying vortex array.

The next step would be to extend this idea to multiple vortices. Vortex arrays in helium nanodroplets have been investigated in hard x-ray CDI experiments before [12, 96, 223]. There, xenon atoms have been used as contrast agents to reveal the vortex structure in the reconstructed images. For example, in the work of Jones *et al.* [96], the helium droplets were heavily doped with xenon and several vortex configurations

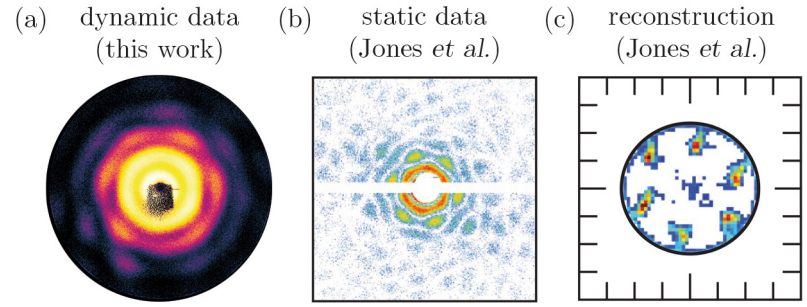

FIG. 4.20: Hints on vortex induced dynamics. A diffraction pattern from this work showing a hexagonal structure is compared to a pattern with similar features and the corresponding reconstruction from Jones *et al.* [96]. (a) Experimental data, this work. Wide-angle scattering image of a laser excited helium nanodroplet doped with xenon. (b),(c) Experimental data and corresponding reconstruction, respectively. Small-angle scattering image of a xenon doped helium nanodroplet without prior NIR irradiation. Adapted from Ref. [96].

could be identified. Interestingly, although this was not a time-resolved study, the hard x-ray diffraction patterns exhibit pronounced similarities to the polygon patterns [cf. Fig. 4.16 (c)]. This is a first indication that these patterns are also related to the droplet's vortex structure. In Fig. 4.20, a hexagon pattern from this work and a similar pattern with the corresponding reconstruction from the work of Jones *et al.* are shown. When looking at the features in both scattering images, their resemblance is intriguing. Although this can be just a coincidence, it renders the inclusion of more complex patterns of dimples on the model surface a promising approach for the further analysis of the dynamic data set.

As was already pointed out in Sec. 4.2.2, the method of forward-fitting model shapes to wide-angle scattering patterns to retrieve the real geometry of a particle is always limited by the quality of the model. Therefore, establishing a connection between the structure of the dopants in the droplet and the diffraction pattern is an important step to refine the model, which might ultimately lead to a complete understanding of the various features observed in the dynamic images. However, it could turn out that the categories found for the different images need to be revisited: So far, the classification was based on features in the images, while the next step has to include a classification based on shape parameters (e.g., oblate, prolate, number and arrangement of dopant clusters/vortices, etc.). As the analysis of the speckle and the "spider" patterns presented here has shown, the location of the dopants inside the droplets (that might be linked to the vortex structure) is important for the dynamics following irradiation with an NIR laser pulse. Therefore, molecular dynamics simulations taking into account multiple or structured dopant sites (i.e., multiple clusters or dopants aligned along vortices) could provide a deeper insight into the processes involved and elucidate their temporal evolution. In combination with the data from this work, several questions could be addressed: (i) What is the main process causing the observed density fluctuations? (ii) How do the fluctuations progress in the droplet, i.e., are they instantly distributed throughout the droplet or do they propagate from the droplet center to the surface? For example, a time resolved analysis of the occurrence of speckle patterns for resonant and non-resonant photon energies could enable a distinction between volume and surface effects in the droplets. (iii) Do the regions of reduced (or increased) density merge? For example, many of the strongly distorted patterns [such as the mirror symmetric

patterns, cf. Fig. 4.16 (e)] exhibit large dark areas and rather large, connected features without fine structure, which hints at a few large regions of fluctuating density in the droplets. Since these patterns predominantly occur at longer delay times, it could be that the initially large number of small irregularities develops into a fewer number of large irregularities. Further, mirror symmetric features in the diffraction patterns hint to mirror symmetric shapes. What causes the structure of the irregularities? (iv) What is the timescale of these processes? Since intense scattering patterns were recorded up to 800 ps (in contrast to previous work on xenon clusters where no more scattering signal was detected after 5 ps [124]), are there processes present that dampen the dynamics in the helium nanodroplets (e.g., is the helium shell acting as a sacrificial layer [24, 25]) and do they need to be included in future simulations?

Finally, I'd like to point out that while the manual classification of the dynamic images performed in this work is a good starting point for the analysis, it is also prone to misinterpretation. For example, the category of mirror symmetric images [cf. Fig. 4.16 (e)] contains images that induce the perception of a known shape or object – a phenomenon that reminds of *Rorschach patterns*, where the perception of shapes is caused by symmetry and fractal dimension [245]. Obviously, these images stand out of the data set and can easily be identified by the researcher. However, the corresponding droplet shapes and underlying dynamics might be completely different for the individual images. Also, the researcher might overlook images with seemingly chaotic patterns and miss important information. Therefore, it might be fruitful to approach the classification problem by employing a self-learning neural network that sorts the data set into categories free from human bias [219].

Chapter 5

Summary and Outlook

In this work, the morphology of superfluid helium nanodroplets has been studied in a scattering experiment utilizing intense extreme-ultraviolet (XUV) light pulses. In general, the analysis of the three-dimensional (3D) droplet structure is based on wide-angle scattering images of individual helium nanodroplets. The study can be divided in two parts: First, an investigation of the equilibrium droplet shapes using only the XUV pulse (static data), and second, an exploration of the dynamics induced in the droplets by irradiation with an intense near-infrared (NIR) light pulse in an NIR pump-XUV probe setup (dynamic data). While the results from the static data set gave answers regarding the 3D shapes of spinning superfluid droplets, the dynamic data set raised many questions that should be addressed by future experiments or enhanced analysis methods.

The experiments were performed at the low density matter (LDM) end-station at the FERMI FEL in Trieste, Italy. Resonant and non-resonant scattering at helium nanodroplets was enabled by tuning the FEL to photon energies ranging from 19.1 eV to 38.5 eV, with ultrashort pulses exceeding power densities of $3 \times 10^{14}\,\mathrm{W\,cm^{-2}}$. The NIR laser delivered pulses with a power density of $8 \times 10^{13}\,\mathrm{W\,cm^{-2}}$ with an adjustable delay between the NIR and FEL pulse that was varied from 0 ps to 800 ps. The helium nanodroplets were produced using a pulsed cluster source. The supersonic expansion of helium gas at a pressure $p_0 = 80\,\mathrm{bar}$ and a temperature $T_0 = 5.4\,\mathrm{K}$ resulted in a mean droplet size of $\langle N \rangle = 6 \times 10^9$ atoms per droplet. The size distribution was determined by fitting Mie profiles to scattering images of spherical droplets. The scattering images were recorded up to a maximum scattering angle $\theta_{\mathrm{max}} = 30°$.

While more than 90 % of the diffraction patterns exhibit concentric circles that can be attributed to spherical droplets, some of the patterns show pronounced asymmetries that arise when a deformed, non-spherical droplet is tilted with respect to the optical axis. In fact, the asymmetries in the pattern reflect the 3D information encoded in the wide-angle diffraction pattern and can therefore be used to accurately retrieve the droplet dimensions (all three principal axes and the droplet volume) as well as its orientation. This enables a complete reconstruction of the droplet shape and from the patterns exhibiting the strongest asymmetries, 20 were selected to cover the whole range of shape deformations. The shape retrieval method is based on an improved multi slice Fourier transform (MSFT) algorithm [13] developed by K. Sander and C. Peltz from the group of T. Fennel (Universität Rostock, Germany) that is used to simulate a diffraction pattern for a model shape and, by altering the model shape, match the

simulation to the recorded scattering image. For a better approximation of the simulated patterns to the experimental data, effective optical parameters were included in the algorithm. Finally, the reconstructed shapes were compared to theoretical models of rotating drops. While previous studies reported superfluid droplet shapes beyond the instability limit for normal liquid drops [12, 15], the occurrence of such "wheel-shaped" droplets could be excluded for the data in this work. This finding is based on the results of an automated classification of all scattering images using a neural network developed by J. Zimmermann [219]. Furthermore, it was shown that spinning superfluid helium nanodroplets exhibit the same shapes as normal liquid rotating drops: Spherical, spheroidal, ellipsoidal, pill-shaped, and dumbbell-shaped droplets were observed, with a transition from oblate to prolate shapes close to the classical instability limit for axisymmetric drops [102, 103, 107].

In the second part of this thesis, the light induced dynamics in helium nanodroplets were studied, i.e., after irradiation with a strong NIR laser pulse. The droplets were doped with xenon atoms to facilitate the ignition of a nanoplasma. Therefore, the energy deposition in the droplets is connected to the dopants and their positions. In consequence, a large variety of complex diffraction patterns is observed that were categorized based on their apparent features. The development of a shape model was exemplified for two classes, speckle patterns and "spider" patterns. In general, the deviations in the scattering images of the dynamic data set (as compared to the static data) can be attributed to density fluctuations in the droplets. In the case of the speckle patterns, the characteristic features can be reproduced by randomly placing bubbles in the model sphere and matched by varying the number, size, and position of the bubbles. The "spider" patterns, on the other hand, are caused by dimples on opposite sides of the droplet surface. Since the density fluctuations are presumably connected to the dopant positions, this observation indicates an underlying structure ordering the dopants. In spinning superfluid droplets, quantized vortices form that attract the dopants which will eventually get trapped [12, 112, 244]. Hence, the observed structure could hint at the presence of vortices in the droplet, implying that the light induced dynamics can help to reveal structures otherwise invisible, since the diameter of a typical vortex is much smaller ($\approx 0.2\,\mathrm{nm}$ [12]) than the wavelength of the XUV light pulse.

The findings of this work point at several pathways I consider worth following in the future that I would like to present as an outlook, although some of the studies are already (partly) underway.

Most importantly, the results corroborate that the wide-angle scattering technique provides additional and valuable information on the morphology of individual nanoparticles. For example, while the shape outline (i.e., the two-dimensional projection) of a wheel-shaped and a pill-shaped droplet can be identical, their 3D shapes are very different leading to disparate physical interpretations. In a combined small-angle and wide-angle scattering approach, the inner structure and the 3D shape of a particle could be resolved simultaneously. In order to record small-angle and wide-angle scattering data of the same particle at the same time, x-ray FEL facilities could be equipped with high harmonic generation (HHG) sources delivering intense XUV light pulses. Furthermore, this approach could improve assigning the particles' orientation and provide additional information on asymmetric density distributions, thus enhancing iterative phase retrieval algorithms in coherent diffraction imaging (CDI) experiments. In this context, it is also remarkable that scattering signal from doped helium nanodroplets was observed up to long delay times (several hundreds of picoseconds), indicating that the droplets could

indeed serve as a sacrificial layer minimizing radiation damage in CDI experiments investigating single embedded particles [23–25].

In order to gain a deeper understanding of the randomly distributed density fluctuations in the helium nanodroplets, it would be interesting to be able to differentiate between fluctuations inside the droplets and fluctuations on the surface. This could be achieved by recording scattering images at different wavelengths: A resonant wavelength would be quickly absorbed by the droplet and therefore be only sensitive to the droplet surface, while a non-resonant wavelength would give information about the whole droplet volume. Using the recently developed two-color capabilities at FEL sources [234] together with a wavelength-sensitive photon detection scheme [200], such an experiment has become feasible.

Finally, the huge variety of characteristic features observed in diffraction patterns of the dynamic data set could be addressed in different ways: (i) Thoroughly analyzing the power density dependence of the light induced dynamics might provide an additional criterion for the classification of the images and further insight into the ignition threshold and subsequent dynamics (e.g., the complexity of the features observed in the images could be dependent on the energy deposited in the droplet). Because of the limited beam time at FEL facilities, lab-based HHG sources could enable studies that systematically explore an even larger parameter space. (ii) A neural network approach could enable the classification of extremely large and diverse data sets. When trained with simulated diffraction patterns of sufficiently variable model shapes, it might even lay the foundations for an automated 3D shape retrieval algorithm. (iii) Because of the multitude of shapes helium nanodroplets exhibit, they could serve as an ideal model system to develop an "FEL microscope": Recording real space images of disintegrating droplets using diamond Fresnel zone plates that can withstand the full power FEL beam for focusing [246] may be a promising approach to eliminate the need for reconstruction algorithms and ultimately resolve the ambiguity introduced by the loss of phase during the imaging process.

Appendices

Appendix A

Size Dependent Scattering Cross Section

The scattering cross section C_{sca} is calculated for droplet radii ranging from 1 nm to 500 nm using a MATLAB computer code [206, 207] that is based on the book *Absorption and Scattering of Light by Small Particles* by C. F. Bohren and D. R. Huffman [152]. The calculation is performed using an adapted MATLAB script originally written by A. Ulmer. The optical parameters δ and β, as shown in Fig. A.1, are taken from Ref. [205]. The resulting scattering cross section for different droplet size regimes is shown in Fig. A.2.

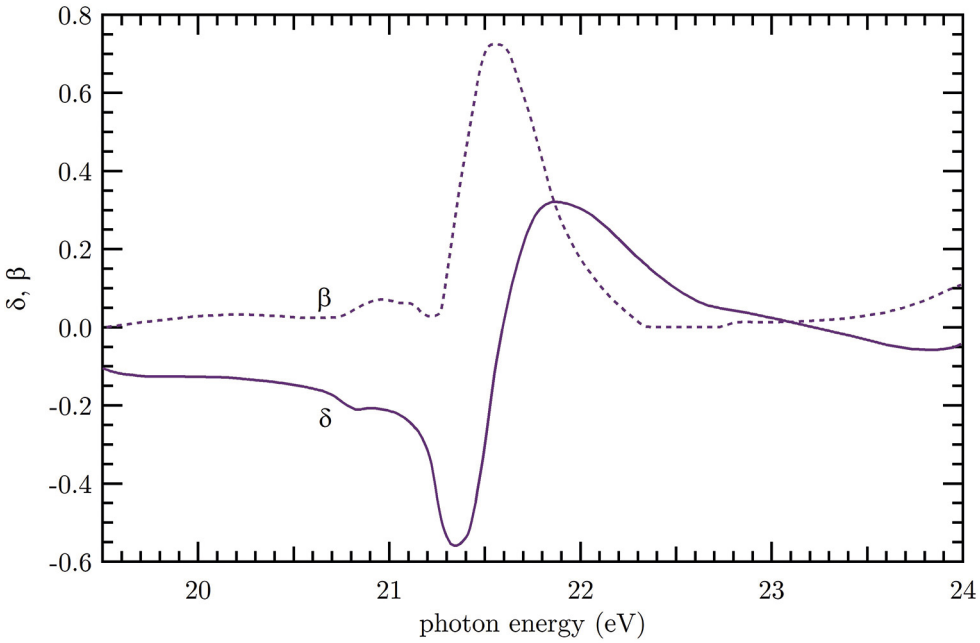

FIG. A.1: Refractive index $\underline{n} = 1 - \delta + i\beta$ of bulk liquid helium. Data are reproduced from Ref. [205].

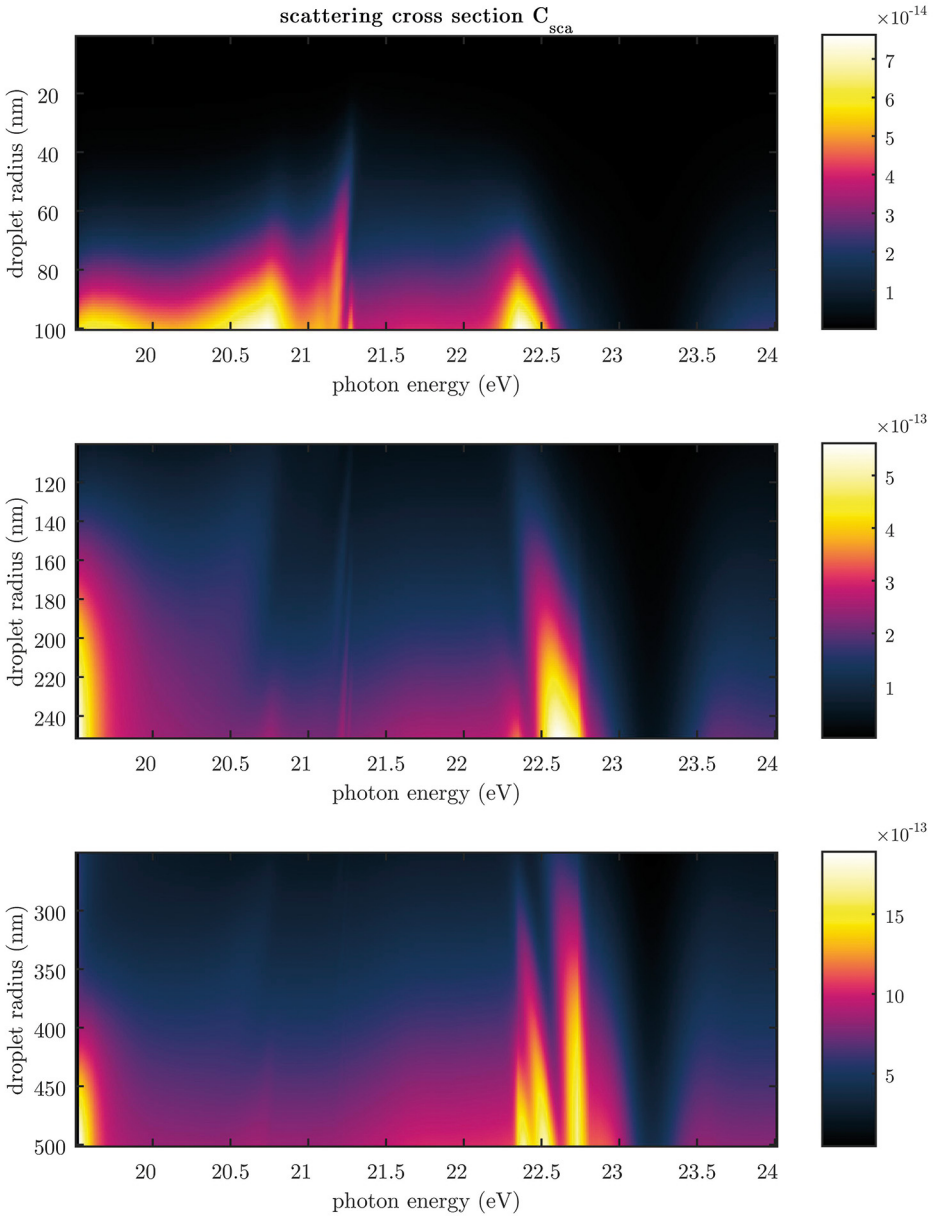

FIG. A.2: Size dependent scattering cross section C_{sca}, calculated for droplet radii ranging from 1 nm to 500 nm using a Mie scattering code [206].

Appendix B

Shape Determination Results

In Tab. B.1, the results from the helium nanodroplet shape determination are summarized (reproduced from the Supplemental Material to Ref. [17]). The recorded scattering image, forward-fitted MSFT simulation, and corresponding model shape are shown. In addition, the experimental parameters (FEL shot number, wavelength λ_{FEL}) and the retrieved shape parameters (principal axes a, b, c, and volume V) are given.

TABLE B.1: Comparison of experimental data and MSFT simulations.

Scattering image	MSFT simulation	Model shape
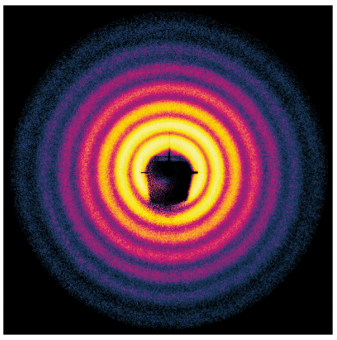	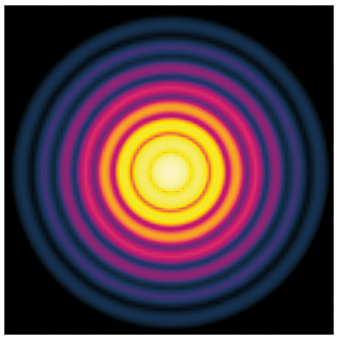	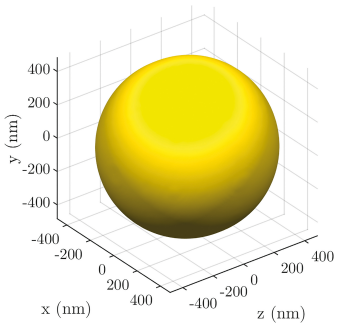
Shot No.: 265895973, $\lambda_{\mathrm{FEL}} = 57.6$ nm, $a/c = 1.03$, $b^3/V = 0.23$ $a = 483.0$ nm, $b = 475.8$ nm, $c = 468.6$ nm, $V = 4.59 \times 10^8$ nm^3		
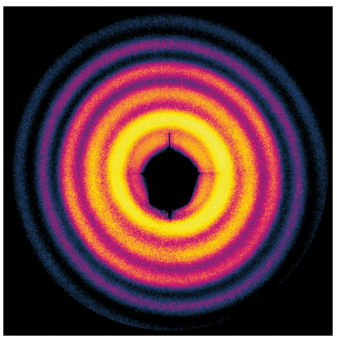	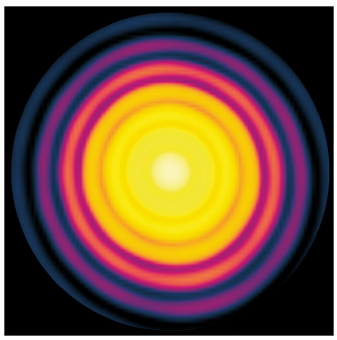	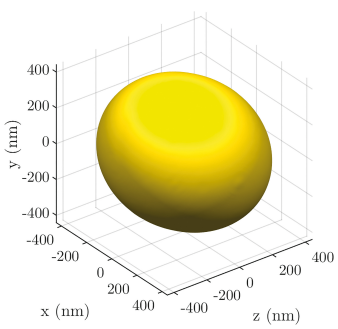
Shot No.: 266136010, $\lambda_{\mathrm{FEL}} = 60.4$ nm, $a/c = 1.17$, $b^3/V = 0.25$ $a = 438.9$ nm, $b = 421.3$ nm, $c = 375.0$ nm, $V = 2.98 \times 10^8$ nm^3		

TABLE B.1: *(Continued).*

Scattering image	MSFT simulation	Model shape
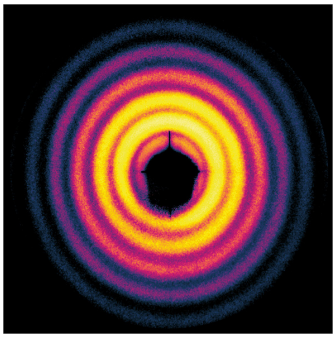	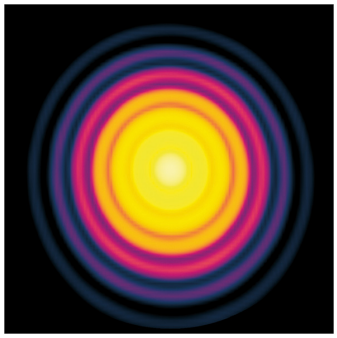	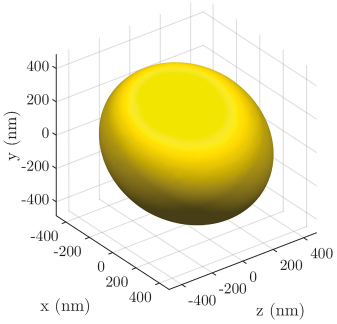
Shot No.: 266136203, $\lambda_{\mathrm{FEL}} = 60.4$ nm, $a/c = 1.18$, $b^3/V = 0.26$ $a = 480.8$ nm, $b = 466.3$ nm, $c = 408.4$ nm, $V = 3.83 \times 10^8$ nm^3		
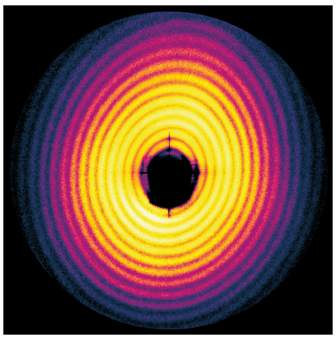	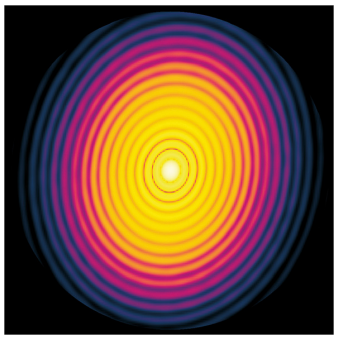	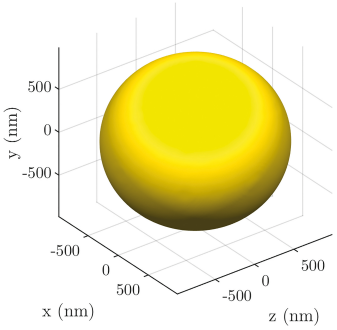
Shot No.: 266064137, $\lambda_{\mathrm{FEL}} = 59.0$ nm, $a/c = 1.19$, $b^3/V = 0.27$ $a = 978.2$ nm, $b = 963.4$ nm, $c = 820.9$ nm, $V = 3.26 \times 10^9$ nm^3		
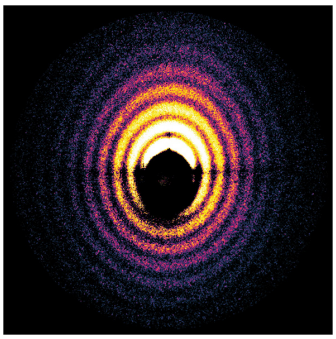	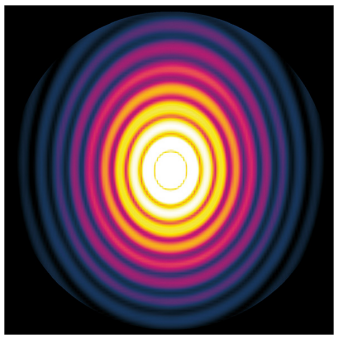	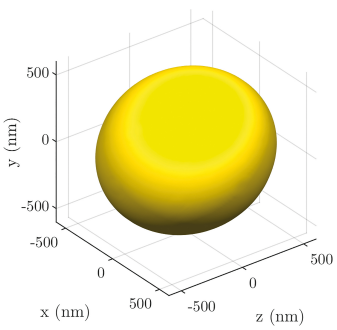
Shot No.: 265908753, $\lambda_{\mathrm{FEL}} = 57.6$ nm, $a/c = 1.26$, $b^3/V = 0.29$ $a = 600.8$ nm, $b = 594.8$ nm, $c = 477.6$ nm, $V = 7.27 \times 10^8$ nm^3		

TABLE B.1: *(Continued).*

Scattering image	MSFT simulation	Model shape
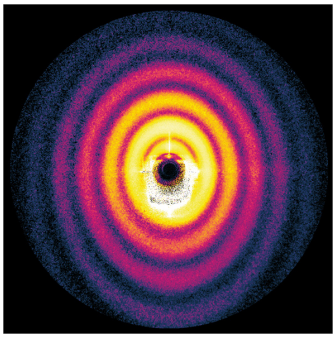	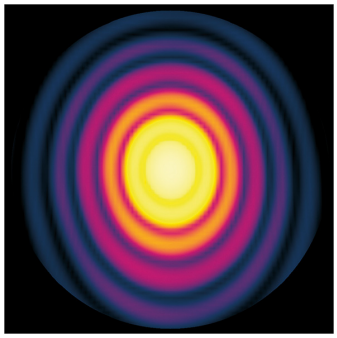	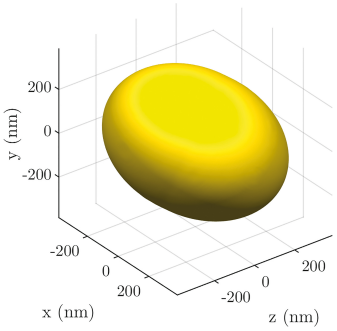
Shot No.: 266072644, $\lambda_{\mathrm{FEL}} = 59.0$ nm, $a/c = 1.33$, $b^3/V = 0.30$ $a = 385.4$ nm, $b = 381.5$ nm, $c = 289.0$ nm, $V = 1.83 \times 10^8$ nm^3		
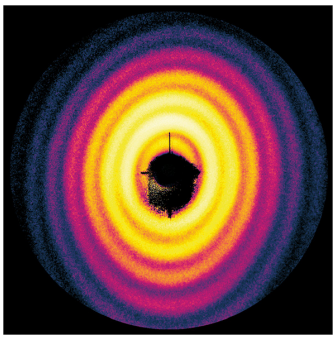	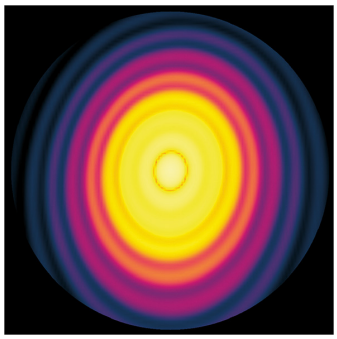	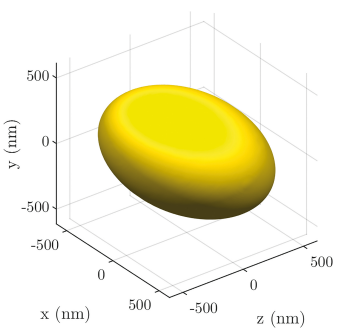
Shot No.: 266256017, $\lambda_{\mathrm{FEL}} = 65.0$ nm, $a/c = 1.49$, $b^3/V = 0.26$ $a = 612.6$ nm, $b = 529.9$ nm, $c = 410.4$ nm, $V = 5.63 \times 10^8$ nm^3		
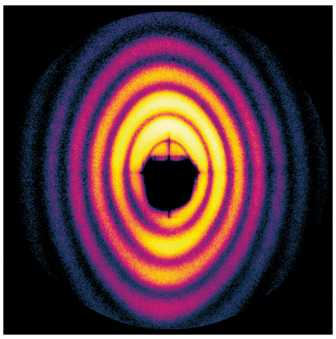	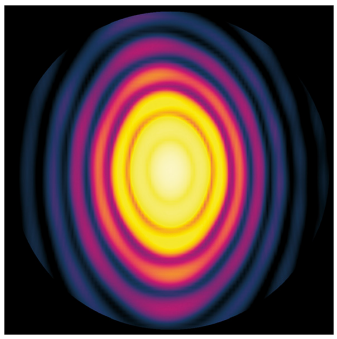	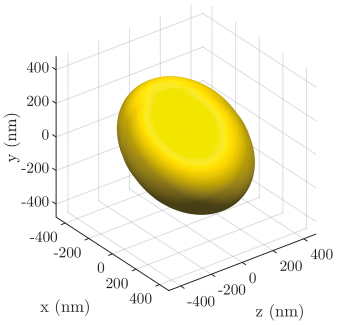
Shot No.: 266064963, $\lambda_{\mathrm{FEL}} = 59.0$ nm, $a/c = 1.59$, $b^3/V = 0.20$ $a = 477.5$ nm, $b = 360.5$ nm, $c = 300.8$ nm, $V = 2.30 \times 10^8$ nm^3		

TABLE B.1: *(Continued).*

Scattering image	MSFT simulation	Model shape
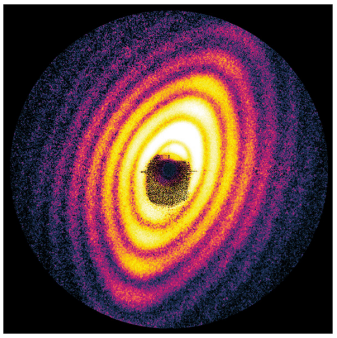	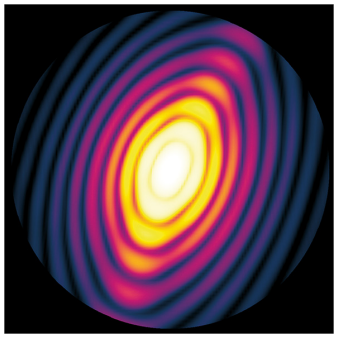	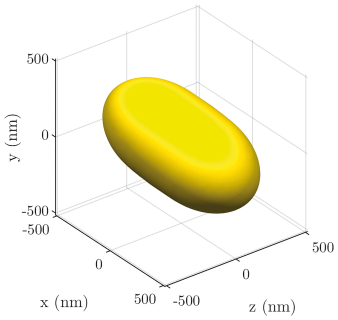

Shot No.: 266003758, $\lambda_{\mathrm{FEL}} = 52.3$ nm, $a/c = 1.82$, $b^3/V = 0.16$
$a = 512.7$ nm, $b = 325.6$ nm, $c = 282.0$ nm, $V = 2.19 \times 10^8$ nm^3

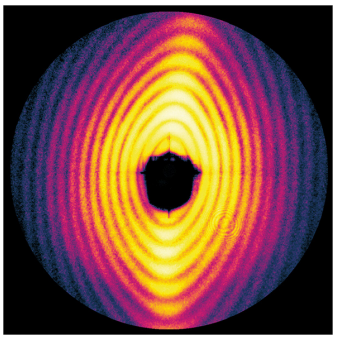	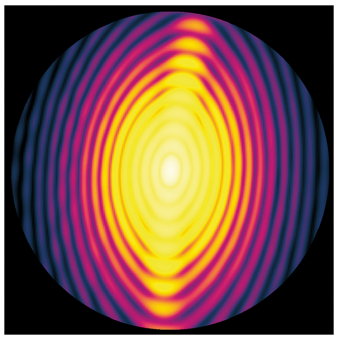	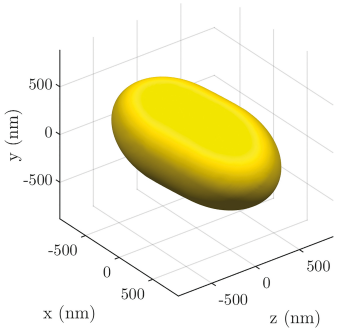

Shot No.: 266063056, $\lambda_{\mathrm{FEL}} = 59.0$ nm, $a/c = 1.83$, $b^3/V = 0.16$
$a = 881.7$ nm, $b = 559.9$ nm, $c = 480.5$ nm, $V = 1.11 \times 10^9$ nm^3

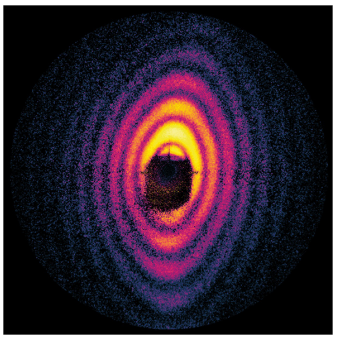	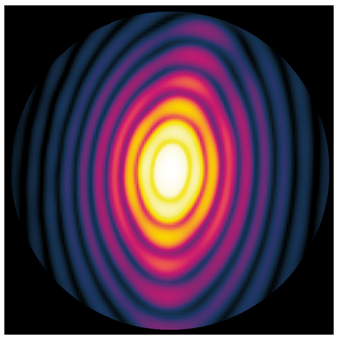	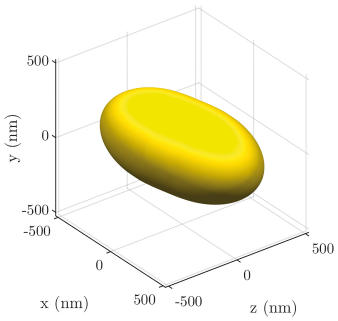

Shot No.: 265992109, $\lambda_{\mathrm{FEL}} = 52.3$ nm, $a/c = 1.87$, $b^3/V = 0.16$
$a = 522.7$ nm, $b = 329.3$ nm, $c = 279.7$ nm, $V = 2.21 \times 10^8$ nm^3

TABLE B.1: *(Continued).*

Scattering image	MSFT simulation	Model shape
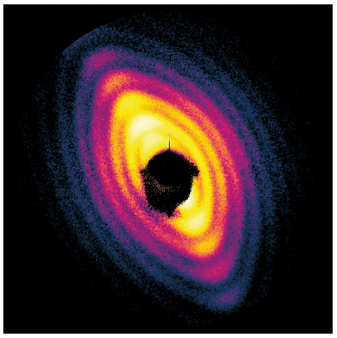	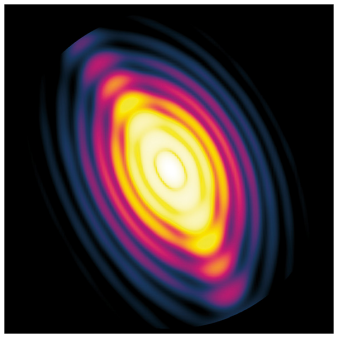	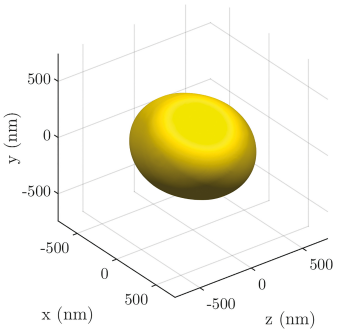
Shot No.: 265924525, $\lambda_{\mathrm{FEL}} = 63.8$ nm, $a/c = 1.87$, $b^3/V = 0.15$ $a = 742.0$ nm, $b = 456.3$ nm, $c = 397.0$ nm, $V = 6.30 \times 10^8$ nm^3		
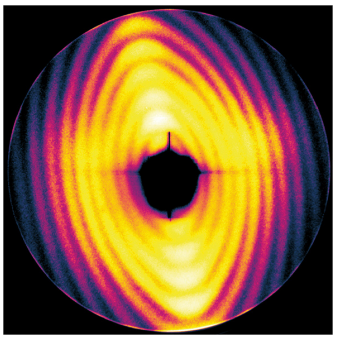	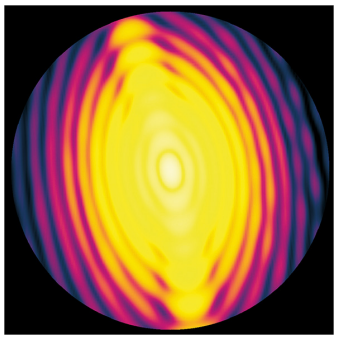	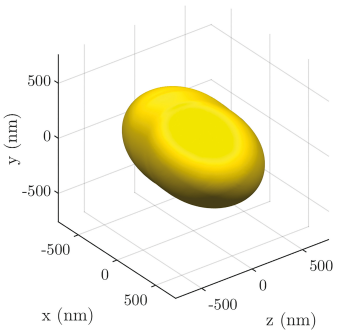
Shot No.: 265937735, $\lambda_{\mathrm{FEL}} = 63.8$ nm, $a/c = 1.90$, $b^3/V = 0.16$ $a = 758.3$ nm, $b = 489.1$ nm, $c = 398.1$ nm, $V = 7.21 \times 10^8$ nm^3		
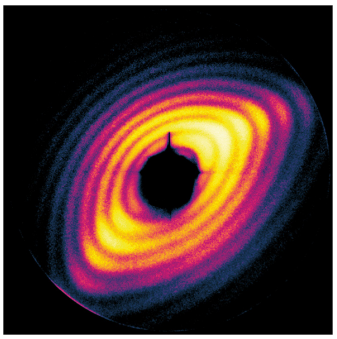	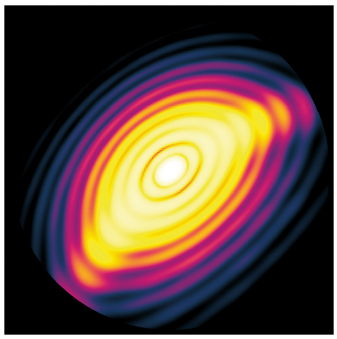	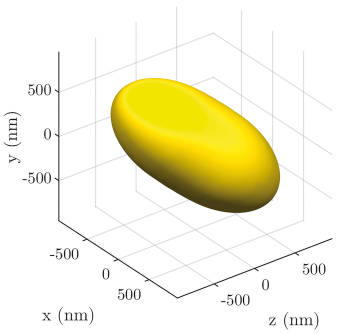
Shot No.: 265936645, $\lambda_{\mathrm{FEL}} = 63.8$ nm, $a/c = 1.98$, $b^3/V = 0.14$ $a = 954.5$ nm, $b = 539.3$ nm, $c = 482.0$ nm, $V = 1.13 \times 10^9$ nm^3		

TABLE B.1: *(Continued).*

Scattering image	MSFT simulation	Model shape
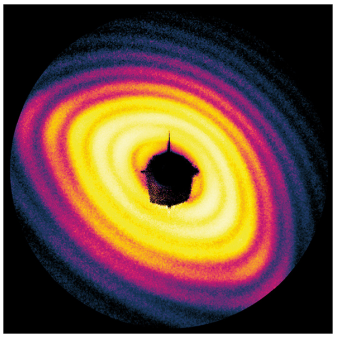	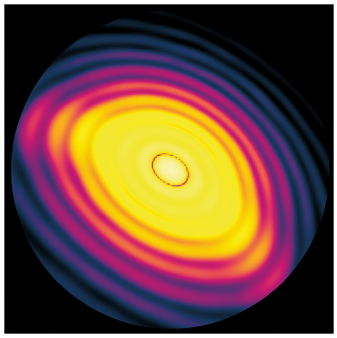	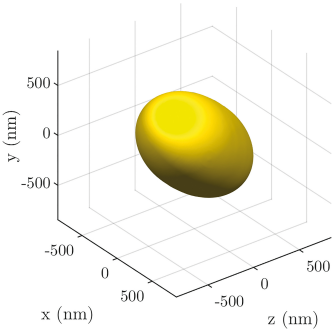
Shot No.: 265938988, $\lambda_{\mathrm{FEL}} = 63.8$ nm, $a/c = 2.06$, $b^3/V = 0.14$ $a = 844.5$ nm, $b = 468.7$ nm, $c = 409.6$ nm, $V = 7.28 \times 10^8$ nm^3		
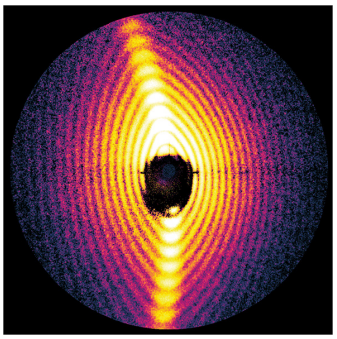	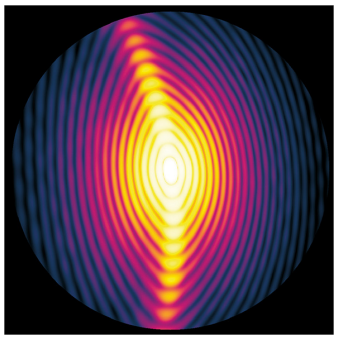	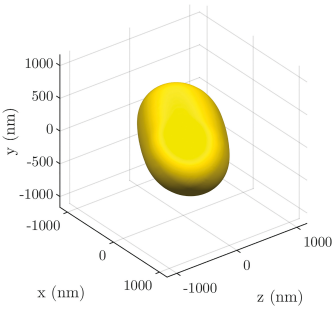
Shot No.: 266017694, $\lambda_{\mathrm{FEL}} = 52.3$ nm, $a/c = 2.13$, $b^3/V = 0.12$ $a = 1163.6$ nm, $b = 599.2$ nm, $c = 546.9$ nm, $V = 1.85 \times 10^9$ nm^3		
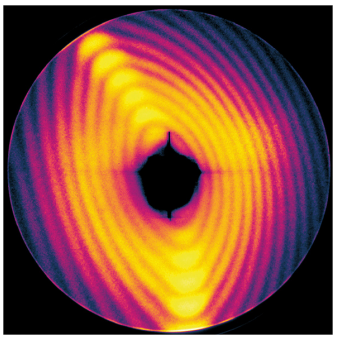	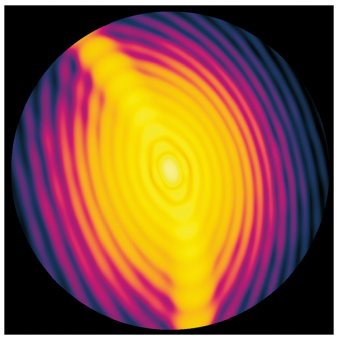	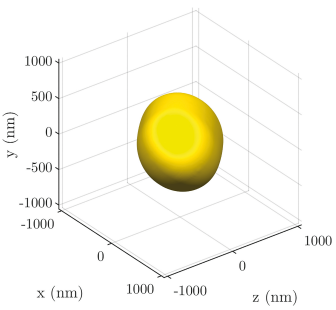
Shot No.: 265927658, $\lambda_{\mathrm{FEL}} = 63.8$ nm, $a/c = 2.20$, $b^3/V = 0.12$ $a = 1054.8$ nm, $b = 543.2$ nm, $c = 479.9$ nm, $V = 1.35 \times 10^9$ nm^3		

TABLE B.1: *(Continued).*

Scattering image	MSFT simulation	Model shape
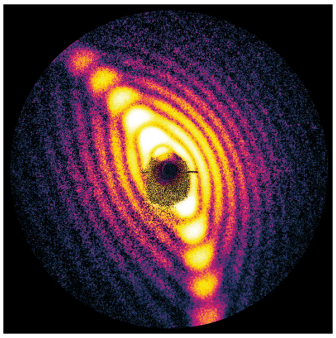	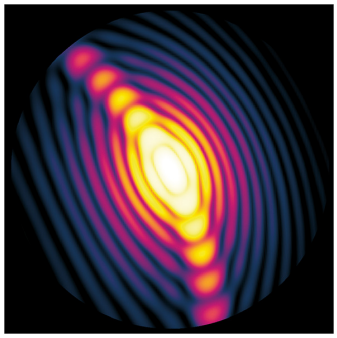	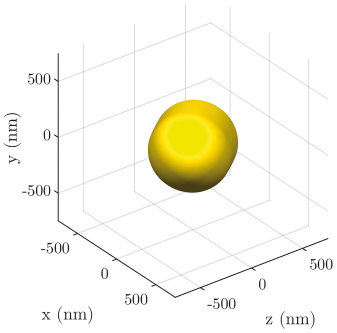
Shot No.: 265996304, $\lambda_{\mathrm{FEL}} = 52.3$ nm, $a/c = 2.44$, $b^3/V = 0.10$ $a = 747.3$ nm, $b = 332.5$ nm, $c = 306.4$ nm, $V = 3.85 \times 10^8$ nm^3		
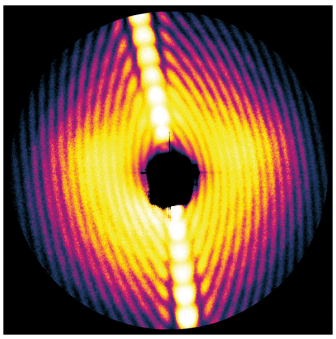	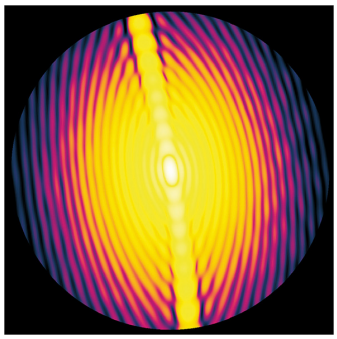	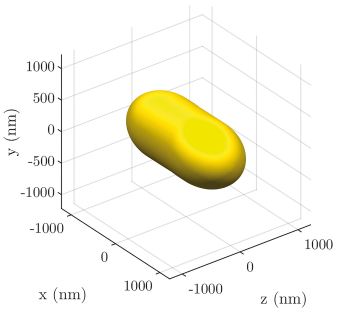
Shot No.: 266131187, $\lambda_{\mathrm{FEL}} = 60.4$ nm, $a/c = 2.56$, $b^3/V = 0.10$ $a = 1218.8$ nm, $b = 560.6$ nm, $c = 475.3$ nm, $V = 1.73 \times 10^9$ nm^3		
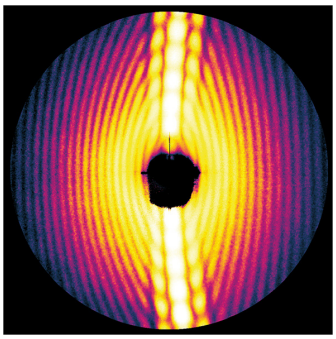	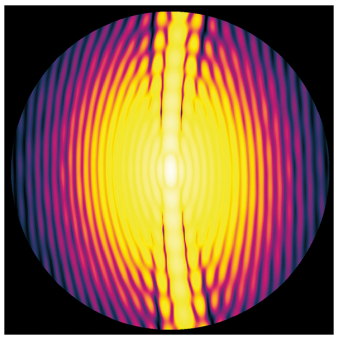	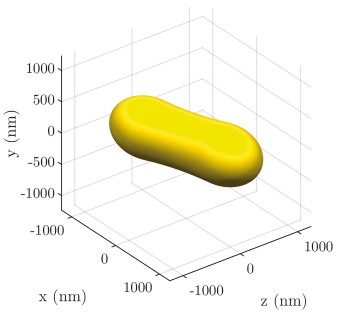
Shot No.: 266115394, $\lambda_{\mathrm{FEL}} = 60.4$ nm, $a/c = 3.03$, $b^3/V = 0.07$ $a = 1232.5$ nm, $b = 449.9$ nm, $c = 406.7$ nm, $V = 1.34 \times 10^9$ nm^3		

Bibliography

[1] W. C. Röntgen, "Ueber eine neue Art von Strahlen", Sonderabdruck aus den Sitzungsberichten der Würzburger Physik.-medic. Gesellschaft 1895 (1896).

[2] *The Nobel Prize in Physics 1914*, NobelPrize.org. Nobel Media AB, (2020) https://www.nobelprize.org/prizes/physics/1914/summary/ (visited on 11/21/2020).

[3] *The Nobel Prize in Physics 1915*, NobelPrize.org. Nobel Media AB, (2020) https://www.nobelprize.org/prizes/physics/1915/summary/ (visited on 11/21/2020).

[4] W. Hoppe, "Structure Analysis with X Rays", in *Biophysics*, edited by W. Hoppe, W. Lohmann, H. Markl, and H. Ziegler (Springer, 1983), pp. 50–65.

[5] A. McPherson and J. A. Gavira, "Introduction to protein crystallization", Acta Crystallographica Section F: Structural Biology Communications **70**, 2 (2014).

[6] C. Bostedt, D. M. Fritz, Z. Huang, H. J. Lee, H. Lemke, W. F. Schlotter, J. J. Turner, and G. J. Williams, "Linac Coherent Light Source : The First Five Years", Reviews of Modern Physics **88**, 10.1103/RevModPhys.88.015007 (2015).

[7] J. Rossbach, J. R. Schneider, and W. Wurth, "10 years of pioneering X-ray science at the Free-Electron Laser FLASH at DESY", Physics Reports **808**, 1 (2019).

[8] I. Schlichting, "Serial femtosecond crystallography: The first five years", IUCrJ **2**, 246 (2015).

[9] M. J. Bogan, D. Starodub, C. Y. Hampton, and R. G. Sierra, "Single-particle coherent diffractive imaging with a soft x-ray free electron laser: towards soot aerosol morphology", Journal of Physics B: Atomic, Molecular and Optical Physics **43**, 194013 (2010).

[10] M. M. Seibert *et al.*, "Single mimivirus particles intercepted and imaged with an X-ray laser", Nature **470**, 78 (2011).

[11] D. Rupp, M. Adolph, L. Flückiger, T. Gorkhover, J. P. Müller, M. Müller, M. Sauppe, D. Wolter, S. Schorb, R. Treusch, C. Bostedt, and T. Möller, "Generation and structure of extremely large clusters in pulsed jets", Journal of Chemical Physics **141**, 044306 (2014).

[12] L. F. Gomez *et al.*, "Shapes and vorticities of superfluid helium nanodroplets", Science **345**, 906 (2014).

[13] I. Barke, H. Hartmann, D. Rupp, L. Flückiger, M. Sauppe, M. Adolph, S. Schorb, C. Bostedt, R. Treusch, C. Peltz, S. Bartling, T. Fennel, K.-H. Meiwes-Broer, and T. Möller, "The 3D-architecture of individual free silver nanoparticles captured by X-ray scattering", Nature Communications **6**, 6187 (2015).

[14] T. Ekeberg *et al.*, "Three-Dimensional Reconstruction of the Giant Mimivirus Particle with an X-Ray Free-Electron Laser", Physical Review Letters **114**, 098102 (2015).

[15] C. Bernando, R. M. P. Tanyag, C. Jones, C. Bacellar, M. Bucher, K. R. Ferguson, D. Rupp, M. P. Ziemkiewicz, L. F. Gomez, A. S. Chatterley, T. Gorkhover, M. Müller, J. Bozek, S. Carron, J. Kwok, S. L. Butler, T. Möller, C. Bostedt, O. Gessner, and A. F. Vilesov, "Shapes of rotating superfluid helium nanodroplets", Physical Review B **95**, 064510 (2017).

[16] T. Gorkhover *et al.*, "Femtosecond X-ray Fourier holography imaging of free-flying nanoparticles", Nature Photonics **12**, 150 (2018).

[17] B. Langbehn, K. Sander, Y. Ovcharenko, C. Peltz, A. Clark, M. Coreno, R. Cucini, P. Finetti, M. Di Fraia, L. Giannessi, C. Grazioli, D. Iablonskyi, A. C. LaForge, T. Nishiyama, V. Oliver Álvarez de Lara, P. Piseri, O. Plekan, K. Ueda, J. Zimmermann, K. C. Prince, F. Stienkemeier, C. Callegari, T. Fennel, D. Rupp, and T. Möller, "Three-Dimensional Shapes of Spinning Helium Nanodroplets", Physical Review Letters **121**, 255301 (2018).

[18] R. Neutze, R. Wouts, D. van der Spoel, E. Weckert, and J. Hajdu, "Potential for biomolecular imaging with femtosecond X-ray pulses", Nature **406**, 752 (2000).

[19] Z. Sun, J. Fan, H. Li, and H. Jiang, "Current status of single particle imaging with X-ray lasers", Applied Sciences **8**, 132 (2018).

[20] B. Ziaja, H. N. Chapman, R. Fäustlin, S. Hau-Riege, Z. Jurek, A. V. Martin, S. Toleikis, F. Wang, E. Weckert, and R. Santra, "Limitations of coherent diffractive imaging of single objects due to their damage by intense x-ray radiation", New Journal of Physics **14**, 115015 (2012).

[21] K. J. Gaffney and H. N. Chapman, "Imaging atomic structure and dynamics with ultrafast x-ray scattering.", Science **316**, 1444 (2007).

[22] D. Rupp, N. Monserud, B. Langbehn, M. Sauppe, J. Zimmermann, Y. Ovcharenko, T. Möller, F. Frassetto, L. Poletto, A. Trabattoni, F. Calegari, M. Nisoli, K. Sander, C. Peltz, M. J. Vrakking, T. Fennel, and A. Rouzée, "Coherent diffractive imaging of single helium nanodroplets with a high harmonic generation source", Nature Communications **8**, 493 (2017).

[23] S. P. Hau-Riege, R. A. London, H. N. Chapman, A. Szoke, and N. Timneanu, "Encapsulation and Diffraction-Pattern-Correction Methods to Reduce the Effect of Damage in X-ray Diffraction Imaging of Single Biological Molecules", Physical Review Letters **98**, 198302 (2007).

[24] A. Mikaberidze, U. Saalmann, and J. M. Rost, "Energy absorption of xenon clusters in helium nanodroplets under strong laser pulses", Physical Review A **77**, 041201(R) (2008).

[25] H. N. Chapman, "X-ray imaging beyond the limits", Nature Materials **8**, 299 (2009).

[26] J. P. Toennies and A. F. Vilesov, "Superfluid Helium Droplets: A Uniquely Cold Nanomatrix for Molecules and Molecular Complexes", Angewandte Chemie International Edition **43**, 2622 (2004).

[27] P. Jena and A. W. Castleman, "Clusters: a bridge across the disciplines of physics and chemistry.", Proceedings of the National Academy of Sciences of the United States of America **103**, 10560 (2006).

[28] J. Gspann, "Electronic and Atomic Impacts on Large Clusters", in Physics of Electronic and Atomic Collisions, edited by S. Datz (1982), pp. 79–96.

[29] M. Hartmann, R. Miller, J. Toennies, and A. F. Vilesov, "Rotationally Resolved Spectroscopy of SF_6 in Liquid Helium Clusters: A Molecular Probe of Cluster Temperature", Physical Review Letters **75**, 1566 (1995).

[30] S. Grebenev, J. P. Toennies, and A. F. Vilesov, "Superfluidity Within a Small Helium-4 Cluster: The Microscopic Andronikashvili Experiment", Science **279**, 2083 (1998).

[31] H. Haberland, *Clusters of Atoms and Molecules* (Springer, Berlin, 1994).

[32] E. W. Becker, K. Bier, and W. Henkes, "Strahlen aus kondensierten Atomen und Molekeln im Hochvakuum", Zeitschrift für Physik **146**, 333 (1956).

[33] D. R. Miller, "Free Jet Sources", in *Atomic and Molecular Beam Methods*, Vol. 1, edited by G. Scoles, in collab. with D. Bassi, U. Buck, and D. Lainé (Oxford University Press, 1988) Chap. 2, pp. 14–53.

[34] I. Yamada, J. Matsuo, N. Toyoda, and A. Kirkpatrick, "Materials processing by gas cluster ion beams", Materials Science and Engineering R **34**, 231 (2001).

[35] H. Pauly, in *Atom, Molecule, and Cluster Beams I, Basic Theory, Production and Detection of Thermal Energy Beams* (Springer, Berlin, 2000) Chap. 3, p. 105.

[36] H. Ashkenas and F. S. Sherman, *Structure and Utilization of Supersonic Free Jets in Low Density Wind Tunnels*, tech. rep. (NASA, 1965).

[37] H. C. W. Beijerinck, R. J. F. Van Gerwen, E. R. T. Kerstel, J. F. M. Martens, E. J. W. Van Vliembergen, M. R. T. Smits, and G. H. Kaashoek, "Campargue-type supersonic beam sources: absolute intensities, skimmer transmission and scaling laws for mono-atomic gases He, Ne and Ar", Chemical Physics **96**, 153 (1985).

[38] L. D. Landau and E. M. Lifshitz, "Shock Waves, §83. Steady flow of a gas", in *Fluid Mechanics*, 2nd edition (Pergamon Press, Oxford, 1987) Chap. 9, p. 316.

[39] I. Pócsik, "Lognormal distribution as the natural statistics of cluster systems", Zeitschrift für Physik D Atoms, Molecules and Clusters **20**, 395 (1991).

[40] O. Hagena, "Nucleation and growth of clusters in expanding nozzle flows", Surface Science **106**, 101 (1981).

[41] O. Hagena, "Condensation in free jets: Comparison of rare gases and metals", Zeitschrift für Physik D Atoms, Molecules and Clusters **4**, 291 (1987).

[42] O. Hagena, "Cluster ion sources", Review of Scientific Instruments **63**, 2374 (1991).

[43] U. Buck and R. Krohne, "Cluster size determination from diffractive He atom scattering", The Journal of Chemical Physics **105**, 5408 (1996).

[44] F. Dorchies, F. Blasco, T. Caillaud, J. Stevefelt, C. Stenz, A. Boldarev, and V. Gasilov, "Spatial distribution of cluster size and density in supersonic jets as targets for intense laser pulses", Physical Review A **68**, 023201 (2003).

[45] H. Kamerlingh Onnes, "Experiments on the condensation of helium by expansion", in Royal Netherlands Academy of Arts and Sciences (KNAW), Vol. 10 (1908), pp. 744–747.

[46] E. W. Becker, R. Klingelhöfer, and P. Lohse, "Strahlen aus kondensiertem Helium im Hochvakuum", Zeitschrift für Naturforschung A **16**, 1259 (1961).

[47] R. D. McCarty and V. D. Arp, "A New Wide Range Equation of State for Helium", in *NIST Chemistry WebBook, NIST Standard Reference Database Number 69*, edited by P. J. Linstrom and W. G. Mallard (National Institute of Standards and Technology, Gaithersburg MD, 20899).

[48] E. L. Knuth, W. Li, and J. P. Toennies, "Phase-Diagram Considerations of Cluster Formation When Using Nozzle-Beam Sources", in *Rarefied gas dynamics: physical phenomena*, edited by E. P. Muntz, D. P. Weaver, and D. H. Campbell (American Institute of Aeronautics and Astronautics, Washington DC, 1989), pp. 329–334.

[49] H. Buchenau, E. L. Knuth, J. Northby, J. P. Toennies, and C. Winkler, "Mass spectra and time-of-flight distributions of helium cluster beams", The Journal of Chemical Physics **92**, 6875 (1990).

[50] B. L. Holian and D. E. Grady, "Fragmentation by Molecular Dynamics: The Microscopic "Big Bang"", Physical Review Letters **60**, 1355 (1988).

[51] R. E. Grisenti and J. P. Toennies, "Cryogenic microjet source for orthotropic beams of ultralarge superfluid helium droplets.", Physical Review Letters **90**, 234501 (2003).

[52] J. P. Toennies and K. Winkelmann, "Theoretical studies of highly expanded free jets: Influence of quantum effects and a realistic intermolecular potential", The Journal of Chemical Physics **66**, 3965 (1977).

[53] D. M. Brink and S. Stringari, "Density of states and evaporation rate of helium clusters", Zeitschrift für Physik D **15**, 257 (1990).

[54] E. L. Knuth and U. Henne, "Average size and size distribution of large droplets produced in a free-jet expansion of a liquid", The Journal of Chemical Physics **110**, 2664 (1999).

[55] F. Bierau, P. Kupser, G. Meijer, and G. von Helden, "Catching Proteins in Liquid Helium Droplets", Physical Review Letters **105**, 133402 (2010).

[56] D. Verma and A. F. Vilesov, "Pulsed helium droplet beams", Chemical Physics Letters **694**, 129 (2018).

[57] J. P. Toennies and A. F. Vilesov, "Spectroscopy of Atoms and Molecules in Liquid Helium", Annual Review of Physical Chemistry **49**, 1 (1998).

[58] F. Stienkemeier and K. K. Lehmann, "Spectroscopy and dynamics in helium nanodroplets", Journal of Physics B: Atomic, Molecular and Optical Physics **39**, R127 (2006).

[59] M. Lewerenz, B. Schilling, and J. P. Toennies, "Successive capture and coagulation of atoms and molecules to small clusters in large liquid helium clusters", The Journal of Chemical Physics **102**, 8191 (1995).

[60] A. Volk, P. Thaler, M. Koch, E. Fisslthaler, W. Grogger, and W. E. Ernst, "High resolution electron microscopy of Ag-clusters in crystalline and non-crystalline morphologies grown inside superfluid helium nanodroplets", Journal of Chemical Physics **138**, 214312 (2013).

[61] P. Thaler, A. Volk, F. Lackner, J. Steurer, D. Knez, W. Grogger, F. Hofer, and W. E. Ernst, "Formation of bimetallic core-shell nanowires along vortices in superfluid He nanodroplets", Physical Review B **90**, 155442 (2014).

[62] J. P. Toennies, A. F. Vilesov, and K. B. Whaley, "Superfluid Helium Droplets: An Ultracold Nanolaboratory", Physics Today **54**, 31 (2001).

[63] T. E. Gough, M. Mengel, P. A. Rowntree, and G. Scoles, "Infrared spectroscopy at the surface of clusters: SF_6 on Ar", The Journal of Chemical Physics **83**, 4958 (1985).

[64] L. F. Gomez, E. Loginov, R. Sliter, and A. F. Vilesov, "Sizes of large He droplets.", Journal of Chemical Physics **135**, 154201 (2011).

[65] W. F. Vinen, "The Physics of Superfluid Helium", CAS - CERN Accelerator School on Superconductivity and Cryogenics for Accelerators and Detectors, 363 (2002).

[66] C. Enss and S. Hunklinger, *Low-Temperature Physics* (Springer, Berlin, 2005).

[67] S. Balibar, "The Discovery of Superfluidity", Journal of Low Temperature Physics **146**, 441 (2007).

[68] D. van Delft, *Freezing physics, Heike Kamerlingh Onnes and the quest for cold* (Royal Netherlands Academy of Arts and Sciences (KNAW), Amsterdam, 2007).

[69] H. Kamerlingh Onnes, "The liquefaction of helium", in Royal Netherlands Academy of Arts and Sciences (KNAW), Vol. 11 (1909), pp. 168–185.

[70] H. Kamerlingh Onnes, "Further experiments with liquid helium", in Royal Netherlands Academy of Arts and Sciences (KNAW), Vol. 13 (1911), pp. 1093–1113.

[71] F. London, "On Condensed Helium at Absolute Zero", Proceedings of the Royal Society of London. Series A - Mathematical and Physical Sciences **153**, 576 (1936).

[72] W. H. Keesom and M. Wolfke, "Two different liquid states of helium", in Royal Netherlands Academy of Arts and Sciences (KNAW), 31 (1928), pp. 90–94.

[73] W. H. Keesom and K. Clusius, "Ueber die spezifische Wärme des flüssigen Heliums", in Royal Netherlands Academy of Arts and Sciences (KNAW), 35 (1932), pp. 307–320.

[74] W. H. Keesom and A. P. Keesom, "New measurements on the specific heat of liquid helium", in Royal Netherlands Academy of Arts and Sciences (KNAW), Vol. 35 (1932), pp. 736–742.

[75] J. C. McLennan, H. D. Smith, and J. O. Wilhelm, "XIV. The scattering of light by liquid helium", The London, Edinburgh, and Dublin Philosophical Magazine and Journal of Science **14**, 161 (1932).

[76] W. H. Keesom and A. P. Keesom, "On the Heat Conductivity of Liquid Helium", Physica **3**, 359 (1936).

[77] J. F. Allen, R. Peierls, and M. Zaki Uddin, "Heat Conduction in Liquid Helium", Nature **140**, 62 (1937).

[78] B. V. Rollin and F. Simon, "On the 'film' phenomenon of liquid helium II", Physica **6**, 219 (1939).

[79] J. F. Allen and H. Jones, "New Phenomena Connected with Heat Flow in Helium II", Nature **141**, 243 (1938).

[80] P. Kapitza, "Viscosity of Liquid Helium below the λ-Point", Nature **141**, 74 (1938).

[81] J. F. Allen and A. D. Misener, "Flow of Liquid Helium II", Nature **141**, 75 (1938).

[82] F. London, "The λ-Phenomenon of Liquid Helium and the Bose-Einstein Degeneracy", Nature **141**, 643 (1938).

[83] L. Tisza, "Transport Phenomena in Helium II", Nature **141**, 913 (1938).

[84] L. Landau, "Theory of the Superfluidity of Helium II", Physical Review **60**, 356 (1941).

[85] A. J. Leggett, "Superfluidity", Reviews of Modern Physics **71**, S318 (1999).

[86] D. R. Allum, P. V. E. McClintock, and A. Phillips, "The Breakdown of Superfluidity in Liquid ^{4}He: An Experimental Test of Landau's Theory", Philosophical Transactions of the Royal Society of London. Series A, Mathematical and Physical Sciences **284**, 179 (1977).

[87] R. J. Donnelly, "The Landau parameters in helium II", Physics Letters A **39**, 221 (1972).

[88] A. Schmitt, *Introduction to superfluidity, Field-theoretical approach and applications* (Springer, Cham, 2015).

[89] E. L. Andronikashvili, "Temperature dependence of the normal density of He II", Journal of Experimental and Theoretical Physics **18**, 424 (1948).

[90] P. Sindzingre, M. L. Klein, and D. M. Ceperley, "Path-integral Monte Carlo Study of Low-Temperature ^{4}He Clusters", Physical Review Letters **63**, 1601 (1989).

[91] O. J. Griffiths, P. Hendry, P. V. E. McClintock, and H. A. Nichol, "Liquid ^{4}He and its Superfluidity", in *Patterns of Symmetry Breaking*, Vol. 127, edited by H. Arodz, J. Dziarmaga, and W. H. Zurek, NATO Science Series (Series II: Mathematics, Physics and Chemistry) (Springer, Dordrecht, 2003).

[92] R. J. Donnelly, *Quantized Vortices in Helium II*, edited by A. M. Goldman, P. V. E. McClintock, and M. Springford, Cambridge Studies in Low Temperature Physics (Cambridge University Press, Cambridge, 1991).

[93] R. P. Feynman, "Application of Quantum Mechanics to Liquid Helium", in *Progress in low temperature physics*, Vol. 1, edited by C. J. Gorter (North-Holland, Amsterdam, 1955) Chap. 2, pp. 17–53.

[94] D. V. Osborne, "The Rotation of Liquid Helium II", Proceedings of the Physical Society. Section A **63**, 909 (1950).

[95] W. F. Vinen, "Detection of single quanta of circulation in rotating helium II", Proceedings of the Royal Society A **260**, 218 (1961).

[96] C. F. Jones *et al.*, "Coupled motion of Xe clusters and quantum vortices in He nanodroplets", Physical Review B **93**, 180510 (2016).

[97] S. M. O. O'Connell, R. M. P. Tanyag, D. Verma, C. Bernando, W. Pang, C. Bacellar, C. A. Saladrigas, J. Mahl, B. W. Toulson, Y. Kumagai, P. Walter, F. Ancilotto, M. Barranco, M. Pi, C. Bostedt, O. Gessner, and A. F. Vilesov, "Angular momentum in rotating superfluid droplets", Physical Review Letters **124**, 215301 (2020).

[98] E. J. Yarmchuk, M. J. V. Gordon, and R. E. Packard, "Observation of stationary vortex arrays in rotating superfluid helium", Physical Review Letters **43**, 214 (1979).

[99] I. Newton, "Book III, Propositions XVIII-XX", in *The Mathematical Principles of Natural Philosophy*, trans. by A. Motte (London, 1729).

[100] J. Plateau, "Mémoire sur les phénomènes que présente une masse liquide libre et soustraite à l'action de la pesanteur", Nouveaux mémoires de l'Académie Royale des Sciences et Belles-Lettres de Bruxelles **16**, 1 (1843).

[101] V. Cardoso, "The many shapes of spinning drops", Physics **1**, 38 (2008).

[102] S. Chandrasekhar, "The stability of a rotating liquid drop", Proceedings of the Royal Society A **286**, 1 (1965).

[103] R. A. Brown and L. E. Scriven, "The Shape and Stability of Rotating Liquid Drops", Proceedings of the Royal Society A **371**, 331 (1980).

[104] T. G. Wang, E. H. Trinh, A. P. Croonquist, and D. D. Elleman, "Shapes of rotating free drops: Spacelab experimental results", Physical Review Letters **56**, 452 (1986).

[105] T. G. Wang, A. V. Anilkumar, C. P. Lee, and K. C. Lin, "Bifurcation of rotating liquid drops: results from USML-1 experiments in Space", Journal of Fluid Mechanics **276**, 389 (1994).

[106] R. J. A. Hill and L. Eaves, "Nonaxisymmetric Shapes of a Magnetically Levitated and Spinning Water Droplet", Physical Review Letters **101**, 234501 (2008).

[107] K. A. Baldwin, S. L. Butler, and R. J. A. Hill, "Artificial tektites: an experimental technique for capturing the shapes of spinning drops.", Scientific Reports **5**, 7660 (2015).

[108] S. Cohen, F. Plasil, and W. J. Swiatecki, "Equilibrium configurations of rotating charged or gravitating liquid masses with surface tension. II", Annals of Physics **82**, 557 (1974).

[109] G. M. Seidel and H. J. Maris, "Morphology of superfluid drops with angular momentum", Physica B: Physics of Condensed Matter **194-196**, 577 (1994).

[110] J. D. Close, F. Federmann, K. Hoffmann, and N. Quaas, "Helium Droplets: A Nanoscale Cryostat for High Resolution Spectroscopy and Studies of Quantized Vorticity", Journal of Low Temperature Physics **111**, 661 (1998).

[111] K. K. Lehmann and R. Schmied, "Energetics and possible formation and decay mechanisms of vortices in helium nanodroplets", Physical Review B **68**, 224520 (2003).

[112] L. F. Gomez, E. Loginov, and A. F. Vilesov, "Traces of Vortices in Superfluid Helium Droplets", Physical Review Letters **108**, 155302 (2012).

[113] F. Ancilotto, M. Pi, and M. Barranco, "Vortex arrays in nanoscopic superfluid helium droplets", Physical Review B **91**, 100503 (2015).

[114] U. Saalmann, C. Siedschlag, and J. Rost, "Mechanisms of cluster ionization in strong laser pulses", Journal of Physics B: Atomic, Molecular and Optical Physics **39**, R39 (2006).

[115] T. Fennel, K.-H. Meiwes-Broer, J. Tiggesbäumker, P.-G. Reinhard, P. M. Dinh, and E. Suraud, "Laser-driven nonlinear cluster dynamics", Reviews of Modern Physics **82**, 1793 (2010).

[116] C. Bostedt, M. Adolph, E. Eremina, M. Hoener, D. Rupp, S. Schorb, H. Thomas, A. R. B. de Castro, and T. Möller, "Clusters in intense FLASH pulses: ultrafast ionization dynamics and electron emission studied with spectroscopic and scattering techniques", Journal of Physics B: Atomic, Molecular and Optical Physics **43**, 194011 (2010).

[117] M. Arbeiter and T. Fennel, "Rare-gas clusters in intense VUV, XUV and soft x-ray pulses: signatures of the transition from nanoplasma-driven cluster expansion to Coulomb explosion in ion and electron spectra", New Journal of Physics **13**, 053022 (2011).

[118] T. Ditmire, T. Donnelly, A. M. Rubenchik, R. W. Falcone, and M. D. Perry, "Interaction of intense laser pulses with atomic clusters", Physical Review A **53**, 3379 (1996).

[119] C. Bostedt, T. Gorkhover, D. Rupp, and T. Möller, "Clusters and Nanocrystals", in *Synchrotron Light Sources and Free-Electron Lasers*, edited by E. J. Jaeschke, S. Khan, J. R. Schneider, and J. B. Hastings (Springer, 2019).

[120] C. Bostedt, E. Eremina, D. Rupp, M. Adolph, H. Thomas, M. Hoener, A. R. B. de Castro, J. Tiggesbäumker, K.-H. Meiwes-Broer, T. Laarmann, H. Wabnitz, E. Plönjes, R. Treusch, J. R. Schneider, and T. Möller, "Ultrafast X-Ray Scattering of Xenon Nanoparticles: Imaging Transient States of Matter", Physical Review Letters **108**, 093401 (2012).

[121] D. Rupp, L. Flückiger, M. Adolph, A. Colombo, T. Gorkhover, M. Harmand, M. Krikunova, J. P. Müller, T. Oelze, Y. Ovcharenko, M. Richter, M. Sauppe, S. Schorb, R. Treusch, D. Wolter, C. Bostedt, and T. Möller, "Imaging plasma formation in isolated nanoparticles with ultrafast resonant scattering", Structural Dynamics **7**, 034303 (2020).

[122] D. Rupp, L. Flückiger, M. Adolph, T. Gorkhover, M. Krikunova, J. P. Müller, M. Müller, T. Oelze, Y. Ovcharenko, B. Röben, M. Sauppe, S. Schorb, D. Wolter, R. Mitzner, M. Wöstmann, S. Roling, M. Harmand, R. Treusch, M. Arbeiter, T. Fennel, C. Bostedt, and T. Möller, "Recombination-Enhanced Surface Expansion of Clusters in Intense Soft X-Ray Laser Pulses", Physical Review Letters **117**, 153401 (2016).

[123] T. Gorkhover *et al.*, "Nanoplasma Dynamics of Single Large Xenon Clusters Irradiated with Superintense X-Ray Pulses from the Linac Coherent Light Source Free-Electron Laser", Physical Review Letters **108**, 245005 (2012).

[124] T. Gorkhover *et al.*, "Femtosecond and nanometre visualization of structural dynamics in superheated nanoparticles", Nature Photonics **10**, 93 (2016).

[125] L. Flückiger, D. Rupp, M. Adolph, T. Gorkhover, M. Krikunova, M. Müller, T. Oelze, Y. Ovcharenko, M. Sauppe, S. Schorb, C. Bostedt, S. Düsterer, M. Harmand, H. Redlin, R. Treusch, and T. Möller, "Time-resolved x-ray imaging of a laser-induced nanoplasma and its neutral residuals", New Journal of Physics **18**, 043017 (2016).

[126] M. D. Perry, O. L. Landen, A. Szöke, and E. M. Campbell, "Multiphoton ionization of the noble gases by an intense 10^{14}-W/cm^2 dye laser", Physical Review A **37**, 747 (1988).

[127] S. Augst, D. Strickland, D. D. Meyerhofer, S. L. Chin, and J. H. Eberly, "Tunneling Ionization of Noble Gases in a High-Intensity Laser Field", Physical Review Letters **63**, 2212 (1989).

[128] M. Richter, S. V. Bobashev, A. A. Sorokin, and K. Tiedtke, "Multiphoton ionization of atoms with soft x-ray pulses", Journal of Physics B: Atomic, Molecular and Optical Physics **43**, 194005 (2010).

[129] L. Young, E. P. Kanter, B. Krässig, Y. Li, A. M. March, S. T. Pratt, R. Santra, S. H. Southworth, N. Rohringer, L. F. DiMauro, G. Doumy, C. A. Roedig, N. Berrah, L. Fang, M. Hoener, P. H. Bucksbaum, J. P. Cryan, S. Ghimire, J. M. Glownia, D. A. Reis, J. D. Bozek, C. Bostedt, and M. Messerschmidt, "Femtosecond electronic response of atoms to ultra-intense X-rays", Nature **466**, 56 (2010).

[130] D. Rupp, "Ionization and Plasma Dynamics of Single Large Xenon Clusters in Superintense XUV Pulses", Doctoral Dissertation (Technische Universität Berlin, Germany, 2013), DOI: https://doi.org/10.14279/depositonce-3643.

[131] L. V. Keldysh, "Ionization in the field of a strong electromagnetic wave", Soviet Physics - JETP **20**, 1307 (1965).

[132] H. Wabnitz, L. Bittner, A. R. B. de Castro, R. Döhrmann, P. Gürtler, T. Laarmann, W. Laasch, J. Schulz, A. Swiderski, K. von Haeften, T. Möller, B. Faatz, A. Fateev, J. Feldhaus, C. Gerth, U. Hahn, E. Saldin, E. Schneidmiller, K. Sytchev, K. Tiedtke, R. Treusch, and M. Yurkov, "Multiple ionization of atom clusters by intense soft X-rays from a free-electron laser", Nature **420**, 482 (2002).

[133] H. Wabnitz, A. R. B. de Castro, P. Gürtler, T. Laarmann, W. Laasch, J. Schulz, and T. Möller, "Multiple ionization of rare gas atoms irradiated with intense VUV radiation", Physical Review Letters **94**, 023001 (2005).

[134] R. Santra and C. H. Greene, "Xenon Clusters in Intense VUV Laser Fields", Physical Review Letters **91**, 233401 (2003).

[135] B. Ziaja, H. Wabnitz, F. Wang, E. Weckert, and T. Möller, "Energetics, Ionization, and Expansion Dynamics of Atomic Clusters Irradiated with Short Intense Vacuum-Ultraviolet Pulses", Physical Review Letters **102**, 205002 (2009).

[136] I. Last and J. Jortner, "Quasiresonance ionization of large multicharged clusters in a strong laser field", Physical Review A - Atomic, Molecular, and Optical Physics **60**, 2215 (1999).

[137] M. Arbeiter, C. Peltz, and T. Fennel, "Electron-relocalization dynamics in xenon clusters in intense soft-x-ray fields", Physical Review A - Atomic, Molecular, and Optical Physics **89**, 043428 (2014).

[138] C. Deiss, N. Rohringer, J. Burgdörfer, E. Lamour, C. Prigent, J. P. Rozet, and D. Vernhet, "Laser-cluster interaction: X-ray production by short laser pulses", Physical Review Letters **96**, 013203 (2006).

[139] G. Mie, "Beiträge zur Optik trüber Medien, speziell kolloidaler Metallösungen", Annalen der Physik **330**, 377 (1908).

[140] B. Schütte, M. Arbeiter, A. Mermillod-Blondin, M. J. Vrakking, A. Rouzée, and T. Fennel, "Ionization Avalanching in Clusters Ignited by Extreme-Ultraviolet Driven Seed Electrons", Physical Review Letters **116**, 033001 (2016).

[141] A. Heidenreich, B. Grüner, M. Rometsch, S. R. Krishnan, F. Stienkemeier, and M. Mudrich, "Efficiency of dopant-induced ignition of helium nanoplasmas", New Journal of Physics **18**, 073046 (2016).

[142] A. Mikaberidze, U. Saalmann, and J. M. Rost, "Laser-driven nanoplasmas in doped helium droplets: Local ignition and anisotropic growth", Physical Review Letters **102**, 128102 (2009).

[143] T. Döppner, J. P. Müller, A. Przystawik, S. Göde, J. Tiggesbäumker, K.-H. Meiwes-Broer, C. Varin, L. Ramunno, T. Brabec, and T. Fennel, "Steplike Intensity Threshold Behavior of Extreme Ionization in Laser-Driven Xenon Clusters", Physical Review Letters **105**, 053401 (2010).

[144] C. Peltz and T. Fennel, "Resonant charging of Xe clusters in helium nanodroplets under intense laser fields", European Physical Journal D **63**, 281 (2011).

[145] S. R. Krishnan, C. Peltz, L. Fechner, V. Sharma, M. Kremer, B. Fischer, N. Camus, T. Pfeifer, J. Jha, M. Krishnamurthy, C.-D. Schröter, J. Ullrich, F. Stienkemeier, R. Moshammer, T. Fennel, and M. Mudrich, "Evolution of dopant-induced helium nanoplasmas", New Journal of Physics **14**, 075016 (2012).

[146] D. Rupp, M. Adolph, T. Gorkhover, S. Schorb, D. Wolter, R. Hartmann, N. Kimmel, C. Reich, T. Feigl, A. R. B. de Castro, R. Treusch, L. Strüder, T. Möller, and C. Bostedt, "Identification of twinned gas phase clusters by single-shot scattering with intense soft x-ray pulses", New Journal of Physics **14**, 055016 (2012).

[147] H. N. Chapman *et al.*, "Femtosecond diffractive imaging with a soft-X-ray free-electron laser", Nature Physics **2**, 839 (2006).

[148] A. Doerr, "Diffraction before destruction", Nature Methods **8**, 283 (2011).

[149] E. Hecht, *Optics*, 4th ed. (Addison Wesley, San Francisco, 2002).

[150] J. C. H. Spence, U. Weierstall, and M. Howells, "Coherence and sampling requirements for diffractive imaging", Ultramicroscopy **101**, 149 (2004).

[151] J. R. Fienup, "Phase retrieval algorithms: a comparison", Applied Optics **21**, 2758 (1982).

[152] C. F. Bohren and D. R. Huffman, *Absorption and Scattering of Light by Small Particles* (Wiley-Interscience, 1998).

[153] J. M. Cowley and A. F. Moodie, "The Scattering of Electrons by Atoms and Crystals. I. A New Theoretical Approach", Acta Crystallographica **10**, 609 (1957).

[154] P. G. Self, M. A. O'Keefe, P. R. Buseck, and A. E. C. Spargo, "Practical computation of amplitudes and phases in electron diffraction", Ultramicroscopy **11**, 35 (1983).

[155] D. Reinhard, B. Hall, D. Ugarte, and R. Monot, "Size-independent fcc-to-icosahedral structural transition in unsupported silver clusters: An electron diffraction study of clusters produced by inert-gas aggregation", Physical Review B **55**, 7868 (1997).

[156] J. M. J. Madey, "Stimulated Emission of Bremsstrahlung in a Periodic Magnetic Field", Journal of Applied Physics **42**, 1906 (1971).

[157] L. R. Elias, W. M. Fairbank, J. M. J. Madey, H. A. Schwettman, and T. I. Smith, "Observation of Stimulated Emission of Radiation by Relativistic Electrons in a Spatially Periodic Transverse Magnetic Field", Physical Review Letters **36**, 717 (1976).

[158] D. A. Deacon, L. R. Elias, J. M. J. Madey, G. J. Ramian, H. A. Schwettman, and T. I. Smith, "First operation of a free-electron laser", Physical Review Letters **38**, 892 (1977).

[159] V. Ayvazyan *et al.*, "First operation of a free-electron laser generating GW power radiation at 32 nm wavelength", European Physical Journal D **37**, 297 (2006).

[160] P. Emma *et al.*, "First lasing and operation of an ångstrom-wavelength free-electron laser", Nature Photonics **4**, 641 (2010).

[161] E. Allaria *et al.*, "Highly coherent and stable pulses from the FERMI seeded free-electron laser in the extreme ultraviolet", Nature Photonics **6**, 699 (2012).

[162] P. Schmüser, M. Dohlus, J. Rossbach, and C. Behrens, *Free-Electron Lasers in the Ultraviolet and X-Ray Regime, Physical Principles, Experimental Results, Technical Realization*, 2nd ed. (Springer International Publishing Switzerland, 2014).

[163] E. J. Jaeschke, S. Khan, J. R. Schneider, and J. B. Hastings, eds., *Synchrotron Light Sources and Free-Electron Lasers, Accelerator Physics, Instrumentation and Science Applications*, 2 vols. (Springer International Publishing Switzerland, 2016).

[164] F. R. Elder, A. M. Gurewitsch, R. V. Langmuir, and H. C. Pollock, "Radiation from Electrons in a Synchrotron", Physical Review **71**, 829 (1947).

[165] V. Ayvazyan *et al.*, "A new powerful source for coherent VUV radiation: Demonstration of exponential growth and saturation at the TTF free-electron laser", European Physical Journal D **20**, 149 (2002).

[166] G. K. Shenoy, J. W. Lewellen, D. Shu, and N. A. Vinokurov, "Variable-period undulators as synchrotron radiation sources", Journal of Synchrotron Radiation **10**, 205 (2003).

[167] I. V. Davidyuk, O. A. Shevchenko, V. G. Tcheskidov, and N. A. Vinokurov, "Results of test of prototype of variable period undulator", Nuclear Instruments and Methods in Physics Research, A **871**, 77 (2017).

[168] L. H. Yu, "Generation of intense uv radiation by subharmonically seeded single-pass free-electron lasers", Physical Review A **44**, 5178 (1991).

[169] L.-H. Yu, M. Babzien, I. Ben-Zvi, L. F. DiMauro, A. Doyuran, W. Graves, E. Johnson, S. Krinsky, R. Malone, I. Pogorelsky, J. Skaritka, G. Rakowsky, L. Solomon, X. J. Wang, M. Woodle, V. Yakimenko, S. G. Biedron, J. N. Galayda, E. Gluskin, J. Jagger, V. Sajaev, and I. Vasserman, "High-Gain Harmonic-Generation Free-Electron Laser", Science **289**, 932 (2000).

[170] L. H. Yu, L. DiMauro, A. Doyuran, W. S. Graves, E. D. Johnson, R. Heese, S. Krinsky, H. Loos, J. B. Murphy, G. Rakowsky, J. Rose, T. Shaftan, B. Sheehy, J. Skaritka, X. J. Wang, and Z. Wu, "First Ultraviolet High-Gain Harmonic-Generation Free-Electron Laser", Physical Review Letters **91**, 074801 (2003).

[171] T. Hara, "Free-electron lasers: Fully coherent soft X-rays at FERMI", Nature Photonics **7**, 852 (2013).

[172] I. Ben-Zvi, K. M. Yang, and L. H. Yu, "The 'fresh-bunch' technique in FELS", Nuclear Instruments and Methods in Physics Research A **318**, 726 (1992).

[173] G. Stupakov, "Using the Beam-Echo Effect for Generation of Short-Wavelength Radiation", Physical Review Letters **102**, 074801 (2009).

[174] S. Khan, "Ultrashort Pulses from Synchrotron Radiation Sources", in *Synchrotron Light Sources and Free-Electron Lasers*, edited by E. J. Jaeschke, S. Khan, J. R. Schneider, and J. B. Hastings (Springer, 2016).

[175] E. Allaria *et al.*, "Two-stage seeded soft-X-ray free-electron laser", Nature Photonics **7**, 913 (2013).

[176] L. Giannessi and C. Masciovecchio, "FERMI: Present and Future Challenges", Applied Sciences **7**, 640 (2017).

[177] E. Allaria *et al.*, "The FERMI free-electron lasers", Journal of Synchrotron Radiation **22**, 485 (2015).

[178] S. Sasaki, "Analyses for a planar variably-polarizing undulator", Nuclear Instruments and Methods in Physics Research A **347**, 83 (1994).

[179] S. Lidia and R. Carr, "An elliptically-polarizing undulator with phase adjustable energy and polarization", Nuclear Instruments and Methods in Physics Research A **347**, 77 (1994).

[180] E. Allaria *et al.*, "Control of the Polarization of a Vacuum-Ultraviolet, High-Gain, Free-Electron Laser", Physical Review X **4**, 041040 (2014).

[181] P. Sigalotti, P. Cinquegrana, A. Demidovich, R. Ivanov, I. Nikolov, G. Kurdi, and M. B. Danailov, "Ultrafast laser synchronization at the FERMI@Elettra FEL", Advances in X-ray Free-Electron Lasers II: Instrumentation **8778**, 87780Q (2013).

[182] M. B. Danailov, F. Bencivenga, F. Capotondi, F. Casolari, P. Cinquegrana, A. Demidovich, E. Giangrisostomi, M. P. Kiskinova, G. Kurdi, M. Manfredda, C. Masciovecchio, R. Mincigrucci, I. P. Nikolov, E. Pedersoli, E. Principi, and P. Sigalotti, "Towards jitter-free pump-probe measurements at seeded free electron laser facilities", Optics Express **22**, 12869 (2014).

[183] P. Finetti *et al.*, "Pulse duration of seeded free-electron lasers", Physical Review X **7**, 021043 (2017).

[184] V. Lyamayev *et al.*, "A modular end-station for atomic, molecular, and cluster science at the low density matter beamline of FERMI@Elettra", Journal of Physics B: Atomic, Molecular and Optical Physics **46**, 164007 (2013).

[185] D. Pentlehner, R. Riechers, B. Dick, A. Slenczka, U. Even, N. Lavie, R. Brown, and K. Luria, "Rapidly pulsed helium droplet source", Review of Scientific Instruments **80**, 043302 (2009).

[186] A. T. J. B. Eppink and D. H. Parker, "Velocity map imaging of ions and electrons using electrostatic lenses: Application in photoelectron and photofragment ion imaging of molecular oxygen", Review of Scientific Instruments **68**, 3477 (1997).

[187] C. Svetina, D. Cocco, A. Di Cicco, C. Fava, S. Gerusina, R. Gobessi, N. Mahne, C. Masciovecchio, E. Principi, L. Raimondi, L. Rumiz, R. Sergo, G. Sostero, D. Spiga, and M. Zangrando, "An active optics system for EUV / soft x-ray beam shaping", in Proceedings of SPIE, Adaptive X-Ray Optics II, Vol. 8503, edited by A. M. Khounsary, S. L. O'Dell, and T. G. Bifano (2012), p. 850302.

[188] C. Svetina *et al.*, "The Low Density Matter (LDM) beamline at FERMI: Optical layout and first commissioning", Journal of Synchrotron Radiation **22**, 538 (2015).

[189] P. Mercère, P. Zeitoun, M. Idir, S. Le Pape, D. Douillet, X. Levecq, G. Dovillaire, S. Bucourt, K. A. Goldberg, P. P. Naulleau, and S. Rekawa, "Hartmann wavefront measurement at 13.4 nm with $\lambda_{\mathrm{EUV}}/120$ accuracy", Optics Letters **28**, 1534 (2003).

[190] M. Zangrando, A. Abrami, D. Bacescu, I. Cudin, C. Fava, F. Frassetto, A. Galimberti, R. Godnig, D. Giuressi, L. Poletto, L. Rumiz, R. Sergo, C. Svetina, and D. Cocco, "The photon analysis, delivery, and reduction system at the FERMI@Elettra free electron laser user facility", Review of Scientific Instruments **80**, 113110 (2009).

[191] PADReS group, *FEL-1 intensity monitor calibration procedure*, Elettra Sincrotrone Trieste, (2017) http://www.elettra.eu/lightsources/fermi/padres/procedures.html (visited on 09/24/2019).

[192] L. Giannessi, personal communication, Feb. 26, 2018.

[193] C. Callegari, personal communication, Mar. 2, 2020.

[194] LDM group, *LDM Beamline Description, Seed Laser for Users (SLU)*, Elettra Sincrotrone Trieste, (2015) https://www.elettra.trieste.it/lightsources/fermi/fermi-beamlines/ldm/beamline-description/page-3.html (visited on 11/12/2019).

[195] C. Callegari, personal communication, Nov. 7, 2019.

[196] A. Kramida, Y. Ralchenko, and NIST ASD Team, *NIST Atomic Spectra Database*, version 5.7.1, National Institute of Standards and Technology, Gaithersburg, MD., (2019) https://physics.nist.gov/asd (visited on 11/11/2019).

[197] M. Meyer, D. Cubaynes, P. O'Keeffe, H. Luna, P. Yeates, E. T. Kennedy, J. T. Costello, P. Orr, R. Taïeb, A. Maquet, S. Düsterer, P. Radcliffe, H. Redlin, A. Azima, E. Plönjes, and J. Feldhaus, "Two-color photoionization in xuv free-electron and visible laser fields", Physical Review A - Atomic, Molecular, and Optical Physics **74**, 011401 (2006).

[198] Oxford Instruments, *Andor neo 5.5 sCMOS camera*, https://andor.oxinst.com/products/scmos-camera-series/neo-5-5-scmos (visited on 09/30/2019).

[199] H. Fukuzawa, T. Tachibana, K. Motomura, W. Q. Xu, K. Nagaya, S. Wada, P. Johnsson, M. Siano, S. Mondal, Y. Ito, M. Kimura, T. Sakai, K. Matsunami, H. Hayashita, J. Kajikawa, X.-J. Liu, E. Robert, C. Miron, R. Feifel, J. P. Marangos, K. Tono, Y. Inubushi, M. Yabashi, M. Yao, and K. Ueda, "Electron spectroscopy of rare-gas clusters irradiated by x-ray free-electron laser pulses from SACLA", Journal of Physics B: Atomic, Molecular and Optical Physics **49**, 034004 (2016).

[200] L. Hecht, "Zweifarben-Streubildaufnahme von Helium-Nanotröpfchen, Planung, Durchführung und erste Ergebnisse", Master's thesis (Technische Universität Berlin, Germany, 2018).

[201] B. Langbehn, "Aufbau und Charakterisierung einer Quelle für Heliumcluster zur Strukturanalyse mit Lichtstreuung", Master's thesis (Technische Universität Berlin, Germany, 2015).

[202] W. Christen, "Stationary flow conditions in pulsed supersonic beams", Journal of Chemical Physics **139**, 10.1063/1.4824155 (2013).

[203] P. Nuñez von Voigt, "Charakterisierung der Zeitstruktur einer gepulsten Quelle für Helium-Nanotröpfchen durch Streuexperimente", Bachelor's thesis (Technische Universität Berlin, Germany, 2016).

[204] M. Joppien, R. Karnbach, and T. Möller, "Electronic Excitations in Liquid Helium: The Evolution from Small Clusters to Large Droplets", Physical Review Letters **71**, 2654 (1993).

[205] A. A. Lucas, J. P. Vigneron, S. E. Donnelly, and J. C. Rife, "Theoretical Interpretation of the Vacuum Ultraviolet Reflectance of Liquid-Helium and of the Absorption-Spectra of Helium Microbubbles in Aluminum", Physical Review B **28**, 2485 (1983).

[206] J. P. Schäfer, *MatScat code*, version 1.4, (2016) https://mathworks.com/matlabcentral/fileexchange/36831-matscat (visited on 10/15/2019).

[207] J. P. Schäfer, "Implementierung und Anwendung analytischer und numerischer Verfahren zur Lösung der Maxwellgleichungen für die Untersuchung der Lichtausbreitung in biologischem Gewebe", Doctoral dissertation (Universität Ulm, Germany, 2011), DOI: https://doi.org/10.18725/OPARU-1914.

[208] D. Attwood and A. Sakdinawat, *X-Rays and Extreme Ultraviolet Radiation, Principles and Applications*, 1st ed. (Cambridge University Press, Cambridge, 2016).

[209] M. Lewerenz, B. Schilling, and J. P. Toennies, "A new scattering deflection method for determining and selecting the sizes of large liquid clusters of ^{4}He", Chemical Physics Letters **206**, 381 (1993).

[210] U. Henne and J. P. Toennies, "Electron capture by large helium droplets", The Journal of Chemical Physics **108**, 9327 (1998).

[211] R. D. McCarty, "Thermodynamic Properties of Helium 4 from 2 to 1500 K at Pressures to 10^8 Pa", Journal of Physical and Chemical Reference Data **2**, 923 (1973).

[212] A. Nelde, "Automatisierte Größenbestimmung aus Röntgenstreubildern einzelner Edelgascluster", Bachelor's thesis (Technische Universität Berlin, Germany, 2016).

[213] B. L. Henke, E. M. Gullikson, and J. C. Davis, "X-Ray Interactions: Photoabsorption, Scattering, Transmission, and Reflection at E = 50-30,000 eV, Z = 1-92", Atomic Data and Nuclear Data Tables **54**, 181 (1993).

[214] R. G. Livesey, "Flow of Gases Through Tubes and Orifices", in *Foundations of Vacuum Science and Technology*, edited by J. M. Lafferty (John Wiley & Sons, Inc, New York, 1998) Chap. 2.

[215] O. Plekan, personal communication, Jan. 8, 2020.

[216] I. Y. Fugol', "Excitons in rare-gas crystals", Advances in Physics **27**, 1 (1978).

[217] O. Bünermann and F. Stienkemeier, "Modeling the formation of alkali clusters attached to helium nanodroplets and the abundance of high-spin states", European Physical Journal D **61**, 645 (2011).

[218] L. Liao and R. J. A. Hill, "Shapes and Fissility of Highly Charged and Rapidly Rotating Levitated Liquid Drops", Physical Review Letters **119**, 114501 (2017).

[219] J. Zimmermann, B. Langbehn, R. Cucini, M. Di Fraia, P. Finetti, A. C. LaForge, T. Nishiyama, Y. Ovcharenko, P. Piseri, O. Plekan, K. C. Prince, F. Stienkemeier, K. Ueda, C. Callegari, T. Möller, and D. Rupp, "Deep neural networks for classifying complex features in diffraction images", Physical Review E **99**, 063309 (2019).

[220] F. R. N. C. Maia, "The Coherent X-ray Imaging Data Bank", Nature Methods **9**, 854 (2012), CXIDB ID 94: `http://cxidb.org/id-94.html`.

[221] K. Sander, "Reconstruction methods for single-shot diffractive imaging of free nanostructures with ultrashort x-ray and XUV laser pulses", Doctoral dissertation (Universität Rostock, Germany, 2018), DOI: `https://doi.org/10.18453/rosdok_id00002439`.

[222] S. Marchesini, H. He, H. N. Chapman, S. P. Hau-Riege, A. Noy, M. R. Howells, U. Weierstall, and J. C. H. Spence, "X-ray image reconstruction from a diffraction pattern alone", Physical Review B **68**, 140101(R) (2003).

[223] R. M. P. Tanyag, C. Bernando, C. F. Jones, C. Bacellar, K. R. Ferguson, D. Anielski, R. Boll, S. Carron, J. P. Cryan, L. Englert, S. W. Epp, B. Erk, L. Foucar, L. F. Gomez, R. Hartmann, D. M. Neumark, D. Rolles, B. Rudek, A. Rudenko, K. R. Siefermann, J. Ullrich, F. Weise, C. Bostedt, O. Gessner, and A. F. Vilesov, "Communication: X-ray coherent diffractive imaging by immersion in nanodroplets", Structural Dynamics **2**, 051102 (2015).

[224] E. M. Purcell and C. R. Pennypacker, "Scattering and absorption of light by nonspherical dielectric grains", The Astrophysical Journal **186**, 705 (1973).

[225] B. T. Draine, "The discrete-dipole approximation and its application to interstellar graphite grains", The Astrophysical Journal **333**, 848 (1988).

[226] G. B. Dantzig, "Origins of the Simplex Method", in *A history of scientific computing*, edited by S. G. Nash (ACM, New York, 1990), pp. 141–151.

[227] J. C. Nash, "The (Dantzig) Simplex Method for Linear Programming", Computing in Science and Engineering **2**, 29 (2000).

[228] M. N. Slipchenko, S. Kuma, T. Momose, and A. F. Vilesov, "Intense pulsed helium droplet beams", Review of Scientific Instruments **73**, 3600 (2002).

[229] S. Yang, S. M. Brereton, and A. M. Ellis, "Controlled growth of helium nanodroplets from a pulsed source", Review of Scientific Instruments **76**, 104102 (2005).

[230] R. Katzy, M. Singer, S. Izadnia, A. C. LaForge, and F. Stienkemeier, "Doping He droplets by laser ablation with a pulsed supersonic jet source", Review of Scientific Instruments **87**, 013105 (2016).

[231] R. M. P. Tanyag, C. F. Jones, C. Bernando, S. M. O. O'Connell, D. Verma, and A. F. Vilesov, "Experiments with Large Superfluid Helium Nanodroplets", in *Cold Chemistry: Molecular Scattering and Reactivity Near Absolute Zero*, edited by O. Dulieu and A. Osterwalder (The Royal Society of Chemistry, 2018) Chap. 8, pp. 389–443.

[232] F. Ancilotto, M. Barranco, and M. Pi, "Spinning superfluid ^{4}He nanodroplets", Physical Review B **97**, 184515 (2018).

[233] F. Villars, "The Collective Model of Nuclei", Annual Review of Nuclear Science **7**, 185 (1957).

[234] E. Ferrari *et al.*, "Widely tunable two-colour seeded free-electron laser source for resonant-pump resonant-probe magnetic scattering", Nature Communications **7**, 10343 (2016).

[235] K. R. Ferguson, M. Bucher, T. Gorkhover, S. Boutet, H. Fukuzawa, J. E. Koglin, Y. Kumagai, A. Lutman, A. Marinelli, M. Messerschmidt, K. Nagaya, J. Turner, K. Ueda, G. J. Williams, P. H. Bucksbaum, and C. Bostedt, "Transient lattice contraction in the solid-to-plasma transition.", Science advances **2**, e1500837 (2016).

[236] T. Nishiyama *et al.*, "Ultrafast Structural Dynamics of Nanoparticles in Intense Laser Fields", Physical Review Letters **123**, 123201 (2019).

[237] S. Dold *et al.*, in preparation.

[238] C. Bacellar, A. S. Chatterley, F. Lackner, C. Pemmaraju, R. M. P. Tanyag, C. Bernando, D. Verma, S. O'Connell, M. Bucher, K. R. Ferguson, T. Gorkhover, N. C. Ryan, G. Coslovich, D. Ray, T. Osipov, D. M. Neumark, C. Bostedt, A. F. Vilesov, and O. Gessner, "Evaporation of an anisotropic nanoplasma", EPJ Web of Conferences **205**, 06006 (2019).

[239] S. R. Krishnan, L. Fechner, M. Kremer, V. Sharma, B. Fischer, N. Camus, J. Jha, M. Krishnamurthy, T. Pfeifer, R. Moshammer, J. Ullrich, F. Stienkemeier, M. Mudrich, A. Mikaberidze, U. Saalmann, and J.-M. Rost, "Dopant-Induced Ignition of Helium Nanodroplets in Intense Few-Cycle Laser Pulses", Physical Review Letters **107**, 173402 (2011).

[240] C. Peltz, personal communication, Jan. 21, 2020.

[241] J. Jordan, "Untersuchung von Licht induzierter Dynamik in Metallclustern mittels Röntgenbeugung", Master's thesis (Technische Universität Berlin, Germany, 2018).

[242] D. Bonhommeau, M. Lewerenz, and N. Halberstadt, "Fragmentation of ionized doped helium nanodroplets: Theoretical evidence for a dopant ejection mechanism", Journal of Chemical Physics **128**, 10.1063/1.2823101 (2008).

[243] M. Bucher, "Ultrafast dynamics of nanoparticles in highly intense x-ray pulses", Doctoral dissertation (Technische Universität Berlin, Germany, 2017), DOI: http://dx.doi.org/10.14279/depositonce-6598.

[244] F. Coppens, F. Ancilotto, M. Barranco, N. Halberstadt, and M. Pi, "Capture of Xe and Ar atoms by quantized vortices in 4 He nanodroplets", Physical Chemistry Chemical Physics **19**, 24805 (2017).

[245] R. P. Taylor, T. P. Martin, R. D. Montgomery, J. H. Smith, A. P. Micolich, C. Boydston, B. C. Scannell, M. S. Fairbanks, and B. Spehar, "Seeing shapes in seemingly random spatial patterns: Fractal analysis of Rorschach inkblots", PLoS ONE **12**, 1 (2017).

[246] C. David, S. Gorelick, S. Rutishauser, J. Krzywinski, J. Vila-Comamala, V. A. Guzenko, O. Bunk, E. Färm, M. Ritala, M. Cammarata, D. M. Fritz, R. Barrett, L. Samoylova, J. Grünert, and H. Sinn, "Nanofocusing of hard X-ray free electron laser pulses using diamond based Fresnel zone plates", Scientific Reports **1**, 57 (2011).